Size based separation of submicron nonmagnetic particles through magnetophoresis in structured obstacle arrays

by

V N Ravikanth Annavarapu

B.Tech., Chemical Engineering – Indian Institute of Technology, Madras 2005

M.Tech., Chemical Engineering – Indian Institute of Technology, Madras 2005

M.S., Chemical Engineering Practice - Massachusetts Institute of Technology, 2007

Submitted to the Department of Chemical Engineering in partial fulfillment of the requirements for the degree of

Doctor of Philosophy in Chemical Engineering Practice

at the

Massachusetts Institute of Technology

June 2010

Signature of Author.....
Department of Chemical Engineering
December, 2009

Certified by.....
T. Alan Hatton
Ralph Landau Professor of Chemical Engineering Practice
Thesis Supervisor

Certified by.....
Kenneth A. Smith
Gilliland Professor of Chemical Engineering
Thesis Supervisor

Accepted by.....
William M. Deen
Carbon P. Dubbs Professor of Engineering
Chairman, Committee for Graduate Students

Size based separation of submicron nonmagnetic particles through magnetophoresis in structured obstacle arrays

by

V N Ravikanth Annavarapu

Submitted to the Department of Chemical Engineering on December, 2009 in partial fulfillment of the requirements of the Degree of Doctor of Philosophy in Chemical Engineering Practice

ABSTRACT

The focus of this work was on developing a novel scalable size based separation technology for nonmagnetic particles in the submicron size range utilizing magnetophoretic forces. When a nonmagnetic particle is immersed in a magnetic fluid and subjected to magnetic field gradients, it behaves like a magnetic hole and experiences magnetic buoyancy forces proportional to its volume. This size dependence of magnetic buoyancy forces can be exploited to selectively focus larger nonmagnetic particles from a mixture and thus we can fractionate nonmagnetic particles on the basis of size.

We designed a separation system composed of a regular array of iron obstacle posts which utilized magnetic buoyancy forces to perform size based separations. A Lagrangian particle tracking model was developed which could describe the behavior of a nonmagnetic particle in regions of inhomogeneous magnetic field gradients. Particle trajectories were simulated for a number of obstacle array geometries and over a range of operating conditions in order to understand the nature of the magnetic buoyancy force and aid in separation system design.

Based on the results of the trajectory simulations, an experimental set up was conceptualized and built to demonstrate capture and separation of nonmagnetic particles using magnetic buoyancy forces. Capture visualization experiments were performed utilizing fluorescence microscopy which showed visual evidence of focusing and preferential capture of larger nonmagnetic particles. Experiments also yielded results qualitatively consistent with the Lagrangian trajectory model.

Pulse chromatography experiments were also performed in order to quantitatively understand the capture and separation behavior. The results obtained showed quantitative evidence of preferential capture of larger particles. Particle capture efficiencies were compared with predictions from simulations and were found to be qualitatively consistent. Finally, the potential of this separation technology was demonstrated by performing proof-of-concept separation experiments with a mixture of 840 nm and 240 nm particles.

Thesis Supervisor: T. Alan Hatton, Ralph Landau Professor of Chemical Engineering
Thesis Supervisor: Kenneth A. Smith, Gilliland Professor of Chemical Engineering

Acknowledgement

The completion of this thesis marks an important milestone in my life and I could not have achieved this without the support and dedication of a number of people. This acknowledgement is an attempt to express my profound gratitude towards everyone who made my journey over the past five years possible.

First of all, I would like to thank my advisors Prof. Alan Hatton and Prof. Ken Smith. Both of them have been a source of constant support and encouragement. Their hands-off advising style and their trust in my abilities has helped me become more independent and grow as a person. Whenever I was lost for ideas in my research, I would never be disappointed by Alan's creative inputs. Also, he acted as a calming influence during some difficult times. Prof. Smith is one of the sharpest people I have ever met. Discussing problems and results with him has been a pleasure and always made me draw new insights which I could not, on my own. I also had the pleasure of being a TA for him and thoroughly enjoyed our conversations on a multitude of topics. I would like to thank Prof. Deen and Prof. Doyle on my thesis committee for their guidance which allowed me to stay on track, while on a challenging timeline. Andrew Gallant and his colleagues at the MIT machine shop worked really hard to fabricate the experimental cell and my sincere gratitude to them as well. I would also like to thank Beth Tuths and Linda Mousseau for always being so helpful in everything.

Second, I would like to thank the entire Hatton group for providing me with an unforgettable experience. These are a group of extremely helpful individuals who are willing to drop whatever they are doing to assist someone else. Lino and Fei have been of profound help, initially as great teachers and later as valuable thought partners. Huan, Smeet, Vinay and Takuya also helped me at various times with experimental work. Finally, Abhinav, Himanshu, Vaibhav, Tatsushi and others were always there as good friends who made my PhD experience so pleasant.

Finally, I would like to thank all the people in my personal life – My roommates Mani, Srini and all other friends at MIT who have given me really happy memories of this place; Anusha, who has been a constant companion through every moment at MIT and beyond; My brother who is my best friend and a source of support through good times and bad; and finally, my parents whose unconditional love never ceases to amaze me and who I cannot thank through this simple acknowledgment. They gave up everything to ensure that I have a good future. This thesis is dedicated to them.

Table of Contents

List of Figures

List of Tables

Chapter 1

Introduction

1.1 Motivation

The world of fine particles is a fascinating one. Submicron and nanometer size particles have unique properties which make them ubiquitous in the chemical and materials industry. However, a great number of applications require precise control of the size, shape and morphology of these particles. This is a subtle task requiring involved synthetic procedures and careful control of experimental conditions during synthesis. If a reliable macro-scale technique of separation by size and shape is developed, industrial particle synthesis methods can be combined with this separation method and narrow particle size and shape distributions can be obtained easily. These ideas form the motivation behind this thesis. The overall goal of this work is to conceptualize techniques based on magnetophoresis for performing continuous size based separation of non-magnetic particles using a magnetic fluid.

1.1.1 Applications of sub-micron particles

The performance of products from a large number of industries relies on the quality of fine particles used for their manufacture. Fine particles can be of various types - inorganic, organic and biological particles. Inorganic fine particles consist of metals, metal oxides, non-metals and ceramics, whereas organic particles consist of polymers. Core shell particles which have an inorganic core and an organic polymeric shell are also attractive for a large number of applications [1]. Final products from many bioprocesses are also often in the form of crystals or inclusion bodies and are termed bio-particles [2]. The annual turnover of metal particle industry alone is in the excess of $ 17 billion in Europe and North America [3]. On including the other particle types, fine particle industry easily constitutes a multi-billion dollar industry.

Submicron particles have a special place in this industry because of their size. In the nanometer regime large surface to volume ratios result in properties quite different from the macro-scale. Below we describe some applications of various kinds of submicron particles as observed in recent literature.

1.1.1.1 Metal nanoparticles

Metal nanoparticles (NPs) possess interesting optical properties such as Surface Plasma Resonance. A large number of applications utilizing these interesting properties have been explored in literature. Gold NPs (~15 nm) have been used for the colorimetric detection of miniscule quantities of DNA [4-5] and proteins [6]. Slightly larger gold NPs (~100 nm) have been useful for photonics, photocatalysis and surface enhanced Raman spectroscopy (SERS) [7]. Using silver NPs (~120 nm) in the SERS technique, molecular spectroscopic signatures could be enhanced by enormous factors of 10^{14} to 10^{15} making it possible to detect even single molecules [8]. Platinum NPs (~250nm) have been useful as conductors in the electronics industry and also as catalysts for numerous industrial chemical syntheses [9]. Monodisperse submicron sized hollow silica capsules have been coated with gold nanoparticles on the inner surface to be utilized as biosensors as well [10].

1.1.1.2 Metal oxide nanoparticles

Metal oxides, like metals, find numerous applications in industry. A layer of TiO_2 NPs (size <500 nm) can block radiation in the range of 300 – 3000 nm due to their light scattering characteristics, a property useful in radiative cooling applications [11]. TiO_2 and other colloidal particles (e.g. polymers, carbon) are also useful for the formation of colloidal photonic crystals (CPC) [12-13] due to their ability to diffract light. CPCs consist of monodisperse spherical submicron NPs arranged in a close packed 2D or 3D crystal which can diffract visible and IR light and can be used to filter specific wavelengths of light [14]. CPCs made of hydrogels can perform colorimetric sensing of variations in pH, temperature, mechanical strain and the presence of solvents [15].

Silica NPs are also very common in the industry due to their ease of synthesis and low cost [16]. Monodisperse submicron SiO_2 can be used to formulate inks for inkjet printing of a range of applications such as OLEDs [17], flat panel displays [16] and drug delivery systems [18]. Silica (~500 nm) coated with a 60 nm layer of Yttrium Oxide ($Y_2O_3:Eu^{3+}$) can be used as phosphor for field emission displays and result in much brighter and higher definition displays[19]. Core-shell particles with an SiO_2 core and a metal shell have also been synthesized and are well known for their optical properties [20].

Hetero-structured nanoparticles combining metal and metal oxide (e.g. Au-Fe_2O_3) have been synthesized recently and are useful as imaging probes in magneto-optical applications[21].

1.1.1.3 Polymeric particles

The final class of NPs – polymer NPS can be custom synthesized for applications such as biomedical drug encapsulation inside a polymer matrix for specific drug delivery [1]. The submicron size of polymer particles also allows intracellular biosensing by fabricating non-invasive sensors consisting of encapsulated indicator dyes [22] and quantum dots [23].

1.1.2 Importance of separation of submicron particles

The many diverse applications of fine particles listed above have one commonality – the requirement of spherical particles lying within a narrow particle size distribution (PSD). This requirement stems from the fact that physical properties of colloids in the nanometer range are very strongly dependent on size [24]. Even the optical properties such as light scattering depend intrinsically on PSD and spacing of crystals [14-15, 19]. In the case of metals and metal oxides, a strong correlation has been observed between PSD and usefulness of the particles for the specific applications [8-9, 11, 24-25]. In addition, for CPCs and coatings, a uniform size of submicron spheres is needed to minimize crystal defects and get a highly structured packing. For biomedical applications such as drug

delivery and biosensing, specific size and shape are critical for effectively and non-invasively reaching intracellular targets [1, 23].

However, synthesis of submicron particles with a narrow PSD and shape distribution is a very challenging task. Mainly two methods of fine metal production exist – particle breakdown and chemical synthesis. In chemical synthesis methods, a wide PSD is obtained because phenomena of nuclei generation and coagulation which dominate particle growth are fluctuation driven in nature [26]. Even shape control is sometimes difficult during chemical synthesis and almost always for the breakdown method. For the specific case of Gold NPs, two distinct NP populations have been observed during chemical synthesis – nanorods and nanospheres [24]. The difficulty in obtaining monodispersity and spherical shape has been shown for other particle types as well where a strong dependence on experimental conditions is observed [9, 11-13, 20, 22-23, 27].

These problems in the synthesis of NPs could be solved by using separation processes for narrowing the output PSD. A separation device (such as the one proposed in this thesis) can take sub-micron particles having a wide PSD as an input and produce multiple streams with narrow output PSDs. Combining particle synthesis with separation could lead to nearly monodisperse particles. In addition, if the device also performs shape based sorting, particles with varying aspect ratios could be separated after synthesis, allowing much more flexibility in synthesis procedures and process conditions. Figure 1-1 shows size ranges of various colloidal particles. The expected operating range of the proposed separation technology is between from tens of nanometers to greater than a micron. Most of the inorganic NPs such as metals, metal oxides, and polymer particles lie within this range. In addition, several bio-particles are also fall in this range. Thus, a successful device for separating sub-micron particle can also separate viruses, bacteria, sub-cellular organelles and inclusion bodies hence, widening its applicability.

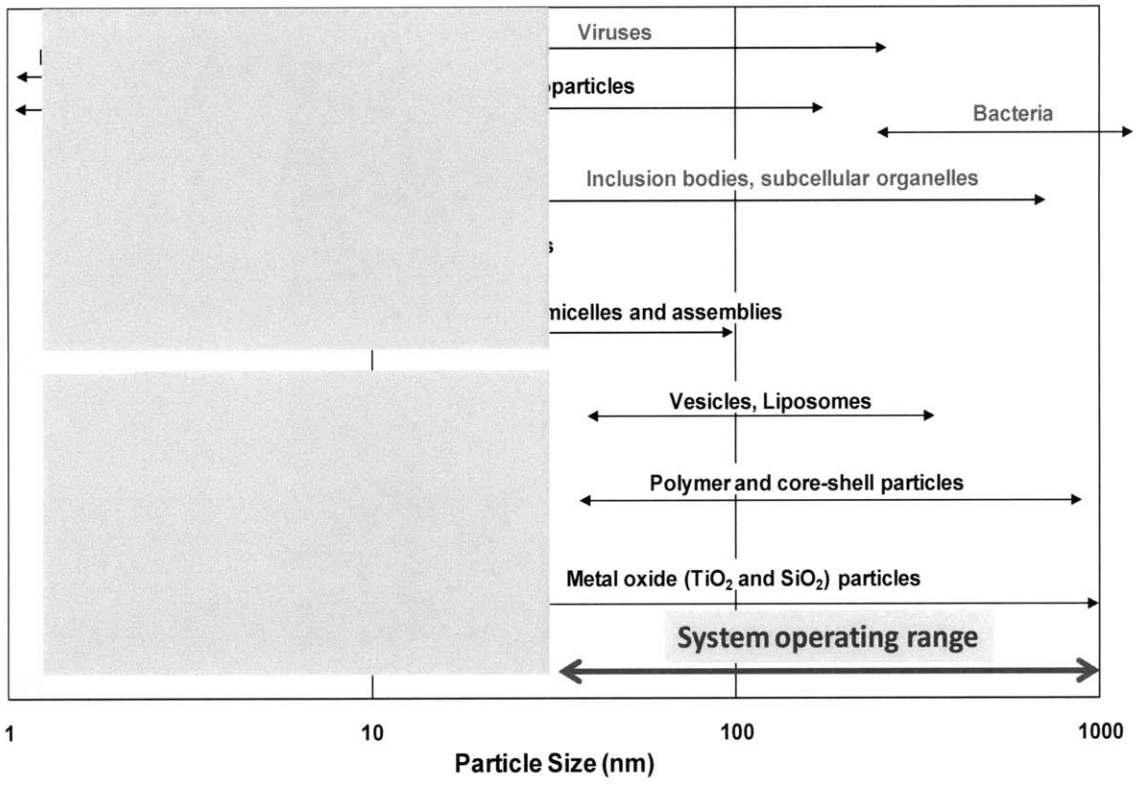

Figure 1-1: Size range of various colloidal particles and relation to operating range for a submicron separation system [28]

1.1.3 Literature review of existing particle separation systems

Much attention has been focused in recent years on developing novel technologies for separating fine particles in the submicron and micron size range. In addition, the rapid growth in micro- and nano-fluidic technologies as well as the emergence of Lab-on-a-Chip concept has contributed phenomenally to the area of sub-micron analysis and separation. A review of various separation methods is presented below organized in terms of driving forces for separation. The subject of magnetic separations, which is of direct relevance to this thesis, is presented as a separate sub-section. Finally, the need to develop a new macro scale technique for separating sub-micrometer particles using a magnetic fluid is emphasized in the final sub-section.

1.1.3.1 Separations in the absence of an external field

Separation in the absence of an external field is caused by the size dependent physical interactions between particles and the system. Examples of these separations include size exclusion chromatography and membrane based filtration processes which are well established methods. Much effort has been focused recently in developing deterministic or stochastic displacement devices which are implemented at the micro-scale.

Size exclusion chromatography (SEC) is one of the oldest methods of particle separation utilizing physical interactions. In this chromatographic method, the stationary phase consists of soft spherical particles that interact with particles in a phenomenon termed as molecular sieving [29]. Larger particles elute faster because they explore less of the interparticle void fraction. Kirkland showed rapid separations of ultrafine colloids in the range of 1-50 nm utilizing porous silica microspheres as the stationary phase [30]. Fischer et al fractionated very fine CdS-sols in the range 2-8 nm using SEC [31]. More recently, gold nanoparticles between 5.3 and 38.3 nm were separated with SEC using a polymer base column of 100 nm pore size [32]. However, SEC is known to be time intensive and suitable only for low volume analytical separations [26].

Membrane separation is another conventional separation method which can be used to separate particles in the size range 0.1 to 10 μm. In the above range, the process is known as microfiltration. Here, the separation membrane is designed in such a way that particles above a certain size are trapped above the membrane while other sizes pass through. Particles can be pushed through the membrane using different forces – pressure, vacuum, centrifugation etc. and the choice of the method is very specific to the system used [33]. However, membranes prepared by conventional methods are known to have a broad pore size distribution which limits their utility for size based separations [26].

On the micro scale, *hydrodynamic chromatography* (HC) has been shown to be an effective elution based method for characterizing submicron particles. Recently, HC was used to separate particles between 26nm and 155 nm [34]. When a mixture of particles is

sent through a channel with a parabolic flow profile, size exclusion of larger particles from the channel wall occurs exposing them to larger velocities. Hence, larger particles elute faster from the channel – the basic principle behind HC. Efforts have been directed to move from elution based to continuous HC. Zhang et al developed an innovative device design which led particles to follow different flow streamlines depending on their size, thus causing continuous separation [35]. However, only larger particle sizes between 10 and 25 μm could be separated with this device. Yamada et al also developed a continuous micro-scale separation device on the principle of HC which they named *pinched flow fractionation* (PFF) [36]. Particles were introduced continuously in a micro-channel containing a very narrow segment (pinch segment). The particles were aligned to the side wall in this segment resulting in them being excluded from the side wall. The size exclusion when combined with sudden expansion after the pinched stream, led to continuous separation in space. Separation was experimentally demonstrated for particles between 15 and 30 μm sizes. In later articles, improvements were proposed to separate smaller (order of 1 micron) and even non-spherical particles and to fractionate even multiple sizes simultaneously [37]. Researches from this group also developed the concept of hydrodynamic filtration (HF) which performs simultaneous separation and concentration of particles. This was demonstrated for particles between 2.1 and 3 μm where an 80 fold improvement in concentration was observed along with separation [38-39]. Blood separations to highly enrich the white blood cells (WBC) (factor of 4000) by have also been carried out in a similar fashion by utilizing the concept of perfusion flow in a micro-fluidic cell [40]. In a related separation concept called Differential Inertial Focusing, high throughput particle separations were carried out by channeling the lift and drag forces in asymmetrically curved channels for separation [41]. This work reported order of magnitude higher throughputs in the range milliliters per minute which is encouraging from an industrial perspective.

Displacement based devices for particle separations have also been explored recently. In these devices, a set of periodic obstacles (rigid geometric shapes) are carefully placed throughout the device domain and deflect particles of different size in different directions

to cause continuous size based separation [42]. The first type of device in this category is known as a geometric ratchet which was conceptualized in the late 1990s [43-44]. This device rectifies the Brownian motion of particles so that each particle size follows a different trajectory in the device based on their Brownian diffusion coefficient [45]. This was realized experimentally by constructing a silicon micro-wafer device which could sort DNA in the range of 15-30 kbp continuously[46]. A related idea for a separation device relies on the asymmetric bifurcation of laminar flow and a deterministic displacement of particles as opposed to stochastic ratcheting [42, 47]. The deterministic displacement is achieved utilizing a carefully designed obstacle course inside the separation device such as one schematically shown in Figure 1-2. On imposing a laminar flow, particles smaller than a specific size (which is dependent on the device and obstacle geometry) follow the flow streamlines. However, larger particles get displaced laterally each time they encounter an obstacle. This concept was verified experimentally for two different systems - submicron PS particles of sizes 0.8, 0.9 and 1 μm and blood cells. In both cases, electrophoresis was used to drive particles down the obstacle course.

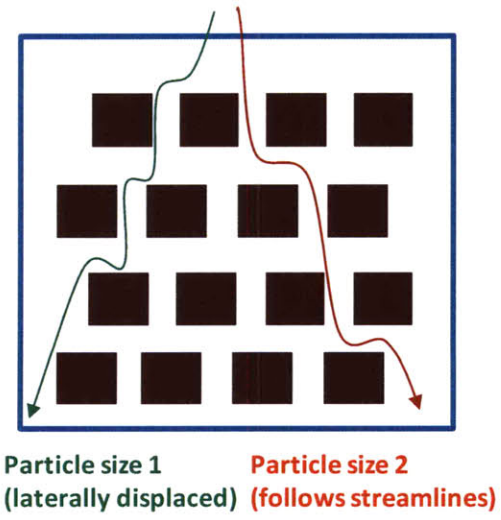

Figure 1-2: Schematic of deterministic displacement devices (based on [47])

1.1.3.2 Field Driven Separations

Various fields have been used to drive separation – electric, magnetic, centrifugal, gravity, light and even ultrasound in certain cases.

Separation using the centrifugal field still remains one of the most widely employed methods for particle separation in the industry. Size fractionation can be carried out using *differential centrifugation* in which a mixed population of particles is subjected to increasing gravitational force resulting in their sequential sedimentation. In this sequence, the larger particles sediment first and smaller particles sediment once gravitational force is sufficiently large. For differential centrifugation of ultrafine particles, multiple centrifugation stages may need to be used to improve capture efficiency and resolution.

Separations driven by an electric field are also quite common. *Gel electrophoresis* is frequently used for the analysis of polymeric and biological samples which differ in charge, size and sometimes shape and is based on the difference in electrophoretic mobility in an applied electric field [48]. However, it is difficult to separate cells and sub-cellular structures using gel electrophoresis due to limited range of achievable pore sizes, and difficulties in sample loading and recovery [43]. Recently, *capillary zone electrophoresis* (CZE) was shown to be a useful analytical technique for the separation of sub-micron polymers and bioparticles [49]. Separation in CZE, which occurs even in the absence of a gel, depends upon the action of three forces – the electrokinetic force due to the applied field, the stokes drag and the electrophoretic retardation force due to the motion of counter ions in the opposite direction in the double layer. Separation was demonstrated using CZE for PS particles having radii between 139 and 381 nm [50]. Another technology for replacing electrophoretic gels is emerging. The rapid development of nano-fabrication techniques in the past few years has allowed fabrication of nano-filter arrays with a gap-size of tens of nano-meters. These custom filters have the potential of being utilized for electrophoretic separations as demonstrated recently [51].

The above electrophoretic techniques are all elution based. The phenomenon of *Dielectrophoresis* (DEP) has been utilized for driving continuous separations. The DEP force is proportional to the electric field gradient and the volume of the particle – a fact that can be exploited for causing separation. Kang et al constructed a microfluidic DEP device for separating PS particles sized between 5 and 15 μm [52]. An interesting feature of their device was the careful positioning of an insulating block inside the microchannel for locally dehomogenizing the electric field. Large field gradients were generated which produced a significant DEP force on the particles resulting in their continuous size fractionation. Kralj et al also developed a device for continuous fractionation of PS beads between 4.1 μm and 6 μm using a series of interdigitated electrodes inside a microchannel [53]. The presence of interdigitated electrodes caused a periodic variation of the electric field inside the channel producing large field gradients. Other setups for DEP separation have been reported which utilize a quadrupole electrode setup for separating micron sized particles [54]. Recently, Liu et also looked at combining DEP with magnetophoresis in order to be better able to manipulate magnetic particles in a microfluidic device and were able to generate forces on the piconewton scale [55]. The concept of DEP was also applied for dynamically fractionating viable cells from nonviable ones by utilizing a moving electric field [56].

Field flow fractionation (FFF) techniques are another family of elution based techniques that utilize external fields for separation. All of them operate with the same underlying principle – when a field is applied perpendicular to the flow direction of a particle mixture, particles of different sizes attain different equilibrium positions since the applied force is size dependent. Then, in the presence of a parabolic flow profile, difference in longitudinal position causes particles to elute at different times. A detailed review of these techniques can be found at various places in literature [57-58].

1.1.3.3 Magnetophoretic separations

Magnetic separations have traditionally been used in the industry for enrichment of iron ore or removal of ferromagnetic impurities from water and clay [59] and in the mineral

industry [60]. Also, minerals of differing densities have been separated using magnetohydrostatic separations [61]. In recent years, there has been extensive work in biological separations using magnetic particles because they are economical, offer mild operating conditions and provide large efficiencies [62]. Most of these separations involve small magnetic particles which attach themselves chemically or physically to the non-magnetic species being separated [59, 63]. However, devices have been developed utilizing the phenomenon of magnetophoresis where separation is based on the difference in inherent magnetic properties or size of the particles. Separations of this latter type are more relevant for size fractionation of submicron particles. The force expression for a magnetophoretic force is given as [64]

$$F_m = \mu_0 V_p (\chi_p - \chi_f) H \nabla H \tag{1.1}$$

Here μ_0 is the permeability of free space, V_p is the volume of the particle, χ_p and χ_f are the magnetic susceptibilities of the particle and the fluid respectively and H is the applied magnetic field. Based on the sign of $(\chi_p-\chi_f)$ magnetophoretic separations could be characterized as positive or negative magnetophoresis.

In *positive magnetophoresis*, separation is achieved by attracting particles of higher magnetic susceptibility (i.e. paramagnetic and ferromagnetic particles) and larger size towards regions of high field. $(\chi_p-\chi_f)$ is positive for these separation systems. Due to the nature of magnetic force, smaller particles and particles with lower magnetic susceptibility are not attracted to the same extent. Continuous separation of magnetic and non-magnetic microparticles was carried out in a microfluidic chip based on the above principle [62]. When magnetic particles were pumped into a laminar flow chamber and a magnetic field was applied perpendicular to the flow direction, particles deviated from laminar flow to varying extents depending on their size and magnetic susceptibility. They were withdrawn continuously from different locations in the device. The above device was used later to separate mouse macrophages from human ovarian cancer cells tagged with magnetic nanoparticles [65].

In magnetic separations, often iron wires or other obstacles are introduced into the separation device to dehomogenize the field generate large field gradients to enhance separation efficiency. Takayasu et al described separations using a paramagnetic capture mode (PCM) which essentially utilizes positive magnetophoresis to capture paramagnetic particles on a wire surface [66]. This group utilized PCM to continuously separate red blood cells (RBCs) from white blood cells (WBCs) using a magnetic wire and a superconducting magnet [67].

Other groups have attempted to separate blood continuously using a paramagnetic or a diamagnetic capture mode (DCM) in a microdevice. The idea was further extended to a multi-stage device to improve capture resolution and efficiency [68-70].

In *negative magnetophoresis*, diamagnetic particles are pushed towards regions of decreasing magnetic field and ultimately get trapped at the points where field gradient vanishes. The magnetic force is dependent on the susceptibility difference between the particle and the fluid. Thus, $(\chi_p-\chi_f)$ is negative for these systems because χ_p is close to zero for diamagnetic particles. Thus, a diamagnetic particle immersed in a continuum ferrofluid experiences a "magnetic pressure" or magnetic buoyancy force which causes negative magnetophoresis [71].

Since the force expression has a negative sign, the diamagnetic particles move towards regions of decreasing magnetic field gradient. In addition, the force is also proportional to the volume of the particle. Thus, diamagnetic particles of differing sizes can be subjected to forces of differing magnitude by immersing them in a ferrofluid and subjecting them to an inhomogeneous magnetic field. To demonstrate this phenomenon experimentally, polystyrene particles of sizes 510 nm and 840 nm were immersed in a magnetite ferrofluid and exposed to a decaying magnetic field in a capillary. The time required to trap these particles near the stationary point of the field was shown to be size dependent. Later, this concept was extended to design a continuous separation technique for these particles [72]. In a separate study, particles of the above two sizes immersed in a ferrofluid were trapped at separate locations in a microfluidic device by applying a saw

tooth magnetic field of increasing intensity [73-74]. Other groups have also explored trapping and three dimensional self assembly into spherical and ellipsoidal shapes of non-magnetic particles immersed in a ferrofluid due to magnetic pressure [75]. Recently, Krebs et al [76] recently demonstrated the use of negative magnetophoresis for ordering biological cells into linear arrangements using inert cytocompatible magnetic nanoparticles.

1.1.4 The need for a macro scale technique for submicron separations

Most of the technologies that exist currently for separations in the submicron range are microscale techniques. At this scale, these devices are suitable for fast and accurate analysis. However, the throughput of these miniaturized devices makes them unsuitable for lab-scale or industrial preparative separations. In many cases, scaling up these devices to a macroscale would result in breakdown on basic principle of separation which is specific to the microscale. The few macroscale conventional techniques that exist have their share of problems. Centrifugation for separation of ultrafine particles suffers from two major problems – poor recovery and low resolution for any particular size [77]. This problem may be addressed by performing multi-stage centrifugation but it makes the process cumbersome, time consuming and uneconomical. Filtration can be a very effective tool for isolating particles from a suspension but not so much for size fractionation. It is difficult to narrow the PSD of a polydisperse sample and to fractionate particles between close size ranges using membrane filtration. Also, operational difficulties such as membrane fouling are encountered. Size exclusion chromatography (SEC) also suffers from the difficulty of sorption of particles by the column stationary phase [32]. The other known issue with SEC is the difficulty encountered when scaling up the technology for preparative separations. In addition, SEC is not a continuous process which makes it difficult for use in the industry. All these difficulties underline a need for a novel continuous separation technique for performing submicron particle separations at a large scale. This thesis will attempt to utilize negative magnetophoresis to develop a technology for continuously separating sub-micron particles.

The ability to utilize "magnetic pressure" for separating even non-magnetic components in the presence of a magnetic fluid makes this separation method universally applicable. Magnetic separation techniques also have other several advantages when compared to other conventional separation techniques [59, 63]. Equipment for magnetophoretic separations is much simpler when compared to mechanically complex centrifuges, filtration equipment or even chromatography columns. Presence of large amount of cell or biological debris and other particulate matter does not affect magnetic separation which makes it ideal for bioseparation at a sub-micron level. In addition, magnetic separation techniques are marked by low shear when compared to conventional techniques. This gentleness is a great advantage when separating brittle materials and biological cells, viruses or sub-cellular organelles which are prone to lyses. In addition, magnetic separations lend themselves to easy scale up. All these factors make magnetic separations ideal for the industry.

1.2 Thesis Objectives

The goal of this thesis was to conceptualize techniques for performing size based separation of submicron non-magnetic particles using a magnetic fluid utilizing magnetophoretic forces. When a non-magnetic particle is immersed in a magnetic fluid and subjected to an inhomogeneous magnetic field, a magnetic buoyancy force acts on this particle in the direction of decreasing magnetic field as shown in Equation (1.1). The specific goals of this thesis are concerned with exploring this driving force for developing a novel separation technology:

A. **Fundamental investigation of new ideas for fractionation of submicron particles using magnetophoresis.** The novel separation technique proposed in this thesis consists of an obstacle course in the form of circular iron wires or other asymmetric shapes. These obstacles have the capacity to generate large magnetic field gradients which provide the driving force for separation. Designing the geometric placement, size and shape of these obstacles so as to channel the magnetic buoyancy force for

performing size fractionation of particles was the first important goal of this thesis. This was divided into further specific tasks as follows

a. **Performing two dimensional particle tracking simulations to understand the behavior of a single nonmagnetic particle in the presence of an obstacle course.** The focus was on understanding the variation of particle motion with size for a given obstacle course. This understanding would be helpful in further developing an understanding of a separation system exploiting magnetophoretic forces.

b. **Performing particle tracking simulations for experimental system design.** Once the physics of particle behavior had been described through simulations, and a novel concept for the separation system had been proposed, the geometric design and operating conditions for an experimental set up could be optimized using simulations. Also, three dimensional particle tracking simulations could be performed on the experimental setup to predict performance of the separation system.

B. **Experimental investigation of the proposed ideas.** An experimental demonstration was necessary to complement design based on simulations and helpful in further illustrating the separation principle. This was performed in two ways:

a. **Visualization experiments.** Fluorescence microscopy experiments were performed to visually observe size dependent capture of submicron nonmagnetic fluorescent particles.

b. **Quantification experiments.** To gain a quantitative understanding of capture and separation performance of the experimental system, pulse chromatography experiments were performed with mixtures of fluorescent particles and magnetic fluid.

1.3 Thesis Overview

The following chapters of the thesis describe progress on these goals in greater detail. In Chapter 2, we explore the fundamental physics behind magnetophoretic forces, develop the single particle trajectory model and describe results from simulations around various obstacle course geometries. In Chapter 3, we describe the experimental work performed as part of this thesis – both capture visualization and capture quantification experiments. Finally, in Chapter 4, we summarize the work in this thesis and explore some avenues for future work.

1.4 References

1. Martin-Banderas, L., et al., *Flow focusing: A versatile technology to produce size-controlled and specific-morphology microparticles.* Small, 2005. **1**(7): p. 688.

2. Van Hee, P., et al., *Strategy for selection of methods for separation of bioparticles from particle mixtures.* Biotechnology and Bioengineering, 2006. **94**(4): p. 689.

3. http://www.malvern.co.uk/ProcessEng/industries/metalpowders/overview.htm, *Metal Powders Industry Overview.*

4. Elghanian, R., et al., *Selective colorimetric detection of polynucleotides based on the distance-dependent optical properties of gold nanoparticles.* Science, 1997. **277**(5329): p. 1078-1081.

5. Goodrich, G.P., et al., *Effect of macromolecular crowding on DNA : Au nanoparticle bioconjugate assembly.* Langmuir, 2004. **20**(23): p. 10246-10251.

6. Dykman, L.A., et al., *A protein assay based on colloidal gold conjugates with trypsin.* Analytical Biochemistry, 2005. **341**(1): p. 16-21.

7. Rodriguez-Fernandez, J., et al., *Seeded growth of submicron Au colloids with quadrupole plasmon resonance modes.* Langmuir, 2006. **22**(16): p. 7007.

8. Nie, S.M. and S.R. Emery, *Probing single molecules and single nanoparticles by surface-enhanced Raman scattering.* Science, 1997. **275**(5303): p. 1102-1106.

9. Elechiguerra, J.L., L. Larios-Eopez, and M. Jose-Yacaman, *Controlled synthesis of platinum submicron and nanometric particles with novel shapes.* Applied Physics A: Materials Science and Processing, 2006. **84**(1-2): p. 11.

10. Sanles-Sobrido, M., et al., *Design of SERS-Encoded, Submicron, Hollow Particles Through Confined Growth of Encapsulated Metal Nanoparticles.* Journal Of The American Chemical Society, 2009. **131**(7): p. 2699-2705.

11. Mastai, Y., et al., *TiO2 nanocrystalline pigmented polyethylene foils for radiative cooling applications: Synthesis and characterization.* Langmuir, 2001. **17**(22): p. 7118-7123.

12. Mine, E., et al., *Synthesis of submicrometer-sized titania spherical particles with a sol-gel method and their application to colloidal photonic crystals.* Journal Of Colloid And Interface Science, 2005. **291**(1): p. 162-168.

13. Friedel, B. and S. Greulich-Weber, *Preparation of monodisperse, submicrometer carbon spheres by pyrolysis of melamine-formaldehyde resin.* Small, 2006. **2**(7): p. 859-863.

14. Colvin, V.L., *From opals to optics: Colloidal photonic crystals.* Mrs Bulletin, 2001. **26**(8): p. 637-641.

15. Fudouzi, H. *Soft opal films with tunable structural color and their applications.* 2005. Boston, MA, United States: International Society for Optical Engineering, Bellingham WA, WA 98227-0010, United States.

16. Hwa-Young, K., S. Hyunjung, and M. Jooho. *Preparation of inks with monodisperse colloidal silica and their self-assembly in a ink-jet printed droplet.* 2003. San Francisco, CA, USA: Mater. Res. Soc.

17. Yang, Y., et al., *Organic/polymeric electroluminescent devices processed by hybrid ink-jet printing.* Journal Of Materials Science-Materials In Electronics, 2000. **11**(2): p. 89-96.

18. Katstra, W.E., et al., *Oral dosage forms fabricated by Three Dimensional Printing (TM).* Journal Of Controlled Release, 2000. **66**(1): p. 1-9.

19. Wang, H., et al., *Monodisperse spherical core-shell-structured phosphors obtained by functionalization of silica spheres with Y_2O_3:Eu^{3+} layers for field emission displays.* Applied Physics Letters, 2005. **87**(18): p. 181907.

20. Graf, C. and A. Van Blaaderen, *Metallodielectric colloidal core-shell particles for photonic applications.* Langmuir, 2002. **18**(2): p. 524.

21. Choi, S.-H., et al., *Simple and Generalized Synthesis of Oxide–Metal Heterostructured Nanoparticles and their Applications in Multimodal Biomedical Probes.* Journal Of The American Chemical Society, 2008. **130**(46): p. 15573-15580.

22. Brasuel, M., et al., *Fluorescent nanosensors for intracellular chemical analysis: Decyl methacrylate liquid polymer matrix and ion exchange-based potassium PEBBLE sensors with real-time application to viable rat C6 glioma cells.* Analytical Chemistry, 2001. **73**(10): p. 2221-2228.

23. Joumaa, N., et al., *Synthesis of quantum dot-tagged submicrometer polystyrene particles by miniemulsion polymerization.* Langmuir, 2006. **22**(4): p. 1810.

24. Brown, K.R., D.G. Walter, and M.J. Natan, *Seeding of colloidal Au nanoparticle solutions. 2. Improved control of particle size and shape.* Chemistry Of Materials, 2000. **12**(2): p. 306-313.

25. Nagasawa, H. and K. Mae, *Development of a new microreactor based on annular microsegments for fine particle production.* Industrial & Engineering Chemistry Research, 2006. **45**(7): p. 2179-2186.

26. A. Akthakul, A.H., F. Stellacci, A. M Mayes, *Size Fractionation of Metal Nanoparticles by Membrane Filtration.* Advanced Materials, 2005. **17**(5): p. 532-535.

27. Goia, D.V. and E. Matijevic, *Tailoring the particle size of monodispersed colloidal gold.* Colloids And Surfaces A-Physicochemical And Engineering Aspects, 1999. **146**(1-3): p. 139-152.

28. Ghosh, S., *Functional Coatings: By Polymer Microencapsulation.* 2006: Wiley-VCH. pp.86.

29. Ladisch, M.R., *Bioseparations Engineering*. 2001.

30. Kirkland, J.J., *High-Performance Size-Exclusion Liquid-Chromatography Of Inorganic Colloids.* Journal Of Chromatography, 1979. **185**(DEC): p. 273-288.

31. Fischer, C.H., *Analysis Of Colloids .6. Semiconductor Colloids Of High Monodispersity By Preparative Size-Exclusion Chromatography.* Journal Of Liquid Chromatography, 1994. **17**(17): p. 3593-3611.

32. Wei, G.T. and F.K. Liu, *Separation of nanometer gold particles by size exclusion chromatography.* Journal Of Chromatography A, 1999. **836**(2): p. 253-260.

33. Ahuja, S., *Handbook of Bioseparations*. 2000, San Diego: Academic Press.

34. Blom, M.T., et al., *On-chip hydrodynamic chromatography separation and detection of nanoparticles and biomolecules.* Analytical Chemistry, 2003. **75**(24): p. 6761-6768.

35. Zhang, X.L., et al., *Continuous flow separation of particles within an asymmetric microfluidic device.* Lab On A Chip, 2006. **6**(4): p. 561-566.

36. Yamada, M., M. Nakashima, and M. Seki, *Pinched flow fractionation: Continuous size separation of particles utilizing a laminar flow profile in a pinched microchannel.* Analytical Chemistry, 2004. **76**(18): p. 5465-5471.

37. Sai, Y., et al., *Continuous separation of particles using a microfluidic device equipped with flow rate control valves.* Journal of Chromatography A, 2006. **1127**(1-2): p. 214.

38. Yamada, M. and M. Seki, *Hydrodynamic filtration for on-chip particle concentration and classification utilizing microfluidics.* Lab On A Chip, 2005. **5**(11): p. 1233-1239.

39. Yamada, M. and M. Seki, *Microfluidic particle sorter employing flow splitting and recombining.* Analytical Chemistry, 2006. **78**(4): p. 1357-1362.

40. VanDelinder, V. and A. Groisman, *Perfusion in microfluidic cross-flow: Separation of white blood cells from whole blood and exchange of medium in a continuous flow.* Analytical Chemistry, 2007. **79**(5): p. 2023.

41. Di Carlo, D., et al., *Equilibrium separation and filtration of particles using differential inertial focusing.* Analytical Chemistry, 2008. **80**(6): p. 2204.

42. Fu, J., et al., *A patterned anisotropic nanofluidic sieving structure for continuous-flow separation of DNA and proteins.* Nat Nano, 2007. **2**(2): p. 121.

43. Ertas, D., *Lateral separation of macromolecules and polyelectrolytes in microlithographic arrays.* Physical Review Letters, 1998. **80**(7): p. 1548-1551.

44. Duke, T.A.J. and R.H. Austin, *Microfabricated sieve for the continuous sorting of macromolecules.* Physical Review Letters, 1998. **80**(7): p. 1552-1555.

45. van Oudenaarden, A. and S.G. Boxer, *Brownian Ratchets: Molecular Separations in Lipid Bilayers Supported on Patterned Arrays.* Science, 1999. **285**(5430): p. 1046-1048.

46. Chou, C.F., et al., *Sorting by diffusion: An asymmetric obstacle course for continuous molecular separation.* Proceedings Of The National Academy Of Sciences Of The United States Of America, 1999. **96**(24): p. 13762-13765.

47. Huang, L.R., et al., *Continuous particle separation through deterministic lateral displacement.* Science, 2004. **304**(5673): p. 987-990.

48. al, R.G.H.e., *Bioseparations Science and Engineering.* 2003, New York: Oxford University Press.

49. Radko, S.P. and A. Chrambach, *Separation and characterization of sub-mu m- and mu m-sized particles by capillary zone electrophoresis.* Electrophoresis, 2002. **23**(13): p. 1957-1972.

50. Radko, S.P., M. Stastna, and A. Chrambach, *Capillary zone electrophoresis of sub-mu m-sized particles in electrolyte solutions of various ionic strengths: Size-dependent electrophoretic migration and separation efficiency.* Electrophoresis, 2000. **21**(17): p. 3583-3592.

51. Fu, J.P., P. Mao, and J.Y. Han, *Nanofilter array chip for fast gel-free biomolecule separation.* Applied Physics Letters, 2005. **87**(26).

52. Kang, K.H., et al., *Continuous separation of microparticies by size with direct current-dielectrophoresis.* Electrophoresis, 2006. **27**(3): p. 694-702.

53. Kralj, J.G., et al., *Continuous dielectrophoretic size-based particle sorting.* Analytical Chemistry, 2006. **78**(14): p. 5019-5025.

54. Tsukahara, S., K. Yamanaka, and H. Watarai, *Flow fractionation of microparticles under a dielectrophoretic field in a quadrupole electrode capillary.* Analytical Chemistry, 2001. **73**(23): p. 5661-5668.

55. Liu, C., L. Lagae, and G. Borghs, *Manipulation of magnetic particles on chip by magnetophoretic actuation and dielectrophoretic levitation.* Applied Physics Letters, 2007. **90**(18): p. 184109-3.

56. Kua, C.H., et al., *Dynamic Cell Fractionation and Transportation Using Moving Dielectrophoresis.* Analytical Chemistry, 2007. **79**(18): p. 6975-6987.

57. Giddings, J.C., *Field-Flow Fractionation - Analysis of Macromolecular, Colloidal, and Particulate Materials.* Science, 1993. **260**(5113): p. 1456-1465.

58. Colfen, H. and M. Antonietti, *Field-flow fractionation techniques for polymer and colloid analysis*, in *New Developments In Polymer Analytics I.* 2000. p. 67-187.

59. Safarik, I. and M. Safarikova, *Use of magnetic techniques for the isolation of cells.* Journal Of Chromatography B, 1999. **722**(1-2): p. 33-53.

60. Svoboda, J., *Magnetic methods for the treatment of minerals.* 1987, Dordrecht, Netherlands: Kluwer Academic Publishers.

61. Jakabsky, S., et al., *Utilization of ferromagnetic fluids in mineral processing and water treatment.* Journal Of Radioanalytical And Nuclear Chemistry, 2000. **246**(3): p. 543-547.

62. Pamme, N. and A. Manz, *On-chip free-flow magnetophoresis: Continuous flow separation of magnetic particles and agglomerates.* Analytical Chemistry, 2004. **76**(24): p. 7250.

63. Safarik, I. and M. Safarikova, *Magnetic techniques for isolation and purification of proteins and peptides.* BioMagnetic Research and Technology, 2004. **2**(7).

64. Gonzalez L A, S.F., K A Smith, T A Hatton, *Magnetophoresis of Nonmagnetic, Submicrometer Particles in Magnetic Fluids.* SMA Transactions in Molecular Engineering of Biological and Chemical Systems (http://dspace.mit.edu), 2004.

65. Pamme, N., J.C.T. Eijkel, and A. Manz, *On-chip free-flow magnetophoresis: Separation and detection of mixtures of magnetic particles in continuous flow.* Journal of Magnetism and Magnetic Materials, 2006. **307**(2): p. 237.

66. Takayasu, M., E. Maxwell, and D.R. Kelland, *Continuous Selective Hgms In The Repulsive Force Mode.* Ieee Transactions On Magnetics, 1984. **20**(5): p. 1186-1188.

67. Takayasu, M., D.R. Kelland, and J.V. Minervini, *Continuous magnetic separation of blood components from whole blood.* Ieee Transactions On Applied Superconductivity, 2000. **10**(1): p. 927-930.

68. Han, K.H. and A.B. Frazier, *Continuous magnetophoretic separation of blood cells in microdevice format.* Journal Of Applied Physics, 2004. **96**(10): p. 5797-5802.

69. Han, K.H. and A.B. Frazier, *Paramagnetic capture mode magnetophoretic microseparator for high efficiency blood cell separations.* Lab On A Chip, 2006. **6**(2): p. 265-273.

70. Han, K.-H. and A.B. Frazier, *Diamagnetic capture mode magnetophoretic microseparator for blood cells.* Journal of Microelectromechanical Systems, 2005. **14**(6): p. 1422.

71. Rosensweig, R.E., *Ferrohydrodynamics*. 1985, London: Cambridge University Press.

72. Fateen, S.-E.K., *Magnetophoretic focusing on submicron particles dispersed in a polymer-stabilized magnetic fluid.* 2002, Massachusetts Institute of Technology: Cambridge MA.

73. Park, E.S., et al., *Size-Selective magnetophoretic trapping of submicrometer non-magnetic particles immersed in a magnetic nano-fluid.* in preparation.

74. Gonzalez , L., *Negative magnetophoresis of submicron species in magnetic nanofluids*, in *Chemical Engineering*. 2008, MIT: Cambridge MA.

75. Feinstein, E. and M. Prentiss, *Three-dimensional self-assembly of structures using the pressure due to a ferrofluid in a magnetic field gradient.* Journal Of Applied Physics, 2006. **99**(6).

76. Krebs, M.D., et al., *Formation of Ordered cellular structures in suspension via label-free negative magnetophoresis.* Nano Lett. Nano Letters, 2009. **9**(5): p. 1812-1817.

77. Graham, J., *Biological Centrifugation*. 2001, Cornwall, UK: TJ International.

Chapter 2

Particle Trajectory Simulations

2.1 Introduction

The first goal of this thesis was to investigate novel methods for performing size based separation of submicron non-magnetic particles through the use of magnetic buoyancy forces. These forces are generated by immersing the particles in a magnetic environment and subjecting them to an obstacle course in the form of circular iron obstacles or other, asymmetric shapes. An obstacle course has the ability to generate large magnetic field gradients – the driving force for separation. In order to be able to design and optimize the shape and geometric arrangement of the obstacle course, an in-depth understanding of physics of particle behavior in such an environment is essential. This chapter describes the results from modeling and simulations performed to understand the physics of non-magnetic particles around an obstacle array. The basic physics behind generation of Magneto Quasi Static (MQS) fields will be described first and the expression for magnetic buoyancy force on a non-magnetic particle will be derived based on work done by Rosensweig [1]. Results from an analysis of order of magnitude of various forces in the system will be presented to understand the feasibility of separation. A particle trajectory tracking model developed to understand the behavior of non-magnetic particles around obstacle arrays will be presented. Simulations were performed using MATLAB and COMSOL using this trajectory model. The details of the particle tracking model, the methodology of simulation and key results will be discussed in a later section. Lastly, this chapter will present a discussion on optimizing the design of obstacle geometry and system operating conditions for separating a mixture of two given particle sizes.

2.2 Maxwell's equations for magneto quasi-static systems

The forces used for separating particles in this thesis were generated using magnetic fields. Magnetic fields can be produced either by currents or changing electric fields. Thus, the electric and magnetic fields in any system are coupled. The four principle equations which describe the physics of electric and magnetic fields and their interactions are known as Maxwell's equations. These equations are shown in equation (2.1) to (2.4) and capture the entire theoretical content of classical electrodynamics [2].

$$\underline{\nabla} \cdot \underline{D} = \rho_f \tag{2.1}$$

$$\underline{\nabla} \cdot \underline{B} = 0 \tag{2.2}$$

$$\underline{\nabla} \times \underline{E} = -\frac{\partial \underline{B}}{\partial t} \tag{2.3}$$

$$\underline{\nabla} \times \underline{H} = \underline{J}_f + \frac{\partial \underline{D}}{\partial t} \tag{2.4}$$

In the above equations, $\underline{D}$ denotes the displacement current, ρ_f denotes the free charge density, $\underline{B}$ the magnetic field induction, $\underline{E}$ the electric field, $\underline{H}$ the magnetic field and $\underline{J}_f$ the free electric current. This thesis is only concerned with time-invariant fields along with an absence of electric currents. Also, it can be assumed that the variation of magnetic fields is slow enough that they are not coupled with the electric fields. This allows simplification of equations 2.3 and 2.4 further, so as to obtain (2.5) and (2.6),

$$\underline{\nabla} \times \underline{E} = 0 \tag{2.5}$$

$$\underline{\nabla} \times \underline{H} = 0 \tag{2.6}$$

In addition to the Maxwell's equations, to completely solve for the electric and magnetic fields, two sets of information are necessary - constitutive equations: relating magnetic induction $\underline{B}$ with magnetic field $\underline{H}$ and electric displacement current $\underline{D}$ with electric field $\underline{E}$ and boundary conditions: for both electric and magnetic fields. The constitutive equations are presented in equations (2.7) and (2.8).

$$\underline{B} = \mu_0(\underline{H} + \underline{M}) \tag{2.7}$$

$$\underline{D} = \varepsilon_0 \underline{E} + \underline{P} \tag{2.8}$$

Here, $\underline{M}$ denotes magnetization and $\underline{P}$ denotes the polarization of the material. The systems in this thesis assume a time invariance of $\underline{E}$ and $\underline{H}$ fields and collinearity of $\underline{M}$ and $\underline{H}$. For this special case, boundary conditions are given by equations (2.9) and (2.10)

$$\underline{n}.(\underline{B}_1 - \underline{B}_2) = 0 \tag{2.9}$$

$$\underline{n} \times (\underline{H}_2 - \underline{H}_1) = 0 \tag{2.10}$$

Equation (2.9) states that the normal component of B is continuous across the interface, a result which follows directly from equation (2.2) on application of the divergence theorem. Similarly, equation (2.10) states that the tangential component of $\underline{H}$ is continuous across the interface. This follows from equation (2.6) on application of the Stokes theorem and is valid only in the special case of absence of currents.

For the purpose of this thesis, finite element methods (FEM) were used to solve for magnetic fields generated by various arrangements of iron obstacles using the *COMSOL Multiphysics* software (Comsol AB). In the magnetostatics application mode, *COMSOL* formulates the solution of magnetic fields in terms of a magnetic vector potential ($\underline{A}$) to aid the numerical solution of Maxwell's equations. The vector potential $\underline{A}$ is defined by equation (2.11)

$$\underline{B} = \underline{\nabla} \times \underline{A} \tag{2.11}$$

Using this definition, equation (2.6) can be represented in terms of potential as [3]

$$\underline{\nabla} \times (\mu_0 \underline{\nabla} \times \underline{A} - \underline{M}) = 0 \tag{2.12}$$

This equation could now be solved in conjunction with a magnetic field continuity boundary condition as described in equation (2.10) if the applied magnetic field value is known. In the presence of magnets, when the applied magnetic field is not known and has to be solved for, the magnetic insulation boundary condition described in equation (2.13) can be used.

$$A_z = 0 \tag{2.13}$$

This condition sets the magnetic field tangential to boundary far away from a magnet appropriately to zero since field lines run as closed loops around a magnet. Once a magnetic field distribution ($\underline{H}$) has been determined, the field gradient ($\underline{\nabla}H$) is obtained numerically using MATLAB. The next section discusses how magnetic buoyancy forces arise on a nonmagnetic species.

2.3 Magnetic buoyancy forces on a non-magnetic particle

2.3.1 Derivation of magnetic buoyancy force

Performing size based separation for sub-micrometer sized particles requires application of a force that has two characteristics – the force scales with size of particles and it should be able to act significantly at the sub-micron scale without losing its efficacy when the separation system is scaled up. The magnetic buoyancy force satisfies both these characteristics. In this section, the origin of this force will be described through a brief derivation adapted from a more detailed derivation provided in Rosensweig [1]. This derivation is valid for hydrostatic systems. Gonzalez [4] showed that the magnetic buoyancy force expression resulting from systems incorporating viscous effects due to flow is no different, since the additional viscous forces on the particles translate to fluid drag on the particle.

For deriving the magnetic buoyancy force immersed in a magnetic fluid, consider the non-magnetic object shown in Figure 2.1. In the figure shown, the non-magnetic body is immersed in a magnetic medium. The expression for net force acting on the body can be attributed to two components – the contribution from stresses exerted by the magnetic fluid on the body and the body force due to gravity. This is shown in equation 2.14

$$\underline{F_p} = \oint_S \underline{n}.\underline{\underline{T_m}}\,dS + \int_V \rho_p \underline{g}\,dV \tag{2.14}$$

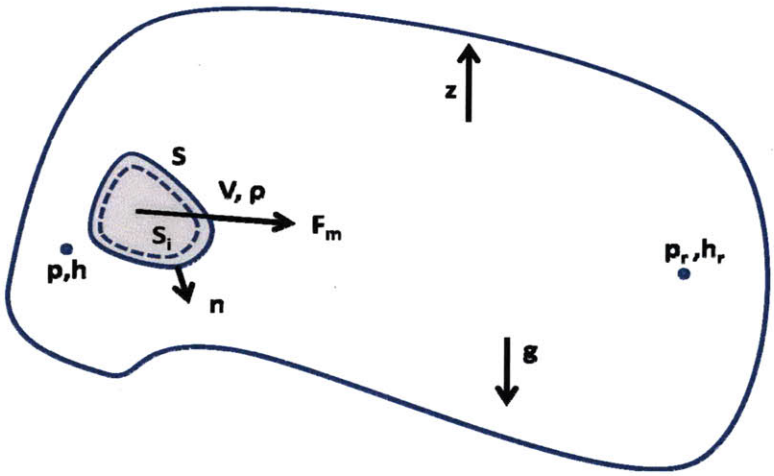

Figure 2-1 - Description of system for developing the expression for magnetic buoyancy force on a non-magnetic particle.

In the above equation, the integral is evaluated over the surface of the non-magnetic object, ρ_p is the density of the particle, g is the acceleration due to gravity and V is the volume of the particle. $\underline{\underline{T}}_m$ is the magnetic stress tensor defined by Rosensweig [1] as given in equation 2.15

$$\underline{\underline{T}}_m = -\left\{ p(\rho,T) + \int_0^H \mu_0 \left[\frac{\partial(\nu M)}{\nu} \right]_{H,T} dH + \frac{1}{2}\mu_0 H^2 \right\} \underline{\underline{I}} + \underline{B}\underline{H} \tag{2.15}$$

In order to conveniently evaluate the integral in equation (2.14), we can use the definition of composite pressure (p^*) which is defined by Rosensweig as [1]

$$p^* = p(\rho,T) + \mu_0 \int_0^H \left(\frac{\partial M}{\partial \nu} \right)_{H,T} dH + \mu_0 \int_0^H M dH \tag{2.16}$$

The magnetic stress tensor can now be written in terms of composite pressure as follows

$$\underline{\underline{T}}_m = -\left\{ p^* + \frac{1}{2}\mu_0 H^2 \right\} \underline{\underline{I}} + \underline{B}\underline{H} \tag{2.17}$$

To simplify the evaluation of composite pressure, the Ferrohydrodynamic Bernoulli Equation (FBE) can be used to represent p^* in terms of other known quantities. The FBE gives [1]

$$p^* + \rho_f gz + \frac{1}{2}\rho v^2 - \mu_0 \bar{M}H = \text{constant}$$

where,

$$\bar{M}H = \int_0^H M dH \tag{2.18}$$

Applying FBE between the location of the object and a reference point 'r' where a magnetic field is absent for the system in Figure 2.1, we can represent p^* as follows

$$p^* = p_r + \rho_f gz_r - \rho_f gz + \mu_0 \bar{M}H \tag{2.19}$$

Thus, using (2.17) and (2.19), we can write the force expression as

$$\underline{F_p} = \oint_S \underline{n}.\left\{-\left(p_r + \rho_f gz_r - \rho_f gz + \mu_0 \bar{M}H + \frac{1}{2}\mu_0 H^2\right)\underline{\underline{I}} + \underline{B}\underline{H}\right\} dS + \int_V \rho_p \underline{g} dV \tag{2.20}$$

Expression (2.20) can be simplified after taking the dot product as

$$\underline{F_p} = \oint_S \left\{-\left(p_r + \rho_f gz_r - \rho_f gz + \mu_0 \bar{M}H + \frac{1}{2}\mu_0 H^2\right)\underline{n} + B_n \underline{H}\right\} dS + \int_V \rho_p \underline{g} dV \tag{2.21}$$

Utilizing Gauss theorem,

$$\oint_S A\underline{n} dS = \int_V \underline{\nabla} A dV \tag{2.22}$$

We can simplify the expression in equation (2.21) such that the first two terms containing reference pressure and hydrostatic component of pressure drop out (since they are constant), and the third term represents the body force of fluid on the object,

$$\oint_S -\left(p_r + \rho_f gz_r - \rho_f gz\right)\underline{n} dS = -\int_V \underline{\nabla}\left(\cancel{p_r} + \cancel{\rho_f gz_r} - \rho_f gz\right) dV = \rho_f gV \underline{e_z} \tag{2.23}$$

The third term can be combined with the final term in (2.21) to get the expression for hydrodynamic buoyancy on the object in the absence of magnetic component of the force, such that

$$\underline{F_p}(H=0) = \underline{F_B} = (\rho_f - \rho_p) gV \underline{e_z} \tag{2.24}$$

We have to still evaluate the force terms capturing the effect of magnetic buoyancy forces (terms 4, 5 and 6 in equation (2.21). For this purpose, we can observe that $\underline{H}$ can be broken into the normal and tangential components as

$$\underline{H} = H_n \underline{n} + H_t \underline{t} \tag{2.25}$$

The normal terms can be grouped together and tangential components can be grouped together as

$$\underline{F_m} = \oint_S \left\{ \left(-\mu_0 \bar{M} H - \frac{1}{2} \mu_0 H^2 + B_n H_n \right) \underline{n} + B_n H_t \underline{t} \right\} dS \tag{2.26}$$

Here $\underline{F}_m$ denotes the magnetic component of total force. To simplify evaluation of this force, we can use the fact that that the magnetic component of force just inside the surface of the object is zero. Thus, this gives an expression for the force just inside the surface (denoted by subscript i),

$$0 = \oint_{S_i} \left\{ \left(-\left[\mu_0 \bar{M} H \right]_i - \frac{1}{2} \mu_0 \left[H^2 \right]_i + B_{n,i} H_{n,i} \right) \underline{n} + B_{n,i} H_{t,i} \underline{t} \right\} dS \tag{2.27}$$

We also know the boundary conditions in the absence of a surface current - the normal component of B and tangential component of H are continuous,

$$\begin{aligned} B_n &= B_{n,i} \\ H_t &= H_{t,i} \end{aligned} \tag{2.28}$$

and the normal component of H is related to B through constitutive relations,

$$\begin{aligned} H_n &= \frac{B_n}{\mu_0} \\ H_{n,i} &= \frac{B_n}{\mu_0} - M_n \end{aligned} \tag{2.29}$$

and magnetization just inside the nonmagnetic body is zero

$$M_{n,i} = 0 \tag{2.30}$$

Subtracting equation (2.27) from equation (2.26) and using the relations in (2.28) – (2.30), simple algebraic manipulations allow us to develop an expression for F_m as follows,

$$\underline{F_m} = -\oint_S \left(\frac{1}{2}\mu_0 M_n^{\,2} + \mu_0 \overline{M} H \right) \underline{n} dS \tag{2.31}$$

In the limit of high applied fields, this expression can be further simplified, since generally magnetization is much smaller than the applied magnetic field, hence, $\frac{M_n^2}{\overline{M}H} << 1$. Thus, we obtain

$$\underline{F_m} = -\oint_S \left(\mu_0 \overline{M} H \right) \underline{n} dS \tag{2.32}$$

On applying the Gauss theorem as shown in (2.22) for equation (2.32), we obtain

$$\underline{F_m} = -\oint_S \left(\mu_0 \overline{M} H \right) \underline{n} dS = -\int_V \underline{\nabla} \mu_0 \overline{M} H dV \tag{2.33}$$

We could assume that the particle is small enough that H or M (magnetization of fluid) are essentially constant around the particle i.e. the length scale for variation of field is much larger than the length scale of the particle. The validity of this assumption was recently investigated by Tejwani [5] who showed that for a magnetic particle core size of 10 nm or less, the disruption of fluid magnetization around a nonmagnetic particle is minimal. Thus, a simplified expression for magnetic buoyancy force could be obtained starting from a force balance on the particle given as

$$\underline{F_m} \approx -\mu_0 M_f \nabla H V_p \tag{2.34}$$

This force expression in equation (2.34) is gives the magnetic buoyancy force applied by the magnetic fluid on a non-magnetic particle is proportional to the fluid magnetization (M_f), the magnetic field gradient and volume of the particle (V_p). This expression has been derived for a quiescent fluid (and thus used the hydrostatic case). However, Gonzalez [4] has derived the force expression for the case when there is relative motion between the particle and the fluid, and obtained the exact same expression. For the

quiescent case, two force terms were obtained – the magnetic buoyancy force and the Archimedes' buoyancy force. The only additional term that arises in the situation when particle is moving relative to the fluid is the fluid drag force exerted by the fluid on the particle.

From equation (2.34), numerous inferences can be drawn about the nature of the force. There is a minus sign on the force, which causes the force to act in a direction opposite that of the magnetic field gradient. In addition, the force is proportional to fluid magnetization. So, the more magnetized the fluid, the larger the magnetic buoyancy force. The force is also proportional to the gradient of the field, and not the field itself. Hence, in the presence of a uniform field, there is no magnetic buoyancy force. We need large field gradients in order to generate significant magnetic buoyancy. Finally, and most pertinently for this thesis, this force is proportional to volume of the nonmagnetic particle. Thus, the larger the non-magnetic particle, the stronger the magnetic buoyancy force on it, which forms the underlying principle of separation of particles.

2.3.2 Principle of separation – negative magnetophoresis

As explained in the last section, Equation (2.34) shows the size dependent nature of magnetic buoyancy force – a characteristic that can be exploited to fractionate particles based on their size. A mixture of particles of two different sizes could be suspended in a magnetic environment (e.g. magnetic fluid) and subjected to strong magnetic field gradients (e.g. through an iron obstacle course). The magnetic buoyancy force $F_M \propto R_p^3$ (proportional to cube of particle radius). Thus, particles of different sizes will experience varying level of this force. The migration velocity of particles of different sizes could be calculated by performing a simple force balance assuming the only forces that exist are the Stokes' drag on the particle and the magnetic buoyancy force as

$$-(6\pi\eta R_p)u_m - \mu_0 M_f \nabla H(\frac{4}{3}\pi R_p^3) = 0 \tag{2.35}$$

$$u_m = -\frac{2\mu_0 M_f \nabla H R_p^2}{9\eta} \tag{2.36}$$

This shows that the migration velocity of the particles is proportional to the square of particle size (R_p^2) which allows particles of different sizes to migrate with different velocities, and forms the underlying principle of separation. It is possible to build a separation system which cleverly exploits this difference in migration velocity between two particle sizes and causes separation.

2.3.3 Utilizing magnetizable obstacles to generate field gradients

The magnetic force on a particle was given in Eqn (2.34) as $F_m = -\mu_0 V_p M_f \underline{\nabla} H$. For a homogenous field, $\underline{\nabla} H = 0$ and there is no magnetic force on the particles. For utilizing magnetic forces for separation, external ferromagnetic objects can be introduced to dehomogenize the field. In the presence of a strong enough field, these objects get magnetized to saturation and create large gradients in their immediate vicinity. The effect of introducing a circular obstacle (long wire) in the presence of a uniform field is shown in Fig. 2-2 where we see the presence of large field gradients.

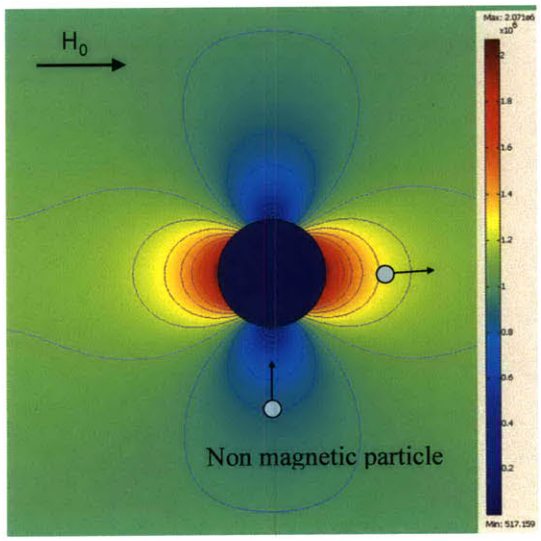

Figure 2-2. Magnetic field gradients generated on applying a uniform horizontal magnetic field in the presence of a long wire and resulting forces on a non-magnetic particle depending on its position.

The negative sign in the force expression tells us that particles will always be "pushed" in the direction of decreasing magnetic field. In the particular case of the wire shown, particles near the horizontal axis will be pushed away and particles near the vertical axis

will be attracted towards the wire as shown in Fig. 2.2. From Eqn. 2.36, we see that the effect of magnetic forces in comparison to fluid drag is proportional to R^2 which means that larger particles will have more deviation from the fluid streamlines compared to smaller particles. In an appropriately constructed device, this difference in magnitude of magnetic forces can be exploited to achieve separation. The variables under our control include intelligent placement of obstacles, control of magnitude and direction of applied magnetic field, and finally the direction and magnitude of approach flow velocity.

2.3.4 Verifying the feasibility of separation using magnetic buoyancy forces

We have seen that, in principle, it is possible to build a separation device based on magnetic buoyancy forces by exploring difference in migration velocities. However, before this idea is explored further, an order of magnitude estimate of the forces needs to be carried out. For the magnetic buoyancy force to be effective at performing size based separation, the order of magnitude of this force has to be comparable with the other forces acting on the particles. There are four major forces acting on the particles which need to be taken into account –

- Magnetic buoyancy force – described in the previous section
- Diffusion force – this force is concentration dependent and acts to move a particle towards regions of lower concentration
- Drag force – This force is exerted by the fluid on the particle and acts in the opposite direction of motion.
- Gravity force – this is due to mass of the particle and acts downward in the vertical direction

An order of magnitude analysis was performed to compare the relative magnitude of these forces along with an estimation of other relevant variables. Results are shown in Table 2-1. Table 2-2 shows the values of parameters used to perform these calculations along with the rationale or reference.

From Table 2-2, it can be seen that the two dominant forces in the system are the magnetic buoyancy force and the viscous drag force, both are which are on the order of a few piconewtons (pN). This magnitude of force is in agreement with other estimates of such forces found in literature [6-7]. It can be seen that the diffusive (10^{-5} pN) and gravity (10^{-4} pN) forces are much smaller than the magnetic buoyancy force and unlikely to significantly influence the motion of a non-magnetic particle which is experiencing magnetophoresis. The magnetophoretic velocity of particles is estimated to be on the order of 1 mm/s which is reasonable for a milli-scale system. The system dimensions are on the order of millimeters, thus, particles with a velocity of this order of magnitude will be able to travel a significant distance in a few seconds. One requirement for the existence of magnetic buoyancy forces is a magnetic environment (i.e. a continuum of magnetic fluid) around the non-magnetic particles. For this requirement to be satisfied, it is important that the magnetic forces on magnetic nanoparticles (composing the magnetic fluid) do not experience a strong magnetophoresis. It can be seen that force on magnetic nanoparticles is on the order of 10^{-3} pN and their migration velocities are on the order of $3*10^{-5}$ m/s which are much smaller than those of non-magnetic particles. Thus, we can assume that a continuum of magnetic nanoparticles will exist around nonmagnetic particles.

In conclusion, an order of magnitude estimate of forces and important variables in the system shows that separation system based on size dependent nature of magnetic buoyancy force is indeed feasible. The principle of the separation system is explained in a later section, which will conceptually describe the initial ideas that were explored in designing the system.

Table 2-1: Results of order of magnitude calculations

Variable	Name	Expression	Value
F_m	Magnetic force on a non-magnetic particle	$\mu_0 V_p M_f \nabla H$	**4.78 pN**
F_v	Drag force	$3\pi\eta V_0 D_p$	**4.71 pN**
F_D	Diffusion force	$\frac{k_B T}{x_p}\nabla x_p$	**4.41 * 10^{-5} pN**
F_g	Force of gravity	$\rho V_p g$	**6.4 * 10^{-4} pN**
$F_{m,mag}$	Magnetic force on magnetic nanoparticles	$\mu_0 V_{p,m} M_p \nabla H$	**8.5 * 10^{-3} pN**
Re	Reynolds number for particle	$V_0 D_p / \nu$	**0.0005**
L_D	Diffusion length	$\sqrt{2Dt_{char}}$, $D = \frac{k_B T}{3\pi\eta D_p}$	**0.419 μm**
u_m	Magnetophoretic migration velocity for non-magnetic particles	$\frac{F_m}{3\pi\eta D_p}$	**10^{-3} m/sec**
$u_{m,mag}$	Magnetophoretic velocity for magnetic nanoparticles	$\frac{F_{m,mag}}{3\pi\eta D_{p,mag}}$	**3 * 10^{-5} m/sec**

Table 2-2: Parameters for order of magnitude calculations and simulations

Parameter	Name	Value	Rationale or reference
μ_0	Permeability of free space	$4\pi \times 10^{-7}$ H/m	
M_f	Saturation Magnetization of fluid	3325 A/m for 5wt % fluid	[8-9]
M_0	Saturation magnetization of iron	1.75×10^6 A/m	
L_{char}, L_{obs}	Characteristic dimension of the system (L_{char}) and the obstacles (L_{obs})	0.1 mm	Estimates for a macroscale device, also assume $L_{char} = L_{obs}$
D_p	Diameter of particle	500 nm	Approximate value in the range of interest
η	Viscosity of fluid	0.001 Pa-s	Assume viscosity of water
V_0	Approach vel. of fluid	0.001 m/s	Arbitrary
ρ	Density of particle	1000 kg/m^3	Assume same as water
D_m	Diameter of magnetic nano-particle core	30 nm	[8]
M_p	Saturation Magnetization of magnetic nanoparticles	1.75×10^6	Same as M_o
H_0	Strength of applied uniform magnetic field	1×10^6 A/m	An approximate magnitude of field strength corresponding to 1 T induction
a	Diameter of circular obstacle	0.4 mm	First approximation $L_{obs} = a$ (for circular obstacle)

2.3.5 Particle trajectory model to simulate the behavior of non-magnetic particles around structured obstacle arrays

In order to develop a separation system, a fundamental understanding of the physics and behavior of non-magnetic particles in regions of structured magnetic field gradients such as those generated by iron obstacles is necessary. Particle trajectory simulations, described in this section can be performed to track particle motion and their size dependence around structured field gradients.

The particle trajectory model performs a simple force balance around a non-magnetic particle immersed in a magnetic fluid. The behavior of a non-magnetic particle is governed by the action of four major forces as shown in Figure 2.3 – the drag force due to fluid flow, the magnetic force, force of diffusion and gravity.

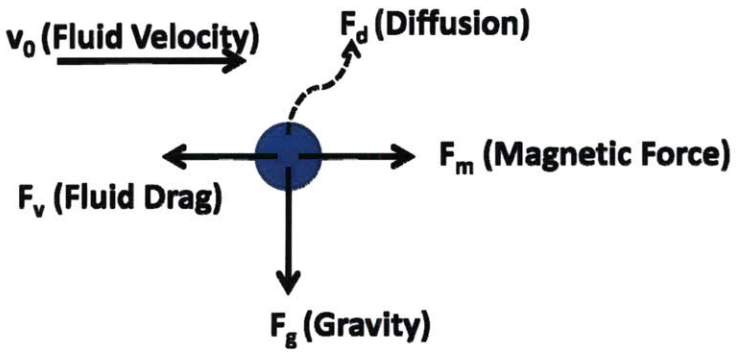

Figure 2-3: Major forces acting on a non-magnetic particle immersed in a magnetic fluid

The force balance on the particle taking into account these four forces can be written as,

$$m\frac{dv_p}{dt} = F_v + F_m + F_d + F_g \tag{2.37}$$

For the submicron particles under consideration, the time scale for particle acceleration (due to inertial force) is considered much smaller than the time scale under which the other forces operate [10]. It can be assumed that under steady state, the inertial forces are much smaller than other forces and can be ignored for Lagrangian particle trajectory modeling. Also, since the Reynolds number is much smaller than 1 (Table 2-1), creeping

flow regime is valid and Stokes' Law can be used to calculate the drag force [11]. The force balance now takes the form

$$6\pi\eta R_p(\underline{v}_0 - \underline{v}_p) - \mu_0 V_p M_f \underline{\nabla} H + F_d + (\rho_p - \rho)V_p \underline{g} = 0 \tag{2.38}$$

where, $\underline{v}_0$, $\underline{v}_p$ are the velocities of fluid and particle respectively, the second term denotes the magnetic buoyancy force, ρ_p and ρ denote the densities of particle and fluid respectively and $\underline{g}$ denotes the acceleration due to gravity. In the size range of interest, the diffusive forces and gravity are negligible compared to the other forces (Table 2-1). Neglecting these forces and rearranging, we get an expression for particle velocity as,

$$\underline{v}_p = \underline{v}_0 - \left(\frac{1}{6\pi\eta R_p}\right)\mu_0 V_p M_f \underline{\nabla} H \tag{2.39}$$

We can convert this equation into a dimensionless form by defining the following non-dimensional variables:

$$v' = \frac{v_0}{V_0};\ \nabla' = \frac{\nabla}{a};\ t' = \frac{ta}{V_0};\ H' = \frac{H}{H_0} \tag{2.40}$$

Here V_0 is the velocity scale for the system which is chosen as the approach velocity of the fluid, 'a' is the characteristic dimension for the system (which is related to obstacle size), and H_0 is the scale for applied magnetic field in the system. Using the variables defined in equation (2.40), the dimensionless particle velocity is obtained as,

$$\underline{v}_p' = \underline{v}' - \gamma\, \underline{\nabla}' H' \tag{2.41}$$

where γ is a dimensionless ratio defined as the Magnetophoretic Velocity Ratio given by

$$\gamma \equiv \frac{V_m}{V_0} = \frac{1}{V_0}\left(\frac{2\mu_0 H_0 R_p{}^2 M_f}{9\eta a}\right) \tag{2.42}$$

Since Equation 2.42 is dimensionless, V_m must be a velocity scale to match the denominator and is defined as the "magnetophoretic velocity". The magnetophoretic velocity ratio γ is a ratio of two velocity scales and it denotes the relative importance of

magnetophoretic velocity to superficial velocity. We can observe from equation (2.41), that velocity of the particle is a vector sum of fluid velocity and a magnetophoretic component denoted by $-\gamma\underline{\nabla}'H'$.

We observe that the larger the value of γ, the more the deviation in particle trajectory from the fluid streamline. If Equation 2.41 is properly scaled, $v' \sim O(1)$ and $\nabla' H' \sim O(1)$. For the effect of magnetic forces to be significant, γ must be close to O(1). It can be also seen from equation (2.42) that γ is proportional to R^2_p. This shows that γ increases rapidly with particle size, and the deviation in trajectory must be much larger for larger particle as compared to smaller particles. This is an important observation for separation system design. For designing a system to separate two particle sizes R_{p1} and R_{p2}, the other parameters in the system (mainly H_0, a, and M_f) must be chosen such that γ is close to 1 for the larger particle size while it is much smaller than 1 for the smaller particle size. This will allow significant effect of magnetophoretic forces on the larger particle size while the smaller particle size escapes with much lower interaction.

For tracking the trajectory of particle motion, equation (2.41) can be expressed in terms of position vector of the particle and integrated using explicit Euler method to obtain,

$$\frac{d\underline{r}'_p}{dt} = \underline{v}' - \gamma\,\underline{\nabla}' H' \tag{2.43}$$

$$\underline{r}'_{p,i+1} - \underline{r}'_{p,i} \approx \left(\underline{v}' - \gamma\,\underline{\nabla}' H'\right)_i \Delta t'_i \tag{2.44}$$

Equation (2.44) provides only a first order approximation of the trajectory of the particle. Given a velocity profile for the fluid (v') and a magnetic field profile (H') and an initial particle position ($\underline{r}_{p0}$), equation (2.44) can be used to obtain the trajectory of a non-magnetic particle in the region of magnetic buoyancy forces. The velocity profile and magnetic field profile can be calculated using COMSOL Multiphysics®. Maxwell's equations and Navier Stokes Equation are solved with appropriate boundary conditions to obtain the magnetic and flow field respectively.

For obtaining particle trajectories, the time step used for integration is scaled at each step i to have an approximately constant displacement at each time step as follows,

$$\Delta t_i' = \frac{\Delta t_0' V_0'}{\sqrt{\left(v_x' - \gamma \frac{\partial H'}{\partial x'}\right)_i^2 + \left(v_y' - \gamma \frac{\partial H'}{\partial y'}\right)_i^2}} \tag{2.45}$$

Using this time step, we can calculate particle trajectories for a variety of geometric arrangements of obstacles. If the time step $\Delta t_i'$ chosen is small enough, second order terms can be neglected in evaluating position vector $\underline{r}'_p$ of the particle without causing significant deviations from actual trajectories. This approximation is quite helpful in numerical solutions, since the v' and H' profiles are available through COMSOL and it is numerically challenging to determine second order terms for these field profiles.

In this section, we have established a basic framework for understanding particle behavior under different operating conditions (magnetic and flow field profiles) which will help in the design of a separation system. In the next section, the results of particle trajectory simulations around a single obstacle are presented.

2.4 Particle trajectory simulations (2D) for a single obstacle

It is important to understand the behavior of a nonmagnetic particle near a single magnetizable obstacle (i.e. a certain magnetic field gradient) before a separation technique utilizing a number of obstacles can be proposed. Based on the behavior of particles near an obstacle of a specific shape and size, effects of placing multiple obstacles in an array can be determined. Particle trajectory simulations were performed using the model developed earlier. A detailed description of simulation methodology for a single obstacle in two dimensions is presented below.

2.4.1 Magnetic field distribution around an obstacle

The obstacle geometry is drawn in COMSOL® and internal boundaries (iron obstacle) and external domain boundaries are specified. The material properties are used as contained in the software database for iron obstacles and air. A finite element mesh is generated over the domain, and it is ensured that the mesh is fine enough such that the calculated field profile does not show apparent discontinuities. It is important to choose an appropriate fineness of generated mesh for each situation, since too fine a mesh size can cause computational difficulties while too broad a mesh size can lead to insufficient field information to generate a gradient. The magnetic field profile is generated by solving Maxwell's equations as discussed in section 2.2 using finite element (FEM) method. For the boundary conditions, a uniform vertical field (+y direction) of magnitude H_0 (= 10^6A/m) is imposed on the domain. The simulation parameters were used as shown in Table 2-2 earlier. The magnetic field generated for a circular and a triangular obstacle are shown in Figure 2-4a and 2-4b respectively.

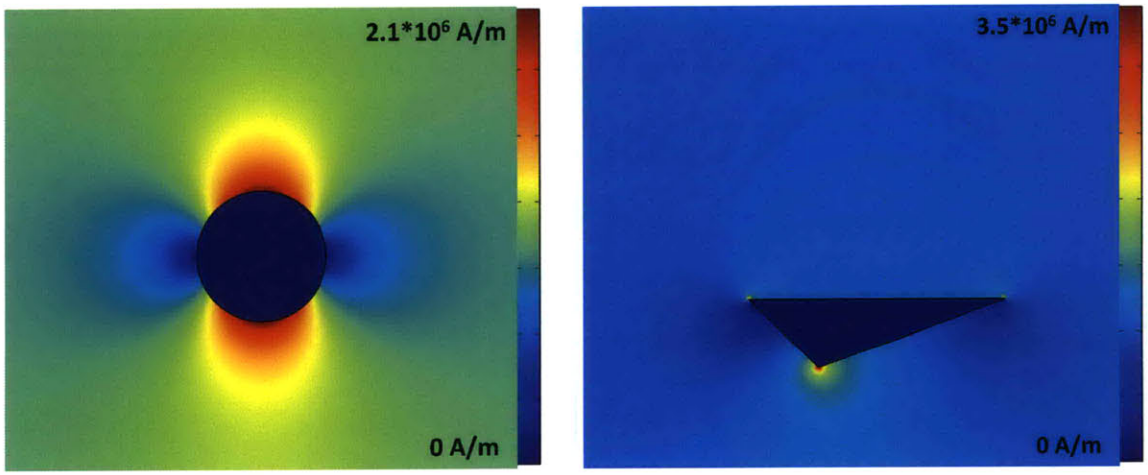

(a) (b)

Figure 2-4 Magnetic Field distribution for an magnetic field is applied in +y direction for a) Circular obstacle b) Triangular obstacle.

The magnetic field profiles show regions of strong magnetic field gradients in the immediate vicinity of the obstacle. We can also observe that the magnetic field goes to zero inside the iron obstacle for both cases. On comparing the two field distributions, we

can observe that for a circular obstacle, the gradients are spread across the entire surface due the symmetry of the obstacle shape, while for a triangular obstacle, the magnetic field variation is concentrated around the vertices. Also, in the triangular obstacle case, we obtain much sharper gradients than the circular case though these gradients are spread over a limited region.

2.4.2 Flow field distribution around an obstacle

As shown in Table 2-2, the Reynolds number for this system is much smaller than 1, and hence creeping flow approximation holds. To obtain the velocity field for various geometries, Navier Stokes equation can be solved coupled with appropriate boundary conditions. Again, COMSOL® Multiphysics was used to solve for this velocity field. The 2-D obstacle geometry was drawn in COMSOL with a uniform flow approaching from the bottom boundary in the +y direction. The top boundary was assumed to have a dynamic pressure of zero and the side boundaries were specified with open boundaries. This effectively sets the dynamic pressure to zero at the side boundaries. No slip conditions were assumed at the obstacle surface. Results plotted for the magnitude of velocity are shown for both a circular and triangular obstacle in Figure 2-5 below.

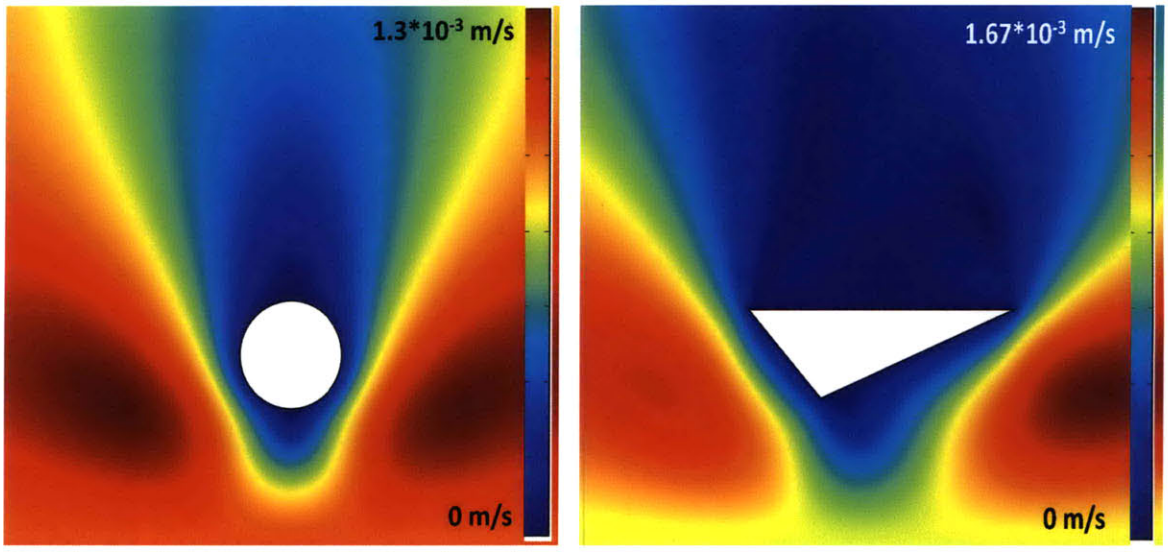

(a) **(b)**

Figure 2-5: Flow Field distribution when a uniform flow approaches the object in +y direction for a) Circular obstacle b) Triangular obstacle.

2.4.3 Methodology for particle trajectory determination through Euler integration

Particle trajectories around a circular or triangular obstacle can be evaluated using equation (2.44). For this purpose, the parameters specified to determine γ are the magnetic fluid strength (M_f), obstacle diameter (a), viscosity of magnetic fluid (η), the applied magnetic field (H_0) and inlet flow velocity (V_0). The values of these specifications are shown in Table 2-2. The particle radius was varied to determine the effect of particle size on trajectories generated. The values of flow field and magnetic field at each point were evaluated by 2D interpolation of data from COMSOL®. The magnetic field data was converted to gradient of the field through processing in MATLAB®. Particles were then introduced at various positions at the bottom boundary (with the flow in +y direction) and their trajectories obtained using Euler integration of Eqn. (2.44). The trajectory of a particle was terminated when it reached either an external boundary (outlet) or an internal boundary (obstacle surface). Thus, an important assumption in these simulations is that if a non-magnetic particle hits the obstacle surface, it gets captured permanently. This is a reasonable assumption, since the particles under consideration are small enough and inertial effects can be ignored. In some experimental systems, this effect could translate to retardation instead of capture. Particles subjected to significant magnetic forces because of presence of obstacles could get retarded to a larger extent than particles not subjected to those forces. However, for this section, we will continue to refer to this phenomenon as capture.

2.4.4 Results from particle trajectory simulations

The initial results from particle tracking simulations are presented below. The particles start from various positions at the bottom boundary. In Fig. 2-6a, we see that in the absence of field, the trajectories very closely follow fluid stream-lines; in fact, on verification, they were found to exactly coincide with the fluid streamlines which is expected from equation (2-44). Figures 2-6(b-d) represent the case when the field has been turned on. For smaller particles ($D_p \sim$ 100nm, Fig 2-6b), the particle motion still

resembled fluid motion very closely. As particle size increases, larger and larger deviation from fluid motion is observed. For 500 nm particles (Fig 2-6c), in the initial part of trajectory the particle feels repulsion due to the presence of the obstacle but on moving further down, it is attracted towards the obstacle. This behavior, which occurs due to the change in field gradient direction, results in particles very close to the obstacle being captured. However, the majority of the particles still pass unaffected. As the particle size increases further (D_p = 800 nm, Fig 2-6d), attractive forces become even stronger resulting in the capture of a majority of the particles. Thus, we observe a preferential capture of larger particles, due a higher γ and this fact can form the basic principle for the separation system.

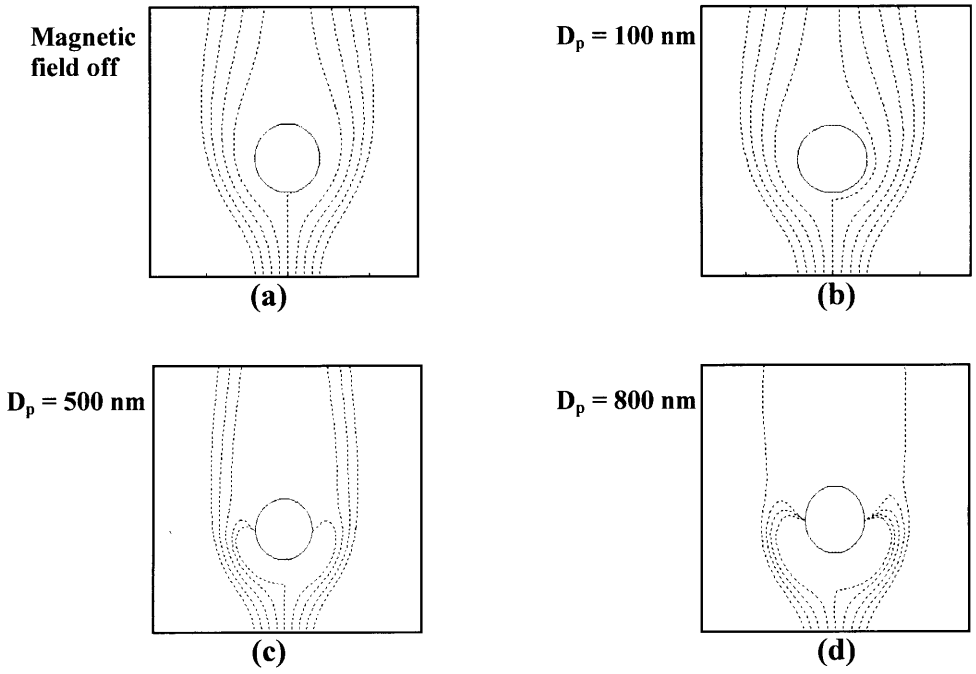

Figure 2-6: As particle size increases, more and more particles are captured on obstacle. Trajectories of particles are shown for (a) In the absence of field (b) In the presence of field for 100 nm diameter particles (c) 500 nm diameter (d) 800 nm diameter particles

In the previous results, the magnetic field was oriented parallel to the flow direction in the +y direction. The effect of rotating the field by 90^0 was also studied, the results of

which are presented in Fig. 2-7. We observe that for the same range of initial x-values for particle trajectory, there is improved capture of 800 nm particles in Fig. 2-7b as compared to Fig 2-6d.

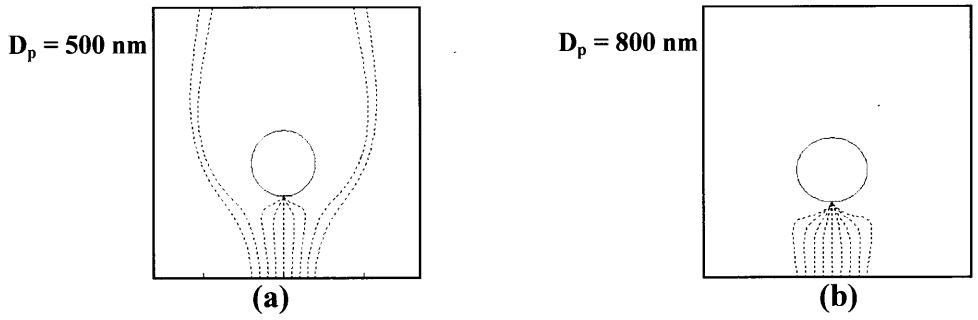

Figure 2-7: Behavior of particles when field direction is rotated by 900 while the flow direction remains the same. Trajectories are shown for (a) 500 nm (b) 800 nm particles

However, a substantial number of 500 nm particles also get captured as a result of which resolution of the device suffers in this case. So, it can be seen that resolution depends on magnetic field direction and it is possible to optimize resolution by varying field direction. The obstacle shape was also changed from circular to an asymmetric triangular obstacle of same area to see the effect on separation. The particle trajectories for a triangular obstacle are shown in Fig. 2-8.

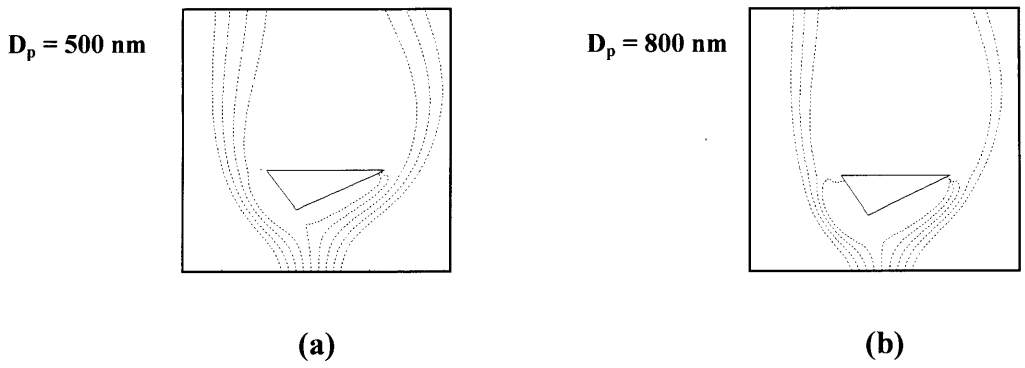

Figure 2-8: Particle trajectories for a triangular obstacle for (a) 500 nm particles (b) 800 nm particle

From Fig. 2-8, we see that separation is not as efficient for a triangular obstacle as for a circular obstacle. For this case, particles of both sizes behave similar to a circular obstacle case though 800 nm particles are captured more effectively than are 500 nm particles. From these results, we can see that the shape of obstacles is very important in designing a separation system. The systematic variation of size, shape and geometric arrangement of obstacles is the topic of a later section.

2.5 Initial ideas for a novel separation system

2.5.1 Proposed separation concept

It was seen from the results of particle trajectory simulations around a single obstacle that given specific system parameters (of field, obstacle dimensions etc.), the balance between fluid drag and magnetic forces governed the behavior of the particles. The fundamental nature of forces is such, that larger particles experience higher magnetophoretic forces as compared to smaller particles. The resulting deviation in trajectory allows a preferential capture of larger particles. On the basis of this principle, an initial conceptual design of a separation system was designed and is presented in Fig. 2-9.

The proposed separation system could work as follows - when a mixture of small and large particles is introduced into the system, only the larger particles would be preferentially trapped on the surface of the obstacles. The smaller particles flow out of the device along the streamlines. Once small particles are removed from the mixture, the trapped larger particles could be eluted by switching off the magnetic field or rotating the magnitude field direction by 90^0. Thus, by cycling between the on and off states of magnetic field, the separation system could be operated in a semi-continuous fashion. This system is in essence a magnetophoretic chromatography system which preferentially retards or captures larger nonmagnetic particles while allowing smaller particles to elute faster.

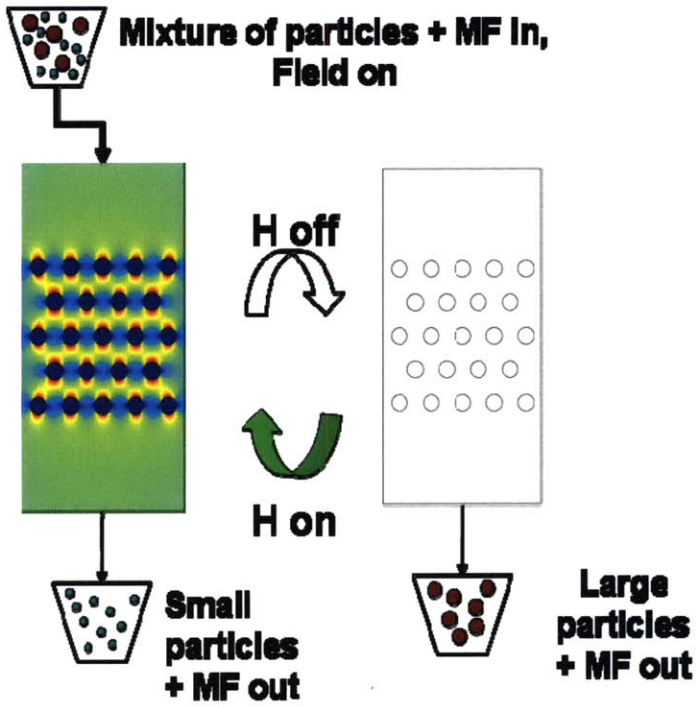

Figure 2-9: Schematic of initial device design

2.5.2 Approach towards separation system design

There is no previous literature available on capture of non-magnetic particles on iron obstacles. However, HGMS systems to capture magnetic nanoparticles are well known in literature [12-13] which operate on the principle of capture of magnetic nanoparticles on a wire mesh, the only difference being that here, the wire mesh is usually arranged randomly. However, for the design of the separation system in this thesis, two aspects of design need to be considered – geometry of obstacle course and operating conditions for the system.

2.5.2.1 Geometric design of obstacle course

The key to design of an efficient separation system for non-magnetic particles would be the optimal geometric placement of the obstacle array in the separation device. This requirement arises from the fact that the non-magnetic particles are captured through magnetic buoyancy force which is an *indirect* force and arises due to the presence of a magnetic environment (such as a magnetic fluid) around a non-magnetic particle. A

random mesh would not ensure the provision of such an environment. Thus, it is required to have the non-magnetic particle mixture navigate a well designed obstacle course to ensure that the magnetic buoyancy forces capture larger particles while smaller particle pass through.

The important variables for optimizing the geometric design of the separation system include the shape of the obstacles, the geometric pattern of arrangement (e.g. rhombic, square etc.), the characteristic dimension of obstacles (e.g. radius) and the characteristic dimensions for the geometry (e.g. spacing, width) that define such patterns. A systematic variation of the various geometries and spacing combinations can be carried out and particle trajectories generated for transport of non-magnetic particles through the system. An optimal configuration could be determined from the results of these simulations.

2.5.2.2 Design of operating conditions

Once an obstacle array has been designed, the operating conditions for the system would have to be chosen to optimize separation resolution. The important variables to be optimized include the applied magnetic field (H_0), the inlet flow velocity (V_0), the fluid magnetization (M_f) and the magnetic field direction. All these variables are interrelated through the magnetophoretic velocity ratio γ as shown in equation (2.42). Thus, systematically varying γ would allow determination of various sets of optimal operating conditions. This is the topic of the next section.

2.6 Particle trajectory simulations for multiple obstacles

In this section, we will present the results from particle trajectory simulations for systems containing an array of obstacles in various geometries. Simulations were carried out by integrating the capabilities of COMSOL (to generate magnetic and flow field profiles for any given geometry) and MATLAB (to perform trajectory integration using equation (2.44)). The simulation architecture is presented in Figure 2-10. The information on geometry of obstacle array and operating variables are input into MATLAB. The geometry of obstacle array was varied to study three types of arrangements – linear array, square array and rhombic array. Within each arrangement, the characteristic spacing was also varied. Systematic variation of operating variables (applied magnetic field and flow velocity) was carried out through variation of γ. MATLAB was then made to interface with COMSOL to obtain the magnetic field and flow field distribution for the given situation. The obtained data was converted into a dimensionless form, gradients were calculated and finally, particle trajectories were determined using equation (2.44).

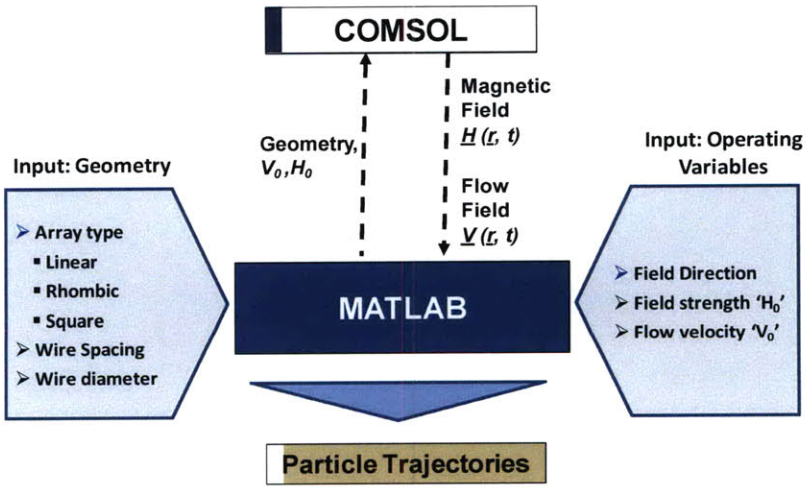

Figure 2-10: System architecture for integration of MATLAB and COMSOL for obtaining particle trajectories while systematically varying geometric and operating variables

The section below first presents particle trajectories for a linear array, followed by square array and finally, a rhombic array of obstacles.

2.6.1 Simulations for a linear array of obstacles

2.6.1.1 Particle trajectories

A linear array of obstacles is just a simple extension of single obstacle case, with obstacles present at a periodic interval in the +x direction. For the purpose of this simulation, an infinite number of periodically spaced obstacles were assumed. Figure 2-11a and Figure 2-11b show the flow field and magnetic field for a linear arrangement of obstacles for a spacing of 2D (twice the diameter measured center to center). The applied magnetic field and the fluid flow are both in the +y direction. We can observe from the profiles that for the flow field, the fluid approaches the obstacles at a uniform velocity but gets accelerated when passing through the array – the magnitude of velocity is maximum in +y direction between the obstacles. However, based on the direction of the applied magnetic field (+y), the regions of magnetic field minima where non-magnetic particle capture occurs is also located between the obstacles. From these field profiles, we expect the ratio of magnetic buoyancy force to drag force (the local γ value) to be quite low between the obstacles and hence the capture to be quite inefficient.

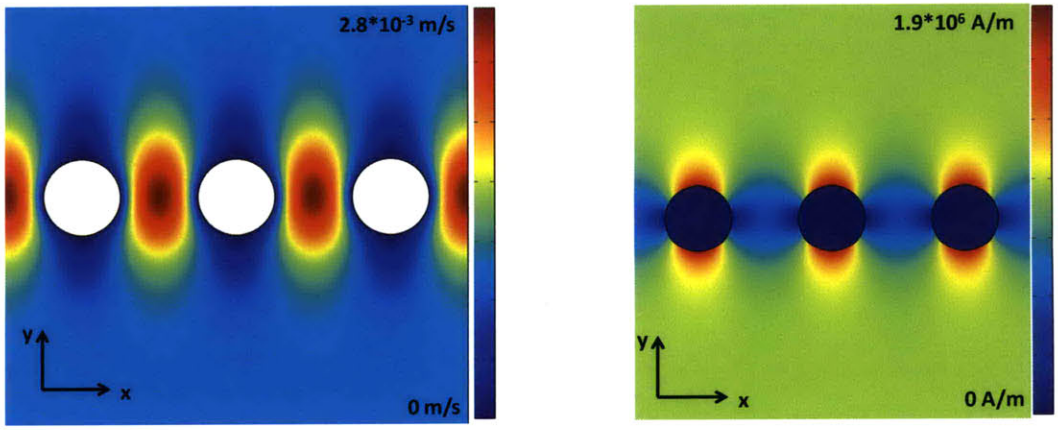

(a) (b)

Figure 2-11: Field distributions for a linear array of obstacles with infinite obstacles stretching in the +x direction - a) Flow field for an approach velocity of 0.0005 m/s in +y direction b) Magnetic field with an applied field of 10^6 A/m in +y direction

The results from particle trajectory simulations for the linear array above are presented in Figure 2.12a-d.

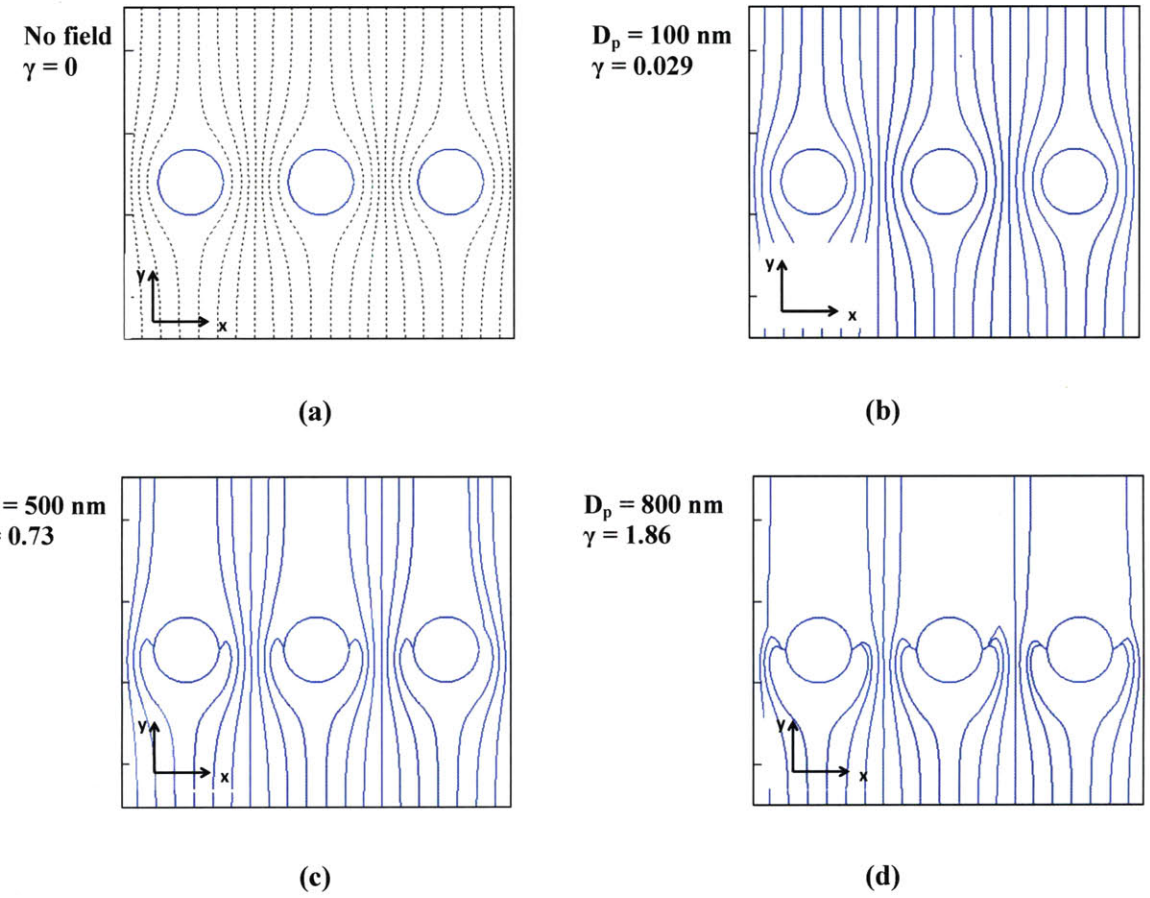

Figure 2-12: Trajectories of particles are shown for fluid flowing in +y direction at 0.0002 m/s and uniform applied field of 10^6 in + y direction and (a) In the absence of field (b) In the presence of field for 100 nm diameter particles (c) 500 nm diameter (d) 800 nm diameter particles

Figure 2-12 shows four different cases for the simulation – starting from the no field case in (a) to significant capture in (d). When no field is applied, the particles follow fluid streamlines which are symmetric across the obstacles due to the periodicity of the obstacle array. When the particles are small with D_p = 100 nm, (γ = 0.029) they closely follow fluid streamlines as well. For 500 nm particles, γ increases sharply at 0.73, and we start observing signs of capture. For the largest particle size of 800 nm, γ = 1.86 and significant amount of capture is observed. Thus, the results from particle trajectory

simulation can be used to distinguish between behaviors of particles of different sizes and evaluate the geometries. Similar trajectories were generated for various obstacle spacings and operating conditions.

2.6.1.2 Plots of capture efficiency (θ) vs. magnetophoretic velocity ratio (γ)

In order to understand the systematically evaluate the effectiveness of the various geometric arrangements in particle capture and separation, plots of capture efficiency (denoted by θ) vs. magnetophoretic velocity ratio γ were generated. Capture efficiency θ can be defined as

$$\theta = \frac{\#\text{ of particles captured on wires}}{\#\text{ of particles sent into the system}} \quad (2.46)$$

Based on this definition, the results for a linear array of obstacles are shown in Figure 2-13. Initially, when no magnetic field is present (γ=0) for any obstacle spacing. We can observe that the capture efficiency θ rises sharply with γ and ultimately reaches saturation at 100% which denotes complete capture of the particles. The particle trajectory model assumes an infinite capacity of obstacles. Thus, when γ is large enough, 100% capture is always observed. When obstacles are closely spaced together (spacing = 1.25D), the minimum value of γ required for 100% capture, γ_{min} = 1.9. As obstacle spacing increases, γ_{min} increases steadily. Hence, these curves show us that it is easiest to capture particles when obstacles are closely spaced together. In fact, a rough thumb rule can be deciphered from the plot – θ is (approximately) inversely proportional to obstacle spacing for a given value of γ. However, practical considerations indicate a tradeoff of obstacle spacing with pressure drop. As obstacle spacing decreases, pressure drop across the obstacle array increases sharply which could set limits on the smallest allowable spacing of obstacles. In addition, limits on the ability to machine obstacles closely could also affect the practically achievable obstacles spacing.

Similar analyses as shown here can be carried out for various obstacle geometries. The next section discusses results for particle trajectory simulations and capture efficiencies for a square array.

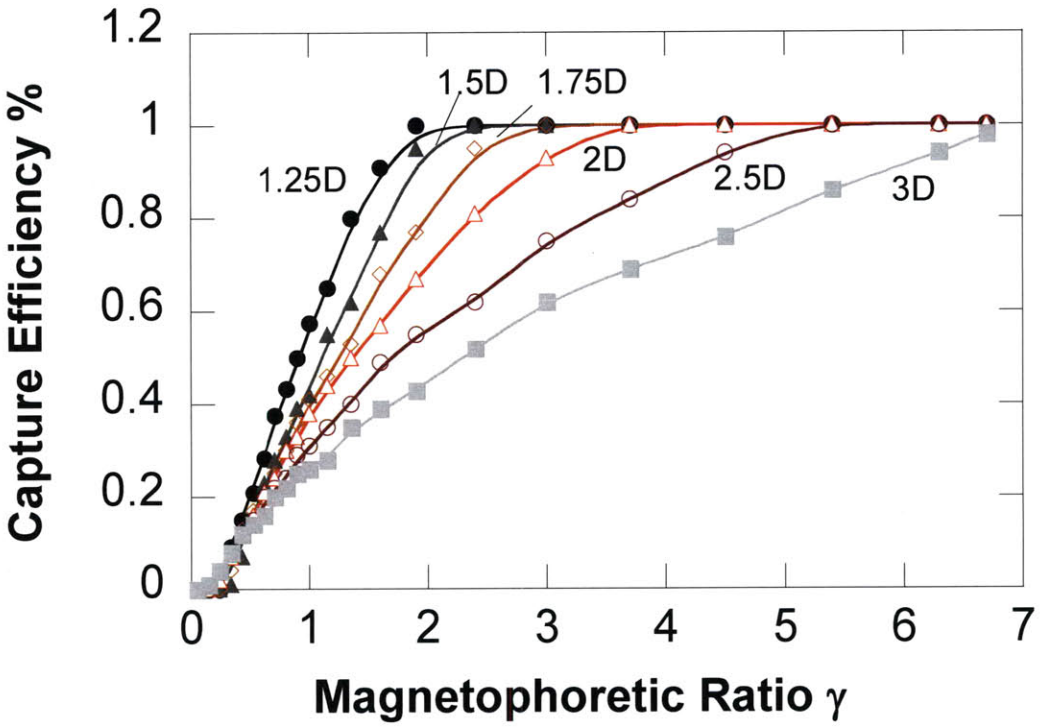

Figure 2-13: Plot of capture efficiency θ vs. magnetophoretic velocity ratio γ for a linear array of obstacles and various values of obstacle spacing.

2.6.2 Simulations for a square array of obstacles

A square array of obstacles was constructed as a simple extension of a linear array in the y direction with equal obstacle spacing in x and y directions. The flow field and magnetic field for a square array are shown in figure 2-14a and 2-14b. From the velocity profile, we observe, the fluid enters with a uniform profile at 0.0005m/s and flows quicker in the regions directly between the circular obstacles. On comparing the magnetic field profile, we again observe the regions of capture (magnetic field minima) to be in +x plane directly between the obstacles.

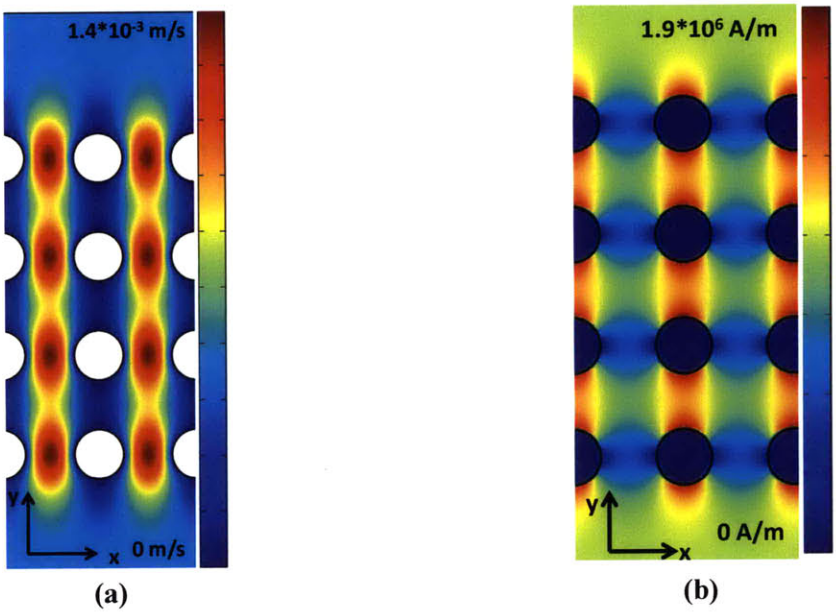

Figure 2-14: a) Flow field distribution with applied flow of 0.0005m/s in +y direction b) Magnetic field distribution with applied field of 10^6 A/m in +y direction.

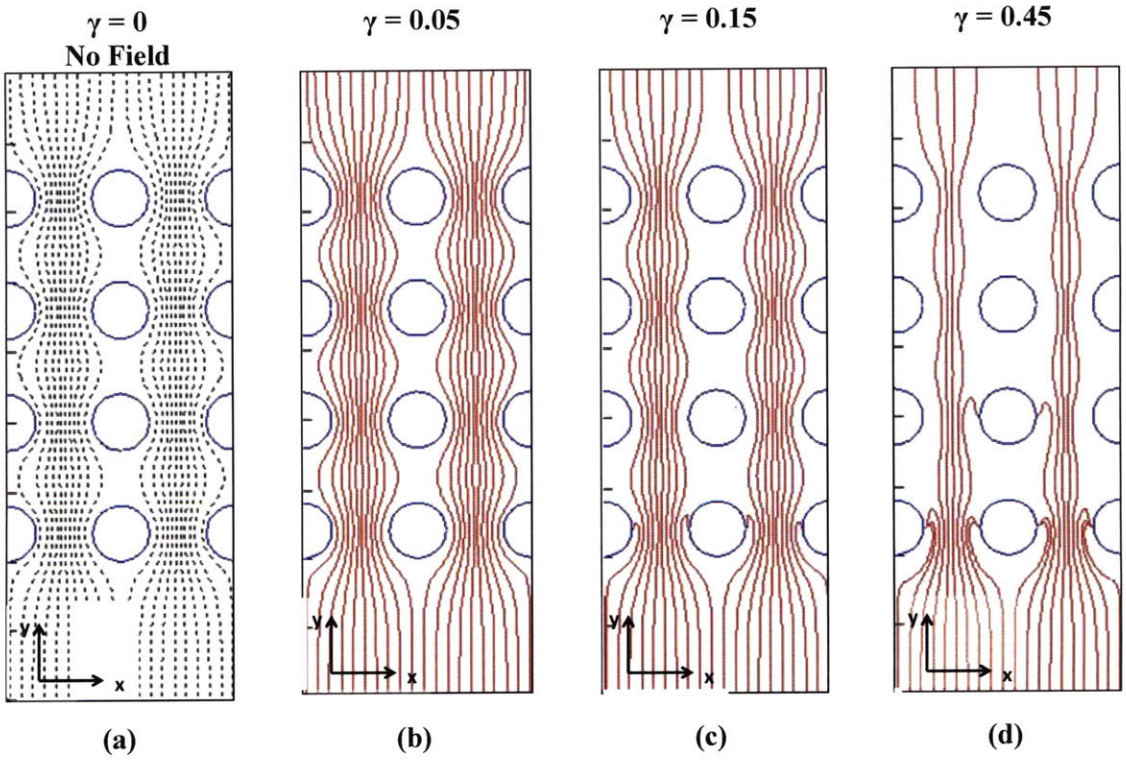

Figure 2-15: Particle trajectories for a square array of obstacles, 2-D spacing with, a)no field and with magnetic field on with, b) γ=0.05 c) γ=0.15 d) γ=0.45

Particle trajectory simulations were carried out for different values of γ and are shown in Figure 2-15(a-d). As mentioned earlier, the particle trajectories are same for a given value

of γ, irrespective of the particle size, flow velocity and magnetic field value. We can observe from the particle trajectories that as with the earlier cases, capture of particles occurs in the x-plane on the obstacles. Most of the capture occurs on the first layer of obstacles with a few particles getting captured on second and third layers. Capture with a square array is more efficient as compared to a linear array, which is expected due to increase in the number of obstacles. On comparing the particle trajectories for a square array with results for a linear array in Figure 2-13, we observe a much lower value of minimum γ required for complete capture (γ_{min}) for a square array. This fact can be observed in plot of capture efficiency θ vs. γ for various geometries shown in Figure 2-16. This figure shows that a square array can perform separations with a much lower value of magnetic field H_0 or a higher velocity V_0 (leading to a higher throughput). Hence a square array is more efficient for separation purposes as compared to a linear array.

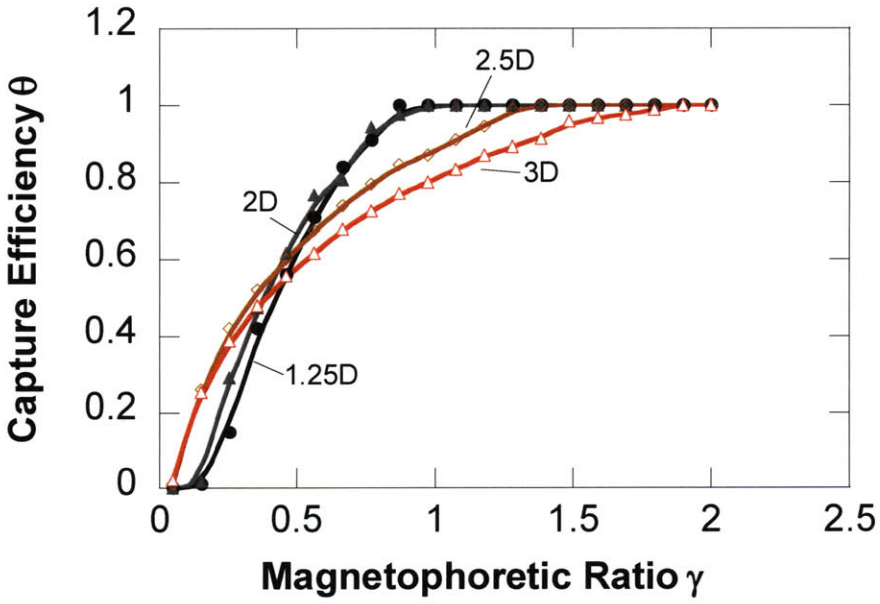

Figure 2-16: Plot of capture efficiency θ vs magnetophoretic velocity ratio γ for a square array

From the figure, the trend for θ vs. γ is similar to that for the linear obstacle array case. θ increases sharply with γ for any geometric spacing. Also, as the spacing becomes wider apart, capture is more efficient for a smaller spacing (in the region of large γ). However, an interesting trend is observed for small γ where a wider spacing is more efficient for

capture. The reason for this could be understood by investigating local magnetophoretic ratio γ_{local} defined on the basis of local velocity V_{local} as compared to a global γ defined on the basis of superficial velocity V_0. γ_{local} is a better determinant of particle behavior as compared to γ since the velocity scale is more appropriate in the former case. In the case of a square array with closely spaced wires, both V_{local} and H_{local} differ greatly from V_0 and H_0 respectively. Further investigation of the relationship between γ_{local} and capture behavior could help explain some of the anomalies in Figure 2-16.

2.6.3 Simulations for a rhombic array of obstacles

A rhombic array of obstacles was constructed for performing trajectory simulations. The characteristic dimensions defining this array were the spacing between the obstacles, the rhombic geometry tilted at a 45^0 angle from the x-axis and an angle of 90^0 between the sides of the rhombus. The flow and magnetic fields for a rhombic array are shown in Figure 2-17 (a-b). Due to the direction of magnetic field in the +y direction, the regions of field minima corresponding to capture zones lie on the x-plane of the obstacles. The velocity profile also looks more amenable to capture, since there are no obvious zones of fluid channeling as was observed in the case of a square array. The particle trajectories are shown in Figure 2-18 (a-d). For the case of no field, particles travel through the obstacle course in the +y direction, and to the outlet. When a small field is applied compared to flow velocity ($\gamma = 0.05$), all particles still reach the outlet since the capture force is not strong enough as compared to fluid drag. Some deviation from pure fluid trajectory is visible and the trajectories to get denser around the obstacle array, probably due to the magnetic buoyancy push experienced from certain regions of the obstacle. As the γ increases further (γ=0.15), small amount of capture is visible in the initial rows of obstacles. For an even larger value of γ (=0.45), much more significant capture is observed. Finally, as γ reaches a large enough value, complete capture of particles is observed (not shown in the figure). To compare the capture efficiency of a rhombic array with a square array and to determine the optimal rhombic geometry, plots of θ vs. γ were generated for various geometric spacings and are shown in Figure 2-19.

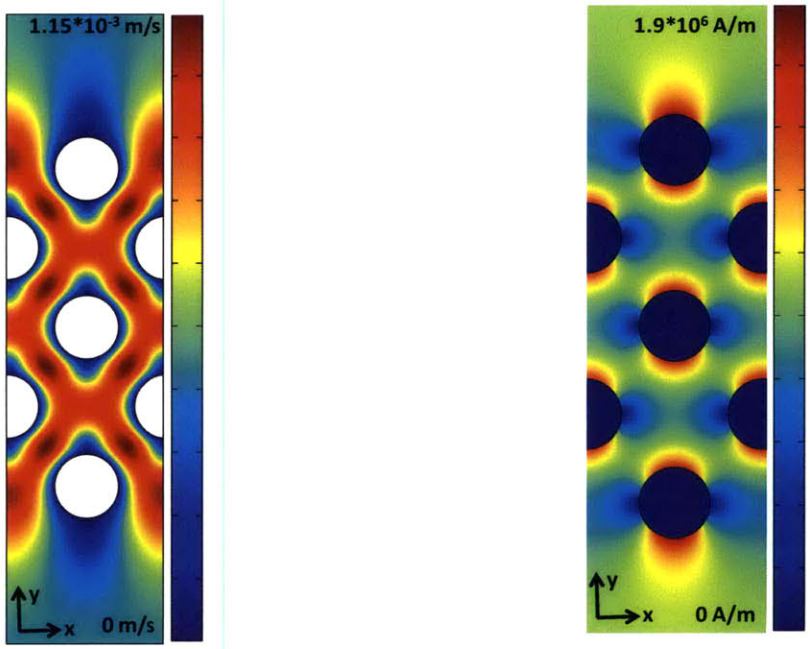

Figure 2-17 Rhombic Array: a) Flow field distribution with applied flow of 0.0005m/s in +y direction b) Magnetic field distribution with applied field of 10^6 A/m in +y direction.

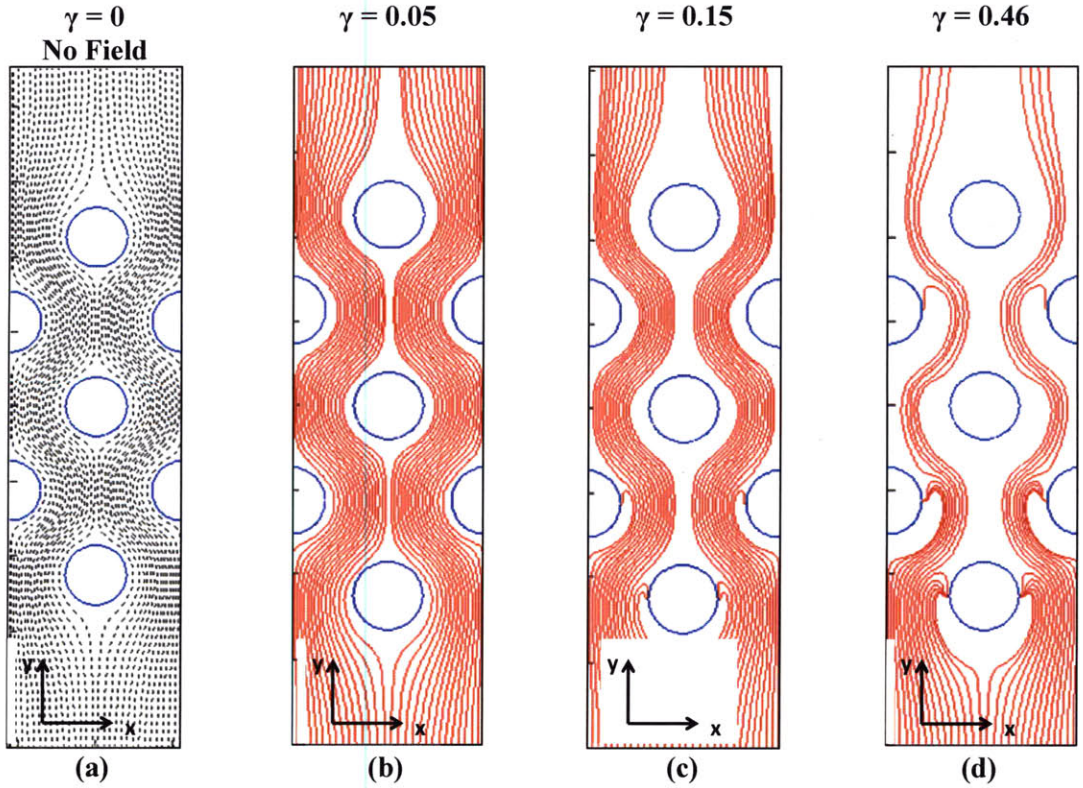

Figure 2-18: Particle trajectories for a rhombic array of obstacles, 2-D spacing, mag. field in +y direction, and, a) no field and, with magnetic field on b) γ=0.05 c) γ=0.15 d) γ=0.45

Again, a similar trend to previous graphs is observed – capture increases sharply with γ, and lower spacing results in better capture efficiency for the same γ. On comparing the capture efficiency for a rhombic array with a square array, we observe better capture for the case of a rhombic array. For a spacing of 2D, the γ_{min} required for complete capture is only 0.77, whereas, for a square array, we observed the corresponding γ_{min} = 1.18. A rhombic array is therefore more efficient than a square array for particle capture.

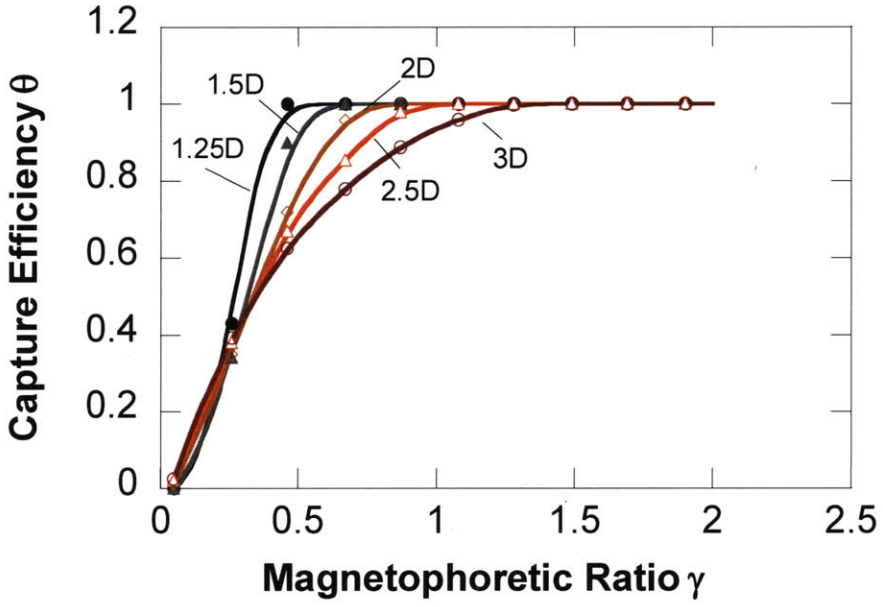

Figure 2-19: Plot of capture efficiency θ vs magnetophoretic velocity ratio γ for a rhombic array with magnetic field in +y direction

2.6.4 Simulations for a rhombic array - perpendicular magnetic field

We determined that a rhombic array gave the best capture efficiency among the various geometries explored. The previous set of simulations was performed with a magnetic field oriented at +y direction. We can refer to this configuration as the 'parallel' configuration since the applied magnetic field is parallel to the flow. The effect of changing magnetic field direction was also studied. This section describes results from simulations carried out with an applied magnetic field in the +x direction. This can be called the 'perpendicular' configuration. Figure 2-20a shows the magnetic field distribution for this scenario. It can be seen that the field minima is now in the y-plane

and hence, the capture zones are located in the front and back of the obstacles instead of the side of the obstacles. Figures 2-20b-d show the particle trajectories for this field direction, which confirms occurence of capture in y plane, in regions corresponding to magnetic field minima.

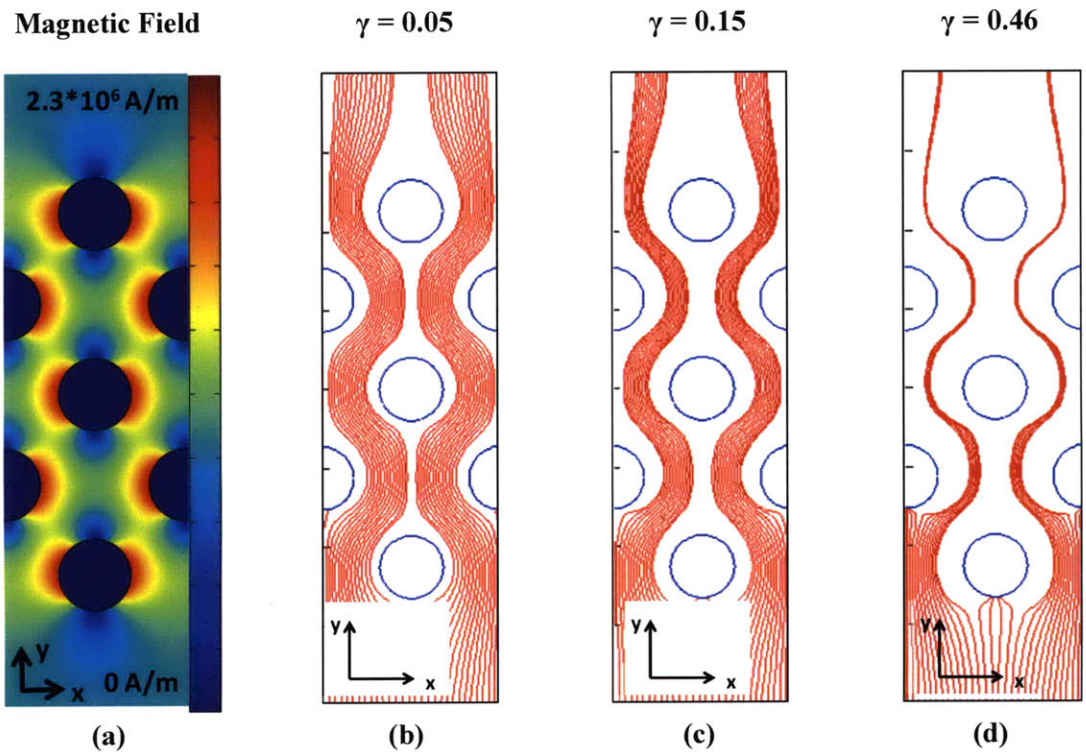

Figure 2-20: Results from simulations for a rhombic array with magnetic field in +x direction: a) magnetic field distribution b) γ = 0.05 c) γ = 0.15 d) γ = 0.46

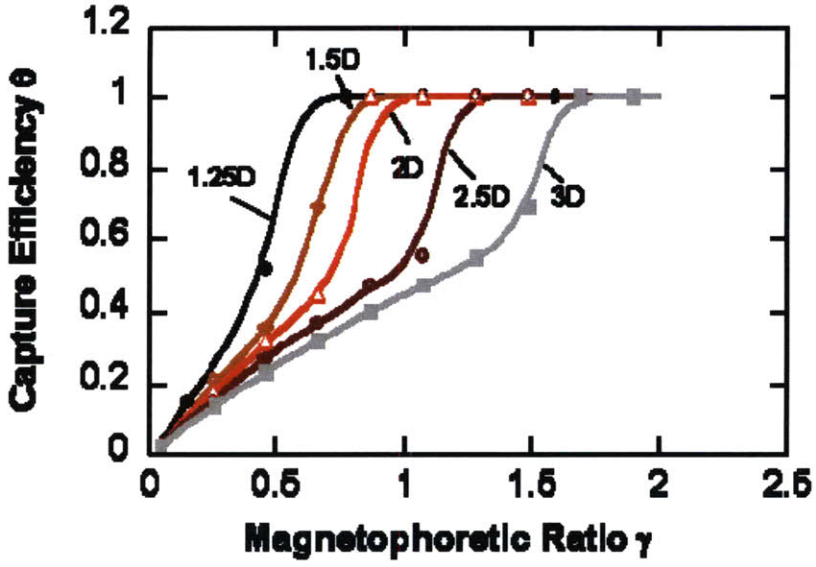

Figure 2-21: Plot of capture efficiency θ vs. magnetophoretic velocity ratio γ for a rhombic array with magnetic field in +x direction

As γ increases, the capture continues to increase as expected. The plot of θ vs γ is shown in Figure 2-21. Figure 2-21 shows interesting results when compared to previous plots of θ vs γ. θ still increases sharply with γ, and saturates at 100% as expected. Also, for the same value of γ, the capture efficiency is higher for obstacles spaced closer together. However, the shape of the curve is interesting. In all the curves, there is a sharp jump to 100% capture efficiency. Thus, at some point for all values of spacing, a small increase in γ results in a jump to 100% capture. This behavior is not observed when the field is in a parallel configuration. Since we are interested in preferential capture of larger sized particles, having a sharp jump, as in the perpendicular configuration is favorable. A system could be designed in such a way that the larger particle sizes has a γ value which allows complete capture (located just right of the sharp rise in the curve) while the smaller particle size which has a lower γ will have a much lower capture efficiency. Separation between mixtures of particles closely spaced together could be carried out using a perpendicular configuration

On comparing the capture efficiency in a rhombic array for a parallel vs perpendicular configuration, we observe that the perpendicular configuration is more efficient. For a 2D spacing, complete occurs at $\gamma_{min} = 0.87$ for perpendicular configuration, where as it

occurs at γ_{min} = 0.77 for a parallel configuration. Thus, this establishes that a rhombic array with a parallel configuration allows the most efficient capture of non-magnetic particles.

2.7 Summary and implications for separation system design

2.7.1 Conclusions

In this section, the results from particle trajectory simulations were demonstrated, first for a single obstacle and then for a multiple obstacle array.

For a single circular or triangular obstacle, it was observed that larger particles were preferentially attracted towards the obstacle and captured. For the specific simulations, at a flow velocity of 0.001 m/s, more 800 nm particles as compared to 500 nm particles. If the field was parallel to the flow, (parallel configuration) the capture occurred in the +x plane. If the field was in the perpendicular configuration, capture occurred in the +y plane. It was observed that circular obstacles have a better distribution of field gradient around the obstacles and hence lead to more efficient capture.

Trajectory simulations were carried out for an array of circular obstacles through systematic variation of geometry and operating conditions. This exercise provided a better understanding of the physics of particle behavior around an obstacle array and ultimately helped us distinguish between behaviors of particles of different sizes flowing through various geometric arrangements of obstacles.

Various geometries were used for simulation – a linear array, a square array and a rhombic array. The geometric spacing between obstacles was also varied. Simulations under a parallel field showed preferential capture of larger particles under each configuration. Plots of capture efficiency vs magnetophoretic velocity ratio γ were generated to compare the effectiveness of capture. In these plots, capture efficiency θ increased sharply with γ followed by saturation at 100% capture. Capture was usually more efficient at smaller spacing as compared to a larger spacing. On comparing

effectiveness of capture for various geometries, it was observed that rhombic geometry provides the optimal capture. Comparison of minimum γ for 100% capture for a spacing of 2D (twice the diameter of obstacles, measured center to center) is provided in Table 2-3. On comparing various configurations, it was determined that a rhombic array of obstacles with a parallel magnetic field configuration provided the most efficient capture of non-magnetic particles.

Table 2-3: Comparison of minimum γ required for complete capture of non-magnetic particles for various obstacle configurations at 2D spacing

Parallel configuration of magnet			Perpendicular configuration
Linear Array	Square Array	Rhombic Array	Rhombic Array
$\gamma_{min} = 1.9$	$\gamma_{min} = 1.18$	$\gamma_{min} = 0.77$	$\gamma_{min} = 0.87$

To understand the effect of magnetic field direction on capture location and amount of capture, two magnetic field directions were simulated – field parallel to the flow and perpendicular to the flow. It was observed that on rotating the magnetic field by 90^0, the simulated capture zones also rotated by 90^0. Also, it was observed that the plots of θ vs γ were sharper for a perpendicular configuration, thus allowing for sharper separation resolution.

2.7.2 Implications for separation system design

Using the information provided by the θ vs γ curves, we can easily design a separation system to separate two particle sizes. In order to explain the design process, let us take the example separation of a mixture of 500 nm and 800 nm particles. A rhombic array with a perpendicular magnetic field configuration with a 2D spacing can be chosen for this system. This geometry provides the most efficient capture, while maintaining a reasonable spacing between obstacles. To determine the operating conditions for performing the separation, we can look at the θ vs γ curve for the specific geometry and spacing, shown in Figure 2-22.

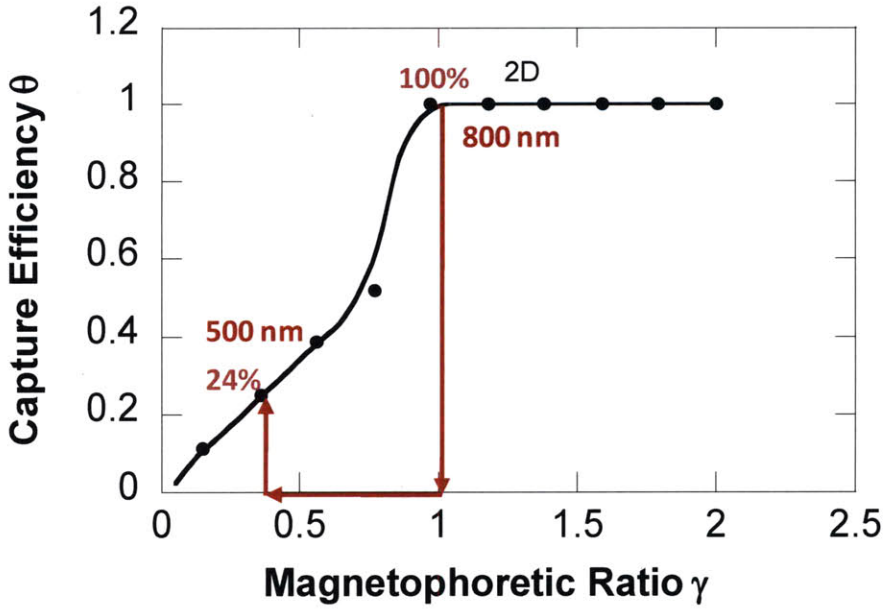

Figure 2-22: Design of operating variables for separation system using θ vs γ curve

Table 2-4: Operating variables for separating mixture of 800 nm and 500 nm particles in a rhombic array of obstacles and 'perpendicular' field configuration.

Variables	Symbol	Units	Value for 800 nm	Value for 500 nm
Particle size	D_p	Nm	800	500
Approach Velocity	V_0	m/s	0.0005	0.0005
Fluid magnetization	M_f	A/m	3365	3365
Obstacle radius	a	μm	80	80
Fluid viscosity	η	Pa.s	0.001	0.001
Magnetic Field	H_0	A/m	$2.69*10^5$	$2.69*10^5$
Applied induction	B_0	Tesla	0.34	0.34
Magnetophoretic ratio	γ		1.0	0.39
Capture efficiency	Θ	%	100%	24%

To determine the operating conditions, let us assume we want complete capture of 800 nm particles. From Figure 2-22, we determine that γ_{min} for this purpose = 0.87. As a conservative estimate, we can choose γ = 1.0 for complete capture. For this value of γ

and a particle size of 800 nm, assuming other physically realizable parameters in Table 2-4, we obtain the value of applied magnetic field induction B_0 = 0.34T. Based on this value of applied field, for a particle size of 500 nm, and all other system parameters kept constant, the value of γ is calculated to be 0.34. The value is smaller since γ is directly proportional to the square of particle size (R_p^2). At this value of γ, the amount of capture for 500 nm particles is determined to be 24% from the figure. Thus, there is 100% capture of 800 nm particles while only 24% capture of 500 nm particles. This is an illustration of how, using the plot of θ vs γ, the system operating conditions for separation could be determined.

In conclusion, in this chapter, we developed an understanding of the physics of non-magnetic particles around an obstacle array through particle trajectory simulations. This understanding was helpful in proposing the principle of separation of a mixture of non-magnetic particle sizes. It also allowed us to design the geometry and operating conditions for carrying out the separation.

Using concepts proposed in this chapter, an experimental system can now be designed to demonstrate the preferential capture of larger non-magnetic particles. The next chapter will describe these experiments conducted to corroborate findings from particle trajectory simulations – first, qualitatively through capture visualization experiments, then quantitatively through pulse chromatography experiments and finally proof-of-principle separation experiments to demonstrate the potential of the system.

2.8 References –

1. Rosensweig, R.E., *Ferrohydrodynamics*. 1985, London: Cambridge University Press.

2. Griffiths, D.J., *Introduction to Electrodynamics*. 3rd ed. 1999: John Wiley.

3. Comsol, *User's Manual - Magnetostatics Applicaiton Mode*. 2009, Comsol Multiphysics.

4. Gonzalez , L., *Negative magnetophoresis of submicron species in magnetic nanofluids*, in *Chemical Engineering*. 2008, MIT: Cambridge MA.

5. Tejwani S., *Thermodynamic and Transport Properties of Nonmagnetic Particles in Magnetic Fluids*, in *Chemical Engineering*. 2009, MIT: Cambridge MA.

6. Pamme, N. and A. Manz, *On-chip free-flow magnetophoresis: Continuous flow separation of magnetic particles and agglomerates.* Analytical Chemistry, 2004. **76**(24): p. 7250.

7. Liu, C., L. Lagae, and G. Borghs, *Manipulation of magnetic particles on chip by magnetophoretic actuation and dielectrophoretic levitation.* Applied Physics Letters, 2007. **90**(18): p. 184109-3.

8. Moeser, G.D., et al., *Water-based magnetic fluids as extractants for synthetic organic compounds.* Industrial & Engineering Chemistry Research, 2002. **41**(19): p. 4739-4749.

9. Gonzalez L A, S.F., K A Smith, T A Hatton, *Magnetophoresis of Nonmagnetic, Submicrometer Particles in Magnetic Fluids.* SMA Transactions in Molecular Engineering of Biological and Chemical Systems (http://dspace.mit.edu), 2004.

10. Morgan H, G.N.G., *AC Electrokinetics: Colloids and Nanoparticles*. 2002, Hertfordshire, UK: Research Studies Press.

11. Deen, W.M., *Analysis of Transport Phenomenon.* 1998, New York, NY: Oxford University Press. pp. 4-5.

12. Moeser, G.D., et al., *High-gradient magnetic separation of coated magnetic nanoparticles.* AICHE Journal, 2004. **50**(11): p. 2835-2848.

13. Ditsch, A., et al., *High-gradient magnetic separation of magnetic nanoclusters.* Industrial & Engineering Chemistry Research, 2005. **44**(17): p. 6824-6836.

Chapter 3

Experimental demonstration of separation concepts

3.1 Introduction

This chapter will describe experiments performed to prove the basic principle of capture of nonmagnetic particles in the presence of large magnetic field gradients. In the previous chapter, we developed a single particle model in which we observed the dependence of capture on magnetophoretic force ratio γ as defined in equation (2.42).

$$\gamma = \frac{2\mu_0 H_0 M_f R_p^2}{9\eta a V_0} \tag{2.42}$$

In the following sections, we will discuss experiments performed to validate the capture mechanism of non-magnetic particles, both qualitatively and quantitatively. Previous attempts at understanding the focusing of nonmagnetic species in magnetic fluids were performed by Fateen [1] and Gonzalez [2]. The current experimental work focuses on capturing non-magnetic species at a larger scale so that this method can be ultimately useful in developing a particle separation technology.

First we will describe the synthesis of a magnetic fluid using a co-precipitation method proposed by Moeser [3] with some modifications. Next we will describe the capture visualization experiments where fluorescent polystyrene particles were immersed in the magnetic fluid and the mixture was then flowed through a region of magnetic fluid gradients. The resulting motion of particles was observed using fluorescence microscopy. The following section will discuss results from quantitative study of particle capture where experiments were performed to quantify the amount of capture and separation using fluorescence spectroscopy. Finally, we compare the experimental results with predictions from three dimensional particle tracking simulations.

3.2 Synthesis and characterization of magnetic fluid

The magnetic fluids used in this research consist of a stable suspension of magnetite (Fe_3O_4) particles in water. A picture of magnetic fluid is shown in Figure 3-1 where the dark brown magnetic fluid is displaying responsiveness to the application of a magnetic field. The structure of this suspension is shown in Figure 3-1.

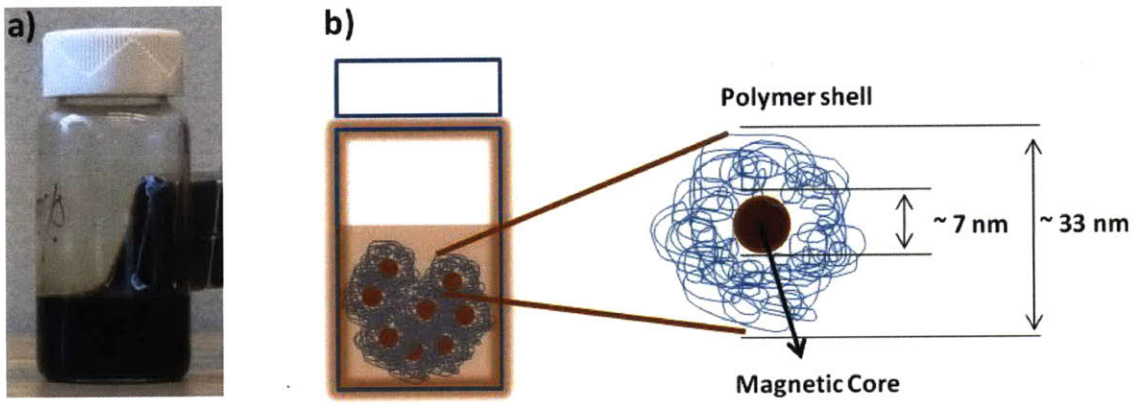

Figure 3-1: Magnetic fluid used in this research a) Response of a magnetic fluid to a magnet. b) Structure of a typical magnetic fluid suspension

The magnetite particles in the suspension are stabilized against aggregation and settling through a combination of thermal agitation and steric repulsion induced by the polymer shell. A variety of materials have been used in the past to coat the magnetite particles and provide stabilization such as graft copolymers [3], fatty acid surfactants [4] and phospholipid coatings [5].

Magnetic fluids can primarily be synthesized by two methods - size reduction and chemical co-precipitation. Co-precipitation is a faster and more economical method and results in a more uniform size distribution for particles in the suspension [6]. For the purpose of this research, co-precipition method as developed by Moeser [7] was used to synthesize magnetic fluid. In this method, synthesis was carried out by precipitating Iron chlorides (Fe2+ and Fe3+) in an aqueous solution of polyethylene oxide/polyacrylic acid (PEO/PAA) graft copolymer. The magnetic fluid, once synthesized was characterized to determine its properties. Transmission Electron Microscopy (TEM) was used to

determine the size of the magnetic cores. Dynamic light scattering (DLS) was used to determine the hydrodynamic diameter to obtain the size of polymer shell. Iron content of the magnetic fluid was determined using a colorimetric titration technique. Vibrating Sample Magnetometry (VSM) and Superconducting Quantum Interference Device magnetometry (SQUID) were used to determine the magnetization of this fluid.

3.2.1 Synthesis of magnetic Fluid

Detailed synthesis procedures for magnetic fluids of the type used in this thesis are described in detail in Moeser [7] . A brief description with minor modifications in this technique is presented below.

3.2.1.1 Materials

Ferric (III) chloride hexahydrate (97%), Ferrous (II) chloride tetrahydrate (99%), Polyacrylic acid sodium salt (50% solution in water, Mw = 5000) and ammonium hydroxide (28 wt% in water) were obtained from Sigma-Aldrich Chemical Company (Milwaukee, WI). Jeffamine XTJ-234 (PEO/PPO-NH2, PEO:PO = 6.1:1, Mw = 3000) was obtained as a gift from Huntsman Corp. (Houston, TX). All chemicals were used as received.

3.2.1.2 Graft co-polymer synthesis

Polyethyleneoxide (PEO)/polyacrylic acid (PAA) graft copolymer was synthesized through an amidation reaction between amine-terminated PEO chains and the carboxylic groups in PAA. The amine terminated PEO chains were grafted onto the PAA backbone through this reaction. Only 16% of the carboxylic groups were reacted with Jeffamine and the remaining 84% were left unreacted for subsequent attachment to the magnetite nanoparticle cores. Bulk polymerization was carried out by mixing 6 grams of 50% PAA solution with 20 grams of Jeffamine (XTJ-234). The resulting mixture was heated to around 40^0 C and mixed thoroughly to prepare a uniform solution. This solution was maintained at 180^0 C for two hours. Nitrogen was bubbled constantly through the mixture

to serve the dual purpose of mixing the reactants as well as removing water continuously. Water removal is essential to prevent occurrence of side reactions. The final product obtained was clear amber liquid that was readily dissolved in water to prepare a 33wt % solution. The typical reaction that takes place during synthesis is shown in Figure 3-2.

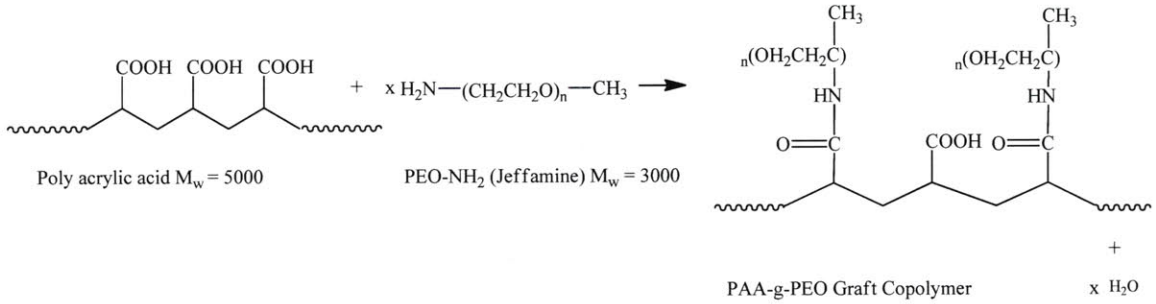

Figure 3-2 – Reaction between PAA and Jeffamine to synthesize the graft copolymer

3.2.1.3 Chemical Co-precipitation of Magnetic Fluid

Magnetite particles were prepared by precipitating Fe(II) and Fe(III) chlorides in a solution of PEO/PAA copolymer through the addition of ammonium hydroxide. The following reaction, as detailed in Moeser [7] takes place shown in Figure 3-3.

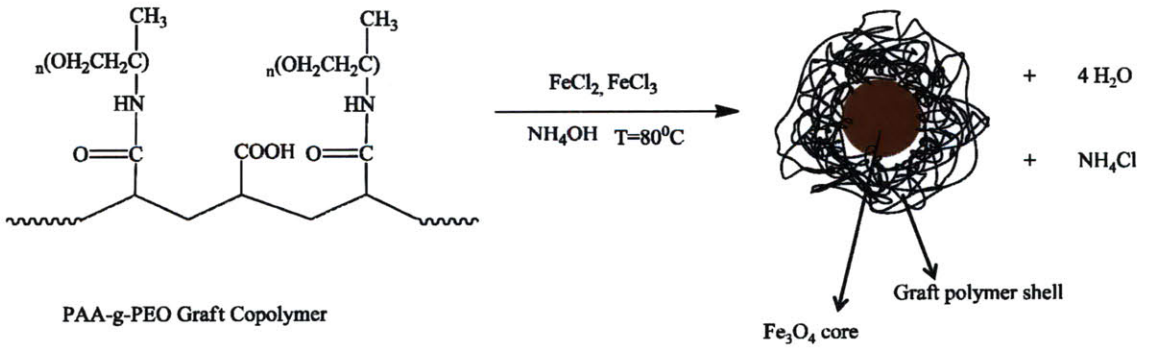

Figure 3-3 – Reaction taking place during magnetic fluid synthesis

In a typical synthesis reaction, nitrogen was bubbled through 40 ml de-ionized water for approximately 20 minutes, while continuously stirring to remove any dissolved oxygen. About 2.35g FeCl3.6H2O and 0.86g FeCl2.4H2O were added and the mixture was heated

to 72^0 C. Nitrogen flow was stopped at this point and 5 ml of 33% PAA/PEO polymer was added and the mixture was heated to 80^0 C. At this temperature, 6 ml of ammonium hydroxide (NH_4OH) was added to precipitate the magnetite particles instantly. The reaction mixture was stirred at 80^0 C for 30 minutes to ensure completion of the synthesis reaction and purge any excess ammonia. This mixture was cooled for 30 minutes before further processing.

3.2.1.4 Purification of magnetic fluid

The above synthesized magnetic fluid needs to be purified to remove excess reactants - excess polymer solution and dissolved ammonia and also to remove large aggregates formed during the synthesis. Large aggregates are formed due to insufficient/partial coating of polymer around some magnetite cores which then combine to form larger clusters. Sonication and filtration are required to remove these aggregates from the magnetic fluid. First, the magnetic fluid was sonicated for about 2 minutes using a wand sonicator (Branson Sonifier 450) in pulse mode to break up the aggregate magnetic cores. The fluid was then subjected to syringe filtration (Pall Corporation, Acrodisc® 25mm syringe filter) to remove larger magnetic clusters. This was performed in two stages – syringe filtration using a 400 μm cutoff filter and then using a 200 μm filter. Once the large aggregates were removed, the magnetic fluid was washed repeatedly using an ultrafiltration cell (Centricon Plus-70 from Millipore Corporation). Excess glycerin was rinsed from the filtration cell by centrifuging for 5 minutes with purified water. For purification of magnetic fluid, approximately 10 ml batches of magnetic fluid were diluted with 30 ml de-ionized water. This mixture was centrifuged for about 25 minutes with Centricon at the maximum allowable RPM. The concentrated magnetite particles obtained in retentate were re-suspended in 10 ml water. Excess ammonia and polymer were washed out in the filtrate. This procedure was repeated a second time to ensure complete removal of excess ammonia and polymer molecules. After synthesis and purification, approximately 40 ml magnetic fluid was available for further characterization.

3.2.2 Characterization of magnetic fluid

The synthesized magnetic fluid was characterized through various analyses to determine its iron content (titration), hydrodynamic diameter size distribution (DLS), core size distribution (TEM) and its magnetization (VSM, SQUID).

3.2.2.1 Iron content analysis

The amount of magnetite contained in a given volume of magnetic fluid determines its magnetization which in turn determines the strength of the fluid's response to the application of a magnetic field. Hence, it is important to determine the magnetite content as accurately as possible. An successful iron analysis technique has been previously described by others [8-9] which relies on colorimetric determination of iron content. A brief summary of the procedure for performing Iron content analysis is described below.

Exactly 40 µl of magnetic fluid is diluted by 5x to 200 µl and added to a 25 ml volumetric flask. 400 µl of concentrated HCl is added to this flask and the mixture is heated using a heat gun inside a fume hood. The resulting yellow mixture is allowed to cool. This ensures dissolution of magnetite cores by the concentrated acid. 0.6 ml of Tiron (4,5-dihydroxy-1,3-benzenedisulfonic acid, disodium salt) is added to the mixture to chelate free iron ions (Fe2+ and Fe3+) in the solution and thoroughly mixed. 3 ml of 4M NaOH solution is added to this mixture and resulting volume made up to 25 ml. The resulting mixture has a pH of above 9.5 and shows extremely strong absorbance at 480 nm. This absorbance can be measured using UV-Vis spectrophotometry and calibrated with iron content. Tiron is known to bind to both Fe^{3+} and Fe^{2+} equally well, and the absorbance at 480 nm has a linear correlation with concentration of iron ions in the solutions. An empirical relationship was developed previously [8-9] which gives fraction of iron content (%w/w) in the fluid as

$$\text{Weight Fraction (\% w/w)} = 0.0576 * (\text{Absorbance at 480 nm}) \quad (3.1)$$

Using this technique, the iron content of magnetic fluids was determined and the fluids were diluted to a concentration of 2% by weight for further use.

3.2.2.2 Transmission Electron Microscopy characterization of core size

The core size for synthesized magnetic fluid was determined using Transmission Electron Microscopy (TEM). In a TEM image, only the metallic core of a magnetite particle has enough contrast to be visible while the surrounding polymer coating is invisible. A TEM image obtained for the synthesized magnetic fluid is shown in Figure 3-4. The core diameters look significantly smaller than 20 nm and are quite polydisperse. The average core diameter was calculated to be 6.7 nm. Results from characterizations of earlier synthesis of magnetic fluids by this method by Moeser [7] are shown in Figure 3-5. On comparing Figures 3-4 and 3-5a, we observe qualitative similarities between the two. Moeser showed that the nanoparticle cores are single crystalline domains, which is an important characteristic giving rise to the superparamagnetic property in a magnetic fluid.

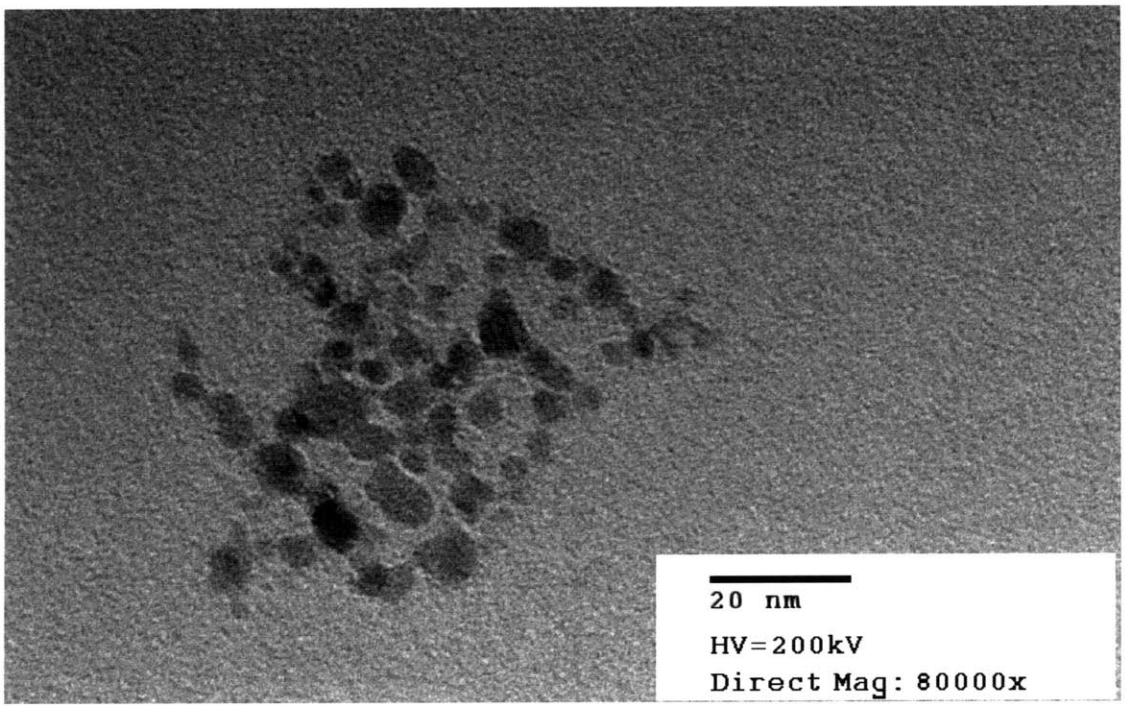

Figure 3-4: TEM image of magnetic cores of nanoparticles for synthesized magnetic fluid.

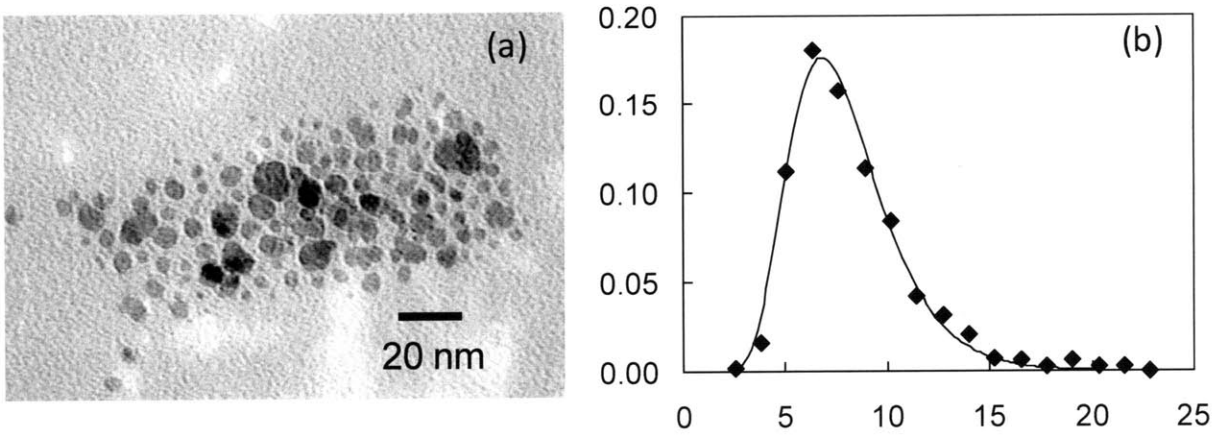

Figure 3-5: a) TEM results from Moeser [2] for magnetic fluid synthesized through a similar process. b) Core size distribution for this magnetic fluid.

3.2.2.3 Dynamic Light Scattering to determine hydrodynamic diameter

As seen above, TEM allowed us to determine the size of the magnetic core but not the polymer shell. To measure the overall diameter of the particle (core-plus-shell), we need the hydrodynamic diameter which can be measured using DLS. We used a Brookhaven BI-200SM light scattering system to determine the hydrodynamic diameter at a measurement angle of 90^0. The light scattering system measures scatter intensity data over time and translates it into the diffusion coefficient of particles. This diffusion coefficient data can be converted into a distribution of particle diameters using Stoke-Einstein equation (assuming spherical particles). DLS data (number averaged size distributions) for a typical batch of magnetic fluid is presented in Figure 3-6. The number averaged particle size was determined to be 33.6 nm and the particle sizes ranged between 26 nm and 60 nm (with a miniscule number of particles between 60 nm and 170 nm). The non-magnetic particles we disperse in the magnetic fluid are of the order of 200 nm. The magnetic particle size is much smaller than the non-magnetic particle size, and the mean free distance between the magnetic particles is also smaller than the non-magnetic particles. Thus, it is safe to assume that the magnetic fluid is a continuum in which the non-magnetic particles are immersed and subjected to magnetophoretic forces.

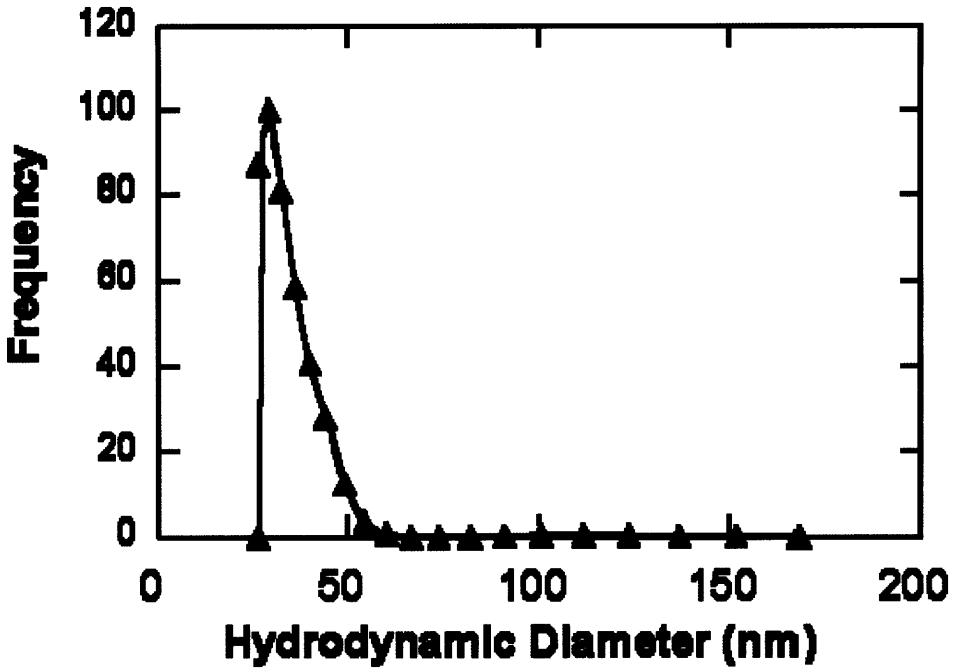

Figure 3-6: Number average hydrodynamic diameters of polymer coated magnetic nanoparticles

3.2.2.4 Magnetization measurements using VSM and SQUID

For the magnetic fluids used in this thesis, with magnetite core on the order of 7.5 nm, we can assume that the fluid is intrinsically superparamagnetic in nature [8]. The particles exhibit minimal interactions, and in the absence of a field, thermal agitation and rotation of the single domain magnetized particles results in zero net magnetization. However, on the application of even small magnetic fields, these particles align instantaneously and show a sharp increase in their magnetization. On application of sufficiently large fields, all particles get aligned and the magnetic field reaches saturation. This behavior can be measured by using either VSM or SQUID. Figure 3-7 shows the magnetization measurement for a 2 wt% magnetic fluid by both VSM and SQUID. The results match exactly for both VSM and SQUID confirming the super-paramagnetic behavior of the fluid. The magnetic fluid shows no residual magnetization at zero field but responds sharply on the application of a magnetic field with perfectly symmetric behavior for both

positive and negative applied field values. The fluid reaches saturation at a field of about 1 Tesla with a saturation magnetization of 929 A/m for a 2% fluid. Previous work has shown that this saturation value is proportional to the magnetite content in the fluid [7].

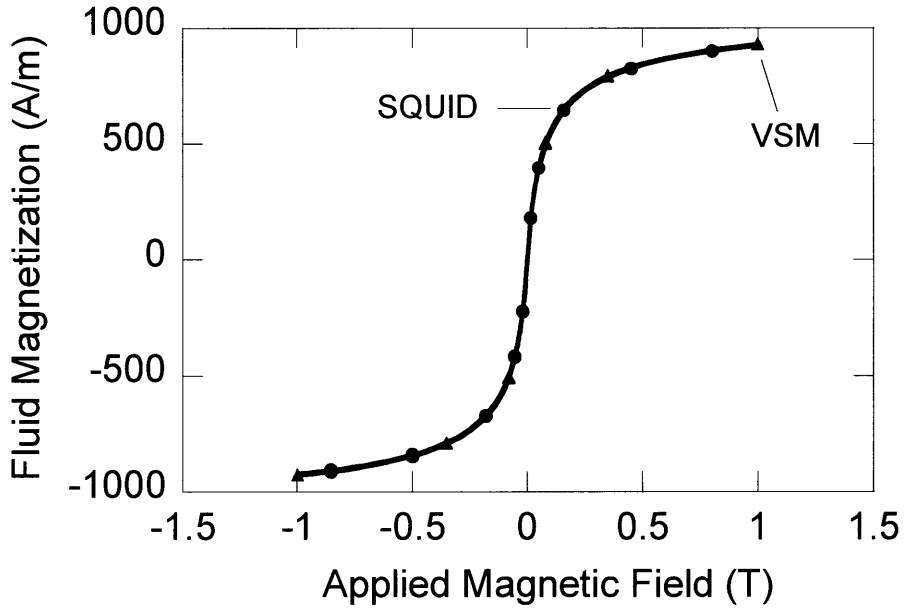

Figure 3-7: Magnetization of a 2% magnetic fluid measured using VSM and SQUID

3.2.3 Summary of magnetic fluid synthesis

In summary, a process for synthesizing a stable magnetic fluid using chemical co-precipitation has been described. This fluid consists of a magnetite core (Fe_3O_4) and a stabilizing shell consisting of graft copolymer with poly-ethylene oxide (PEO) side chains grafted onto a poly-acrylic acid (PAA) backbone. The resulting magnetic fluid has magnetic particles with average hydrodynamic diameter of approximately 35 nm. This magnetic nanoparticles size is small enough to provide a continuum environment for immersed polystyrene non-magnetic particles larger than 200 nm. This average core size of these nanoparticles is around 6.7 nm which results in super-paramagnetic behavior of the magnetic fluid. This was verified using VSM and SQUID which showed saturation magnetization for a 2% fluid to be 929 A/m. The next section describes non-magnetic

particle capture experiments which were performed using magnetic fluid synthesized using this procedure.

3.3 Magnetophoretic capture experiments – qualitative study

This section describes experiments performed to qualitatively demonstrate capture of non-magnetic polystyrene particles in the presence of a magnetic medium and on application of magnetic field gradients. Fluorescent polystyrene particles were suspended in a magnetic fluid and this mixture of particles and magnetic fluid was flowed through a set-up built to generate magnetic buoyancy forces on non-magnetic particles. Fluorescence microscopy was used to observe the behavior of particles under this force. The goal of these experiments was to obtain visual evidence of capture of non-magnetic polystyrene particles of larger sizes due to magnetic buoyancy forces while smaller particle sizes remained unaffected. This would qualitatively validate the principle for building a separation system. In the sections below are described the design of the experimental set up, description of experimental set up and procedure and finally the results and conclusions from visualization of magnetophoretic capture.

3.3.1 Design of experimental set up

The design of experimental set up was based on insights from particle trajectory simulations described in the previous chapter combined with practical considerations. While designing the experimental set up, it was important to optimize the design that would result in sufficient magnetic buoyancy force on larger polystyrene particles while allowing smaller particles to go through.

The experimental set up was designed to generate magnetic field gradients by having an array of cylindrical obstacles embedded in a transparent flow cell. A uniform magnetic field was to be applied on this obstacle array. Simulations were performed to optimize two sets of variables for this set up - the design variables and operating conditions. The design variables for the flow cell involved choosing the appropriate obstacle radius 'a', obstacle geometry, obstacle spacing and flow cell dimensions. Operating conditions

included choosing the appropriate incident fluid velocity (V_0) on the obstacle array, strength of applied magnetic field (H_0), magnetic field orientation relative to flow velocity, magnetic fluid strength which affects its magnetization (M_f) and particle radius of non-magnetic particles (R_p).

3.3.1.1 Design of obstacle geometry

To aid in the design, 2-dimensional particle trajectory simulations were carried for the specific experimental set up. These simulations use the same methodology as in Chapter 2, however now, the array of obstacles is finite (not periodic) and the operating conditions are chosen to mirror experimentally realizable values. The geometric design of the experimental set up is summarized in Table 3-1 which uses insights from particle trajectory simulations. A rhombic geometry of obstacles was chosen in order to have the most efficient capture. Other choices are systematically explained in the table. Once the geometry was specified, magnetic field simulations were performed to determine a magnet configuration that would allow application of a uniform field on the geometry.

Table 3-1: Design Parameters for capture visualization experiments

Parameter	Value/Range	Remarks
Obstacle Radius 'a'	200 μm	Smallest available/ machinable
Obstacle spacing	x direction: 2D y direction: 1.5 D	Practically machinable, D = 2a
Obstacle geometry	Rhombic	Maximum capture efficiency at any given γ
Flow cell width	4000 μm	To accommodate 5 wires in a row
Flow cell height	500 μm	Sufficiently thin for visualization
No. of obstacle rows	5	Row nos. 1,3,5 have five obstacles each. Row nos. 2 and 4 have four obstacles each

3.3.1.2 Design of magnet configuration to generate uniform magnetic field distribution

As explained earlier, magnetic field gradients were to be generated by applying a uniform magnetic field over an array of cylindrical iron obstacles. Magnetic field was applied parallel to the flow direction in the experimental flow cell. This was done by placing two bar magnets with poles aligned on each side of the flow cell as shown in Figure 3-8a. To ensure that the applied magnetic field was uniform, magnetic field simulations were performed in COMSOL®. For this purpose, actual dimensions of flow cell and geometric configuration were used in the simulation (Table 3-1). The goal of the simulation was not to verify the absolute value of magnetic field but rather to verify if the distribution generated by this magnetic configuration was uniform over the entire obstacle array. Simulation results for the experimental set up in Figure 3-8a show a uniform magnetic field generated over the entire cell. Large gradients are observed in the vicinity of iron obstacles. These results allow us to determine the appropriate spacing between bar magnets and the magnet configuration required to generate a uniform parallel magnetic field. Experimental measurements were performed to confirm results from simulations. The experimental measurement of applied magnetic field is shown in Figure 3-9. From the plot, we observe that magnetic field is roughly constant in the range between y = -0.0016 and +0.0016, with a value around 0.043 T. Figure 3-8b shows the flow field distribution for the experimental cell containing the obstacle array. In this simulation, a no slip boundary condition was assumed around the side boundaries of the flow cell.

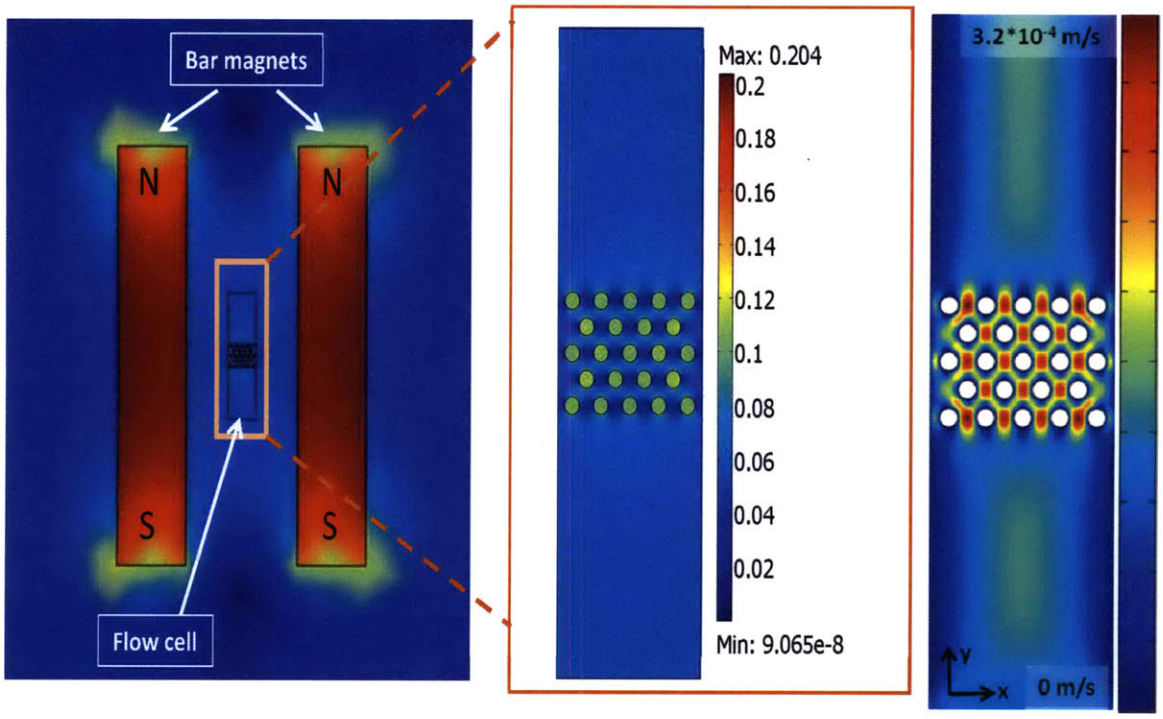

(a) (b)

Figure 3-8: Field profiles for the experimental set up (a) Magnetic field profile (magnitude of $|\underline{B}|$) (b) Flow field profile (magnitude of $|\underline{V}|$)

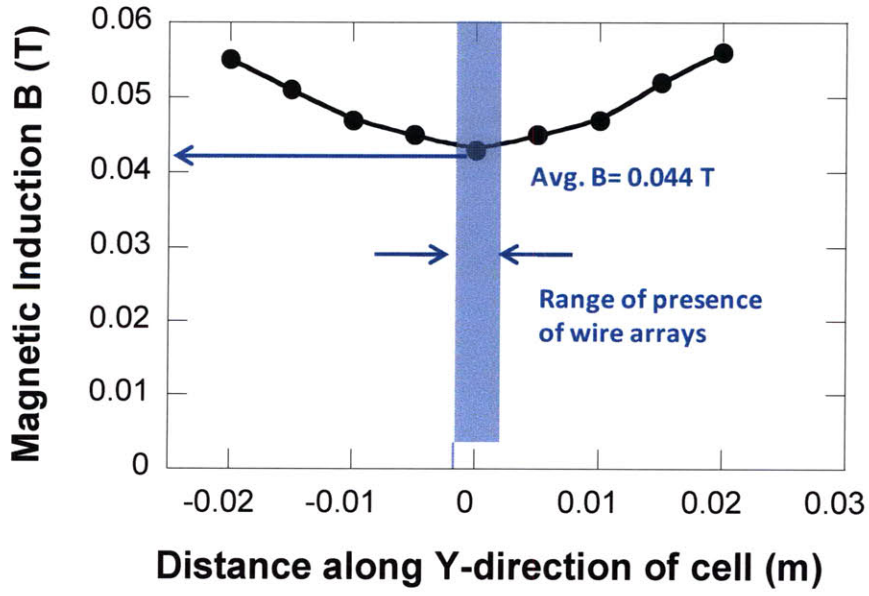

Figure 3-9: Experimental measurement of magnetic field profile generated

3.3.1.3 Design of operating conditions using 2D particle trajectory simulations

After determining the flow and magnetic fields for the experimental set up, two dimensional particle trajectory simulations were performed to determine the operating conditions. The procedure used was similar to the one described in section 2.6 of this thesis, however, the effect of no-slip boundary conditions on the side walls of the device was taken into account. The z-direction was assumed to be infinitely long so that gradients in this direction do not influence the flow or magnetic field. This assumption is reasonable for the magnetic field, in case of very long cylindrical obstacles. However, the width of the flow cell is thin enough such that the walls in z direction sufficiently influence the flow field. This is a limiting approximation for a two dimensional model. The typical two dimensional particle trajectories for various values of magnetophoretic ratio γ are shown in Figure 3-10.

It can be seen that γ_{min} for complete capture of particles is 0.15, which is a much smaller than γ_{min} observed in section 2.6.3 for a rhombic array (with infinite periodic obstacles). The reason for this discrepancy is the presence of no-slip boundary conditions on the boundaries of the device which were absent in the previous case. In order to pick the right set of operating conditions, a plot of capture efficiency vs γ was generated for the set up which is shown in Figure 3-11. From this plot, we observe that the range of γ should be between 0 and 0.15, in order to observe the capture behavior of particles on the obstacle array. Based on this range of γ, the operating conditions such as the range of V_0 and values of applied H_0, M_f and R_p for experiments were determined, and are summarized in Table 3-2.

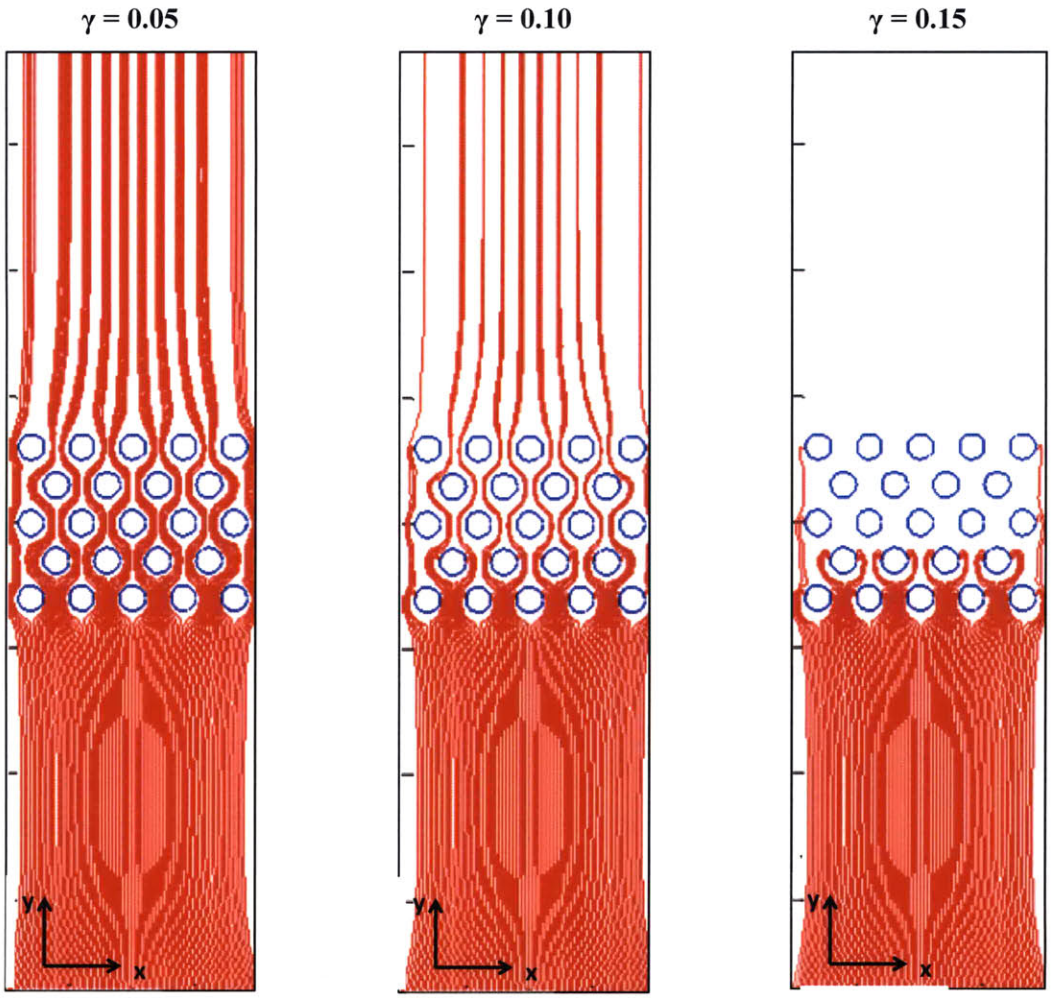

Figure 3-10: Typical particle trajectories for three different values of gamma – a) $\gamma = 0.05$ b) $\gamma = 0.10$ c) $\gamma = 0.15$

Table 3-2 Operating Parameters for capture visualization experiments

Parameter	Units	Value/Range	Remarks
Velocity of fluid V_0	m/s	0.00005 to 0.0006	From particle tracking simulations
Fluo. particles Radius	nm	200, 500, 900	Available sizes
Magnetic Field H_0	A/m	$3.6*10^4$	Limited by magnet strength
Magnetic Fluid Strength	Wt%	2%	Controlled by synthesis
Fluid Magnetization H_0	A/m	375 A/m	Interpolated from MH Curve
Fluid Viscosity η	Pa.s	0.001	Same as water [10]

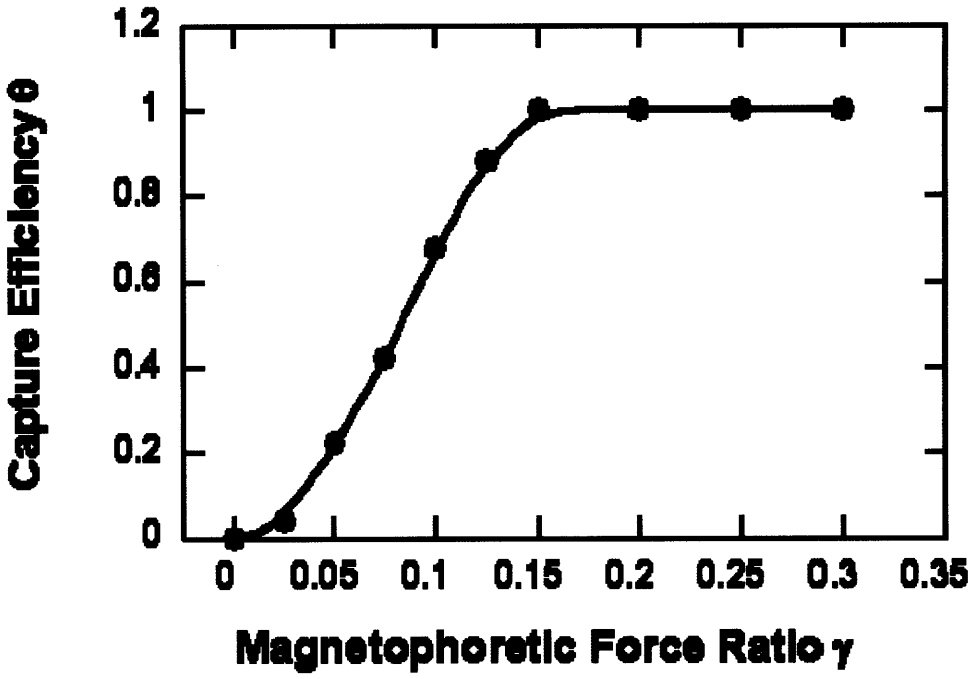

Figure 3-11: Capture Efficiency vs. γ plot for experimental set up based on 2D particle trajectory simulations

In this section, we looked at the determination of design and operating variables for the experimental set up. The next section provides a detailed description of experimental set up and materials.

3.3.2 Experimental Methods

3.3.2.1 Materials

Fluorescently tagged polystyrene beads were purchased from Duke Scientific (Palo Alto, CA). Their particle size, excitation and emission maxima are listed in Table 3-3. The fluorescent dyes have been incorporated into the polymer matrix and hence, the fluorophores do not leach during the course of experiments.

Table 3-3: Particle size, excitation and emission maxima for fluorescent particles.

Particle Size	Excitation Maxima	Emission Maxima
200 nm	468 nm (blue)	508 nm (green)
500 nm	468 nm (blue)	508 nm (green)
900 nm	468 nm (blue)	508 nm (green)

These particles were diluted from 1% w/v to a 0.05% w/v suspension in the magnetic fluid. The strength of magnetic fluid used was 2 wt% synthesized as described in section 3.2. De-ionized water was used to flush the flow cell. Stainless steel pins were embedded in the flow cell to generate the obstacle array. Polyacrylate was used to create a transparent flow cell. Neodymium cube magnets (10x10x10 mm) with maximum field at the surface of about 1.3 Tesla, were purchased from Indigo Corporation (Toronto,ON) and joined end to end with poles aligned to create a longer bar magnet.

3.3.2.2 Experimental sample preparation

A typical composition of experimental mixture is shown in Table 3-4. Magnetic fluid (3.28 wt%) was diluted to 2 wt% in the final mixture. The fluorescent particles with 1% w/v were used as purchased and diluted to 0.05% w/v in the final mixture, sugar solution prepared with density 1.269 g/cc using Sucrose ($C_{12}H_{22}O_{11}$, Mallinckrodt Baker, Inc, Phillipsburg, NJ), and de-ionized water. The mixture was agitated using a vortex mixer and sonicated for 5 minutes to allow for uniform mixing of components.

Table 3-4 Typical experimental mixture composition

Component	Amount	Composition in mixture
Magnetic Fluid 3.28 wt%	3.7 ml	2 wt% MF
Fluorescent particles 1% w/v	300 µl	0.05% w/v
Sugar solution 1.268 g/cc	0.8 ml	1.05 g/cc
Water	1.5 ml	
Final Mixture	**6.3 ml**	

3.3.2.3 Description of experimental set up

Based on the design specifications of geometry and operating conditions, an experimental set up was constructed. This set up had the ability to observe non-magnetic particles even as small as 200 nm using fluorescence microscopy. A schematic of the experimental setup is shown in Figure 3-11. Photographs of actual set up are shown in Figure 3-13.

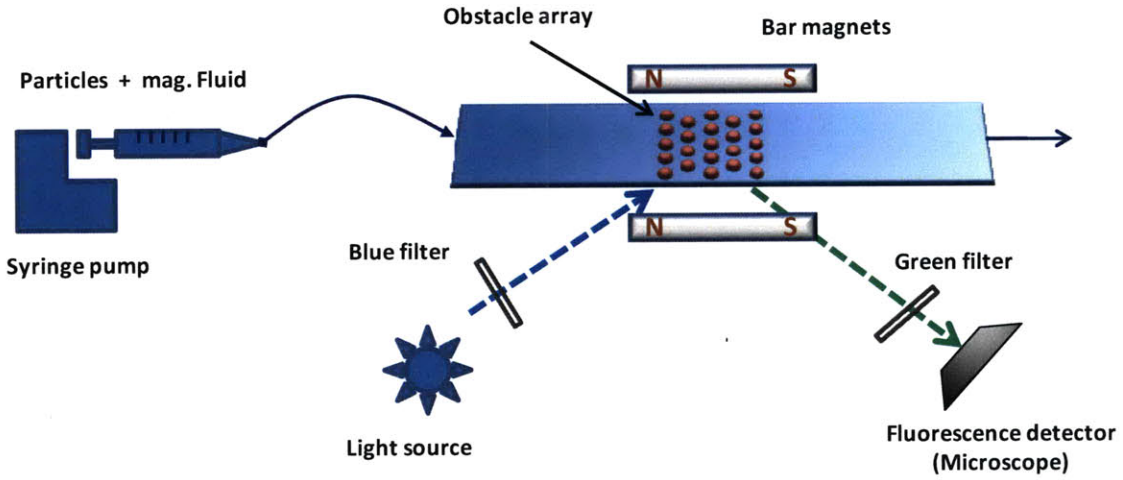

Figure 3-12: Schematic of Capture Visualization Experiments

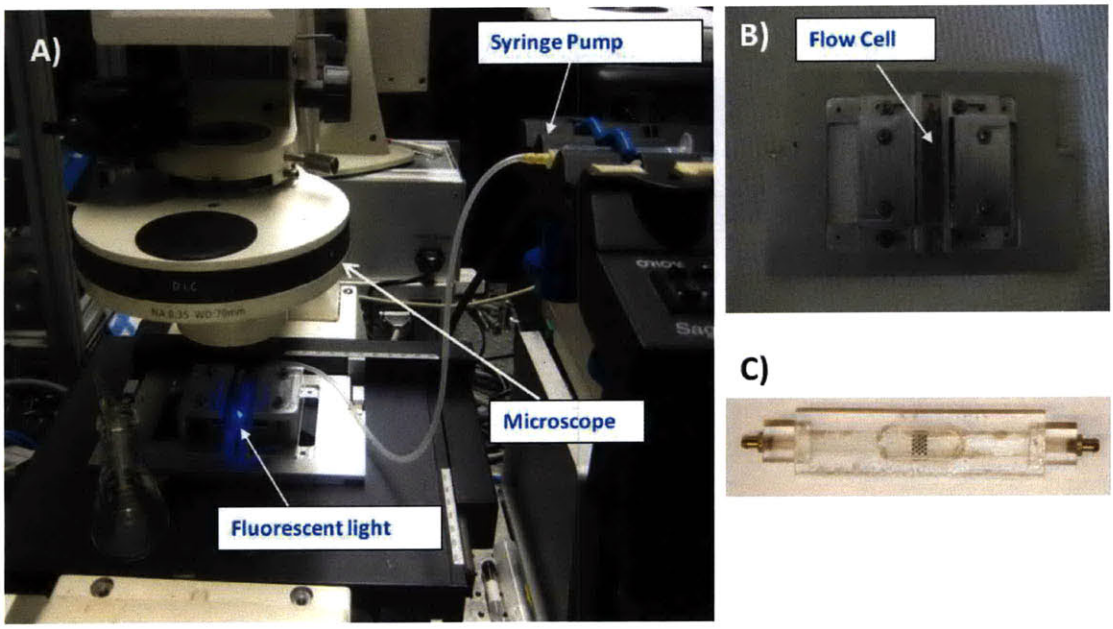

Figure 3-13: Pictures of a) microscope set up b) flow cell holder c) flow cell for experiments

At the heart of the set-up is a transparent poly-acrylate flow cell shown in Figure 3-13c which contains the array of cylindrical iron obstacles embedded in the designed geometry at the center. The array contains 5 rows of cylindral obstacles (diameter = 400 μm) in a rhombic arrangement. Magnets are placed around the flow cell with poles aligned, as explained earlier and held in position using a custom designed flow cell and magnet holder made of anodized aluminum shown in Figure 3-13b. The flow cell and holder were both machined at the MIT central machined shop. This holder could attach to a fluorescent microscope (CarlZeiss Axiovert HAL 100). Blue light in the range of 470 nm to 490 nm was allowed to shine on the embedded wire array and continuous fluorescent images were obtained using the combination of a 2.5X magnification lens (CarlZeiss Fluar 2.5x) and microscope camera (CarlZeiss Axiocam). The Zeiss Fluar lens was specifically chosen since it has a larger aperture making it sensitive to even a weak fluorescent signal. A mixture of 2 wt% magnetic fluid and 0.05% v/v fluorescent polystyrene particles of a specific size was prepared. Sucrose ($C_{12}H_{22}O_{11}$, Mallinckrodt Baker, Inc, Phillipsburg, NJ) was added to increase the specific gravity of the mixture to 1.05 to match that of the beads making the mixture neutrally buoyant. This mixture was passed through the flow cell at a constant rate with the help of a syringe pump (Sage M365, Orion Corporation, PA) to maintain a specific flow velocity over the wire array. Care was taken to ensure there are no air bubbles inside the wire array that could distort the flow profile. At t=0, bar magnets were placed in holder to apply a uniform magnetic field on the obstacle array. Magnets were removed after allowing sufficient time for capture and build up of fluorescent polystyrene particles on the wire array. Camera was switched off once the buildup dissolved.

3.3.2.4 Image acquisition from the microscope

The typical image acquisition set up for experiments is shown in Figure 3-14. The flow cell capture zone is illuminated with blue light from a UV lamp source (EXFO Inc). The fluorescent signal is captured through a low magnification lens with high sensitivity for fluorescence (Zeiss Fluar 2.5X) which is then sent to a CCD camera (Zeiss Axiocam). The images from camera are constantly sent to a data acquisition system in a computer which stores these sequential images. Images are taken at regular intervals (5 seconds) for

about 20 minutes to track the particle behavior in the flow cell over time. These sequential images can be pieced together through any image manipulation software to create a movie of particle behavior.

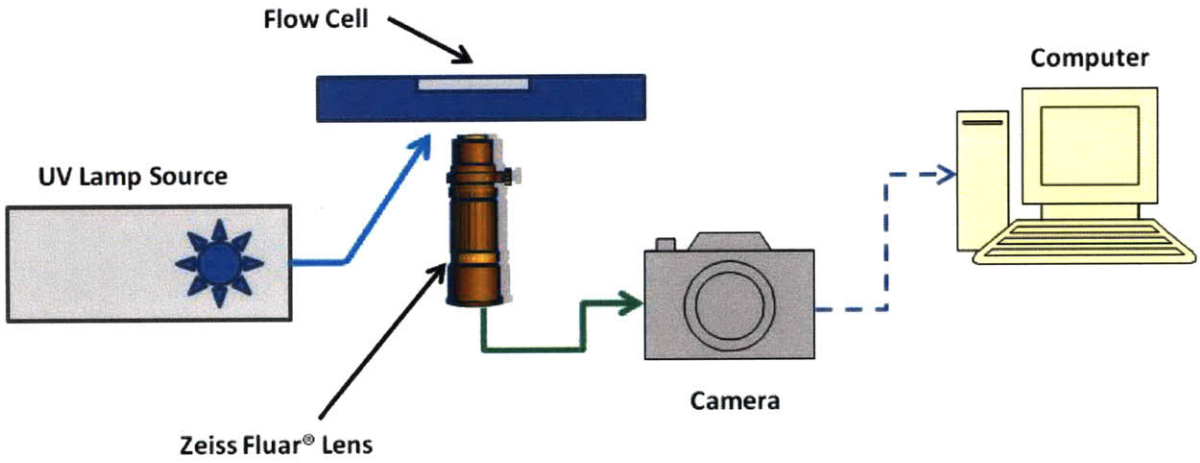

Figure 3-14: Image acquisition set up for fluorescent particle capture experiments

3.3.3 Experimental results and discussion

In this section, the results obtained from visual observation of particle focusing will be discussed. In a typical experiment, the sample mixture of non-magnetic particles and magnetic fluid was passed through the experimental set up with magnets turned on for approximately 20 minutes. In the case where non-magnetic particles were large enough to be captured, this was sufficient time for the capture build up to saturate around the obstacle array. First, the behavior of non-magnetic particles over time is discussed in the presence and absence of magnetic field. Later, the discussion focuses on the effect on capture behavior when varying different experimental variables - particle size R_p, flow velocity V_0, field direction and magnetophoretic force ratio γ.

Typical image from a particle capture experiment is shown in Figure 3-15a with a magnetic field distribution for this array in Fig 3-15b. The array of cylindrical obstacles in the designed geometry can be seen in form of dark green circular spots. There are 23 obstacles in total arranged in 5 rows (five obstacles in each of the odd rows numbered 1,

3 and 5; four obstacles in each of the even rows numbered 2 and 4). The particle and magnetic fluid mixture is flowed in the –y direction and magnetic field is applied parallel to the flow. In Figure 3-15a, there is evidence of capture due to magnetic buoyancy forces. The buildup due to capture of fluorescent particles occurs between the cylindrical obstacles in the x-plane – a maximum of 18 capture zones exist where buildup can be observed as bright florescent spots. In the absence of capture, there are no fluorescent spots and a dark-green grainy background is observed. A time series of images such as Fig. 3-15a can be used to determine the time evolution of behavior of non-magnetic particles on the application of a magnetic field. Figure 3-15b shows the corresponding magnetic field distribution that generates the magnetic buoyancy forces which allows this particular capture behavior. Particles experience magnetic buoyancy forces in the direction of decreasing magnetic field and get directed toward minima of magnetic field. For an applied field in y direction, the field minima are always located in the x-plane of each wire.

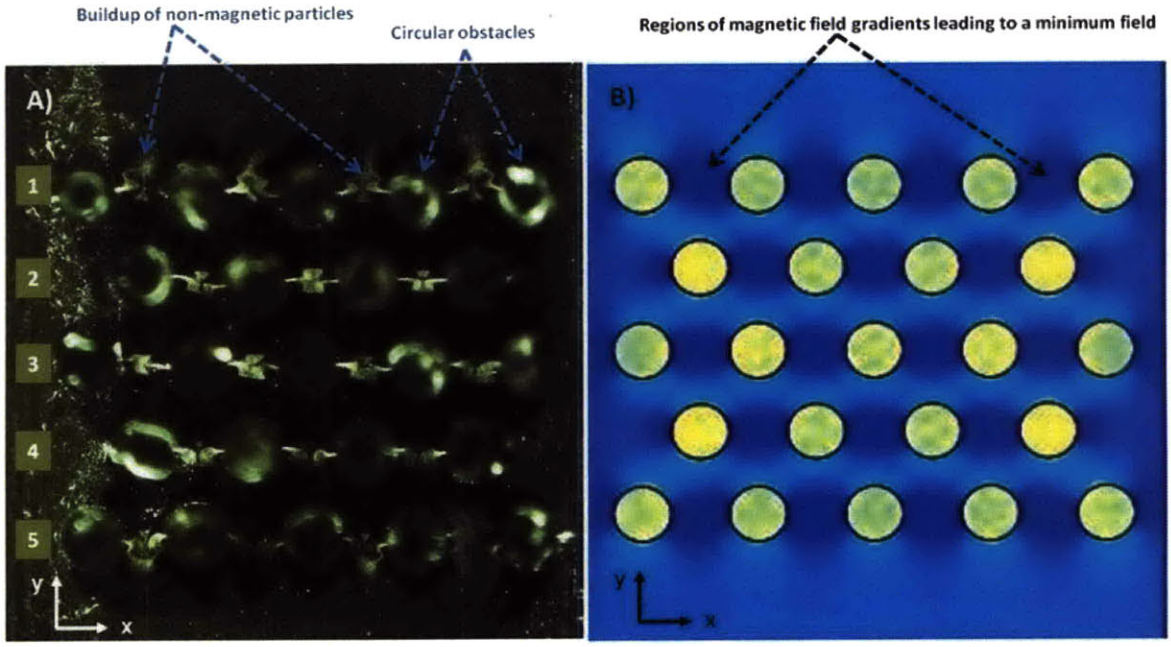

Figure 3-15 a) Typical buildup image obtained during particle capture experiments b) Magnetic field distribution for this obstacle array. It can be observed that minima of magnetic fields coincide exactly with regions of buildup of non-magnetic particles

3.3.3.1 Capture behavior of 900 nm particles

Figure 3-16 shows the results obtained as a series of images which were obtained when fluorescent 900 nm particles, immersed in a 2% MF and flowed at a velocity of 0.05 mm/s over the wire array with the magnetic field switched on at T = 0. Magnetic field of 0.044T was applied parallel to the flow using a bar magnet. It can be seen that initially (T=0), there is no buildup of fluorescent particles and particles are flowing uniformly across the wire array. However, as time progresses, the capture zones on wires (in the x-plane) gradually become brighter. By the time T=500s, it can be seen that most of areas between the wires are covered with bright fluorescent spots. On allowing the set up to reach close to steady state (T=1000s), it can be seen that the buildup between the wires consolidates into a tighter structure (the fluorescent spots become smaller and brighter). A video [11] was produced combining the image sequence from which we can observe the capture behavior of fluorescent particles. On removing the magnetic field, the buildup dissolves rapidly and the wire array reaches the initial state of T=0 in a few seconds. This experiment proves the basic principle of capture of nonmagnetic particles on the application of magnetic buoyancy forces. As explained in previously in Figure 3-15b, the buildup occurs in regions of magnetic field gradients that lead to field minima.

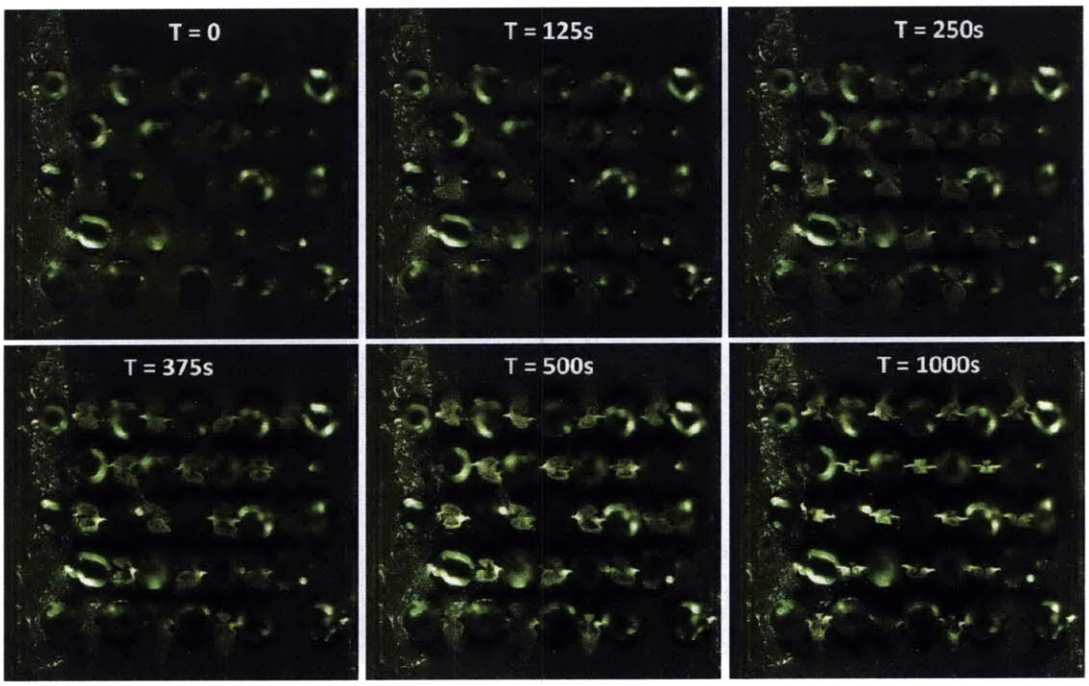

Figure 3-16: Evolution of Buildup of 900 nm particles over time on a wire array

3.3.3.2 Effect of particle size on capture behavior

To understand the effect of size of non-magnetic particles on capture, the previous experiment was repeated for three different particle sizes – 200 nm, 500 nm and 900 nm. A flow velocity of 0.1 mm/s was used and all other experimental conditions were same as before. The final states of build up from these experiments are shown in Figure 3-17. It can be seen that increasing particle size results in a greater number of fluorescent spots on the obstacle array. A buildup coverage (C) can be defined to understand the extent of capture as

$$C = \frac{\text{Actual buildup fluorescence spots}}{\text{Maximum possible buildup fluorescence spots (=18)}} \tag{3.2}$$

The coverage calculated for different particle sizes is shown in Table 3-5. The calculation for coverage is approximate since in some cases, only partial buildup occurs between wires and cannot be accounted for appropriately through this definition.

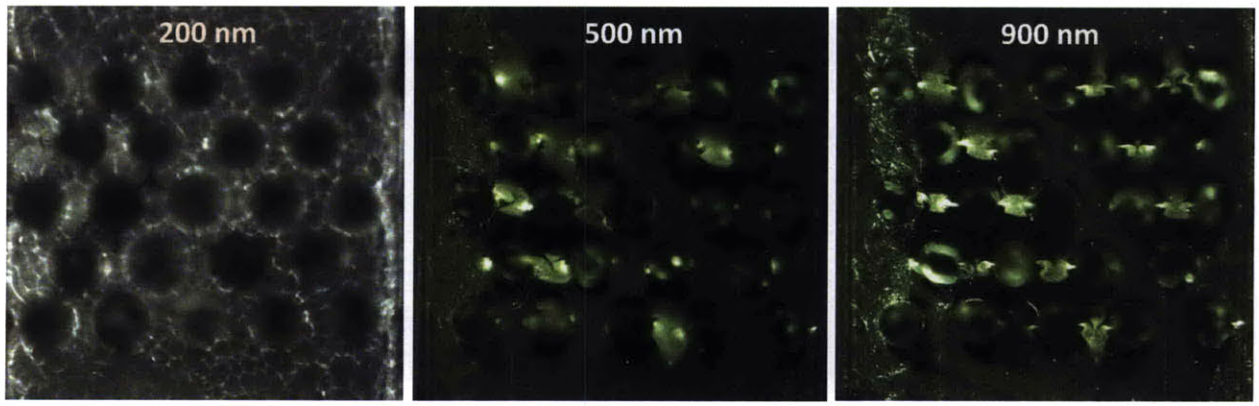

Figure 3-17: Effect of non-magnetic particle size on capture behavior

Table 3-5: Buildup Coverage variation on changing particle size

Particle Size (nm)	Number of capture zones	Coverage C	Magnetophoretic force ratio γ
200	**0**	**0**	**0.002**
500	**6**	**33%**	**0.011**
900	**11**	**61%**	**0.036**

From the results in Table 3-5, it is clear that as non-magnetic particle size increases, greater amount of capture is observed as reflected in a higher coverage. The obtained results are qualitatively consistent with our model, which suggests that capture depends on the magnetophoretic force ratio γ, which scales as square of particle radius R_p in Equation (2.42)

3.3.3.3 Effect of flow velocity

To study the effect of input flow velocity (or superficial velocity V_0) on particle capture, experiments were performed for a sample mixture of 500 nm particles in a 2% MF and an applied uniform field of 0.043T parallel to the flow direction. The sample mixture was introduced into the flow cell at different V_0 each time and observations were recorded. Figure 3-18 shows the results from these experiments. It can be observed that as flow velocity decreases, the behavior of nonmagnetic particles changes from no capture to significant capture. This is more apparent from results in Table 3-6 where we see that the buildup coverage C increases from 0% to 100% on decreasing the velocity from 0.6 mm/s to 0.031 mm/s. The magnetophoretic force ratio γ is inversely proportional to V_0. As V_0 decreases, γ increases which results in stronger magnetophoretic force leading to greater deviation from fluid streamlines and thus, a higher capture results.

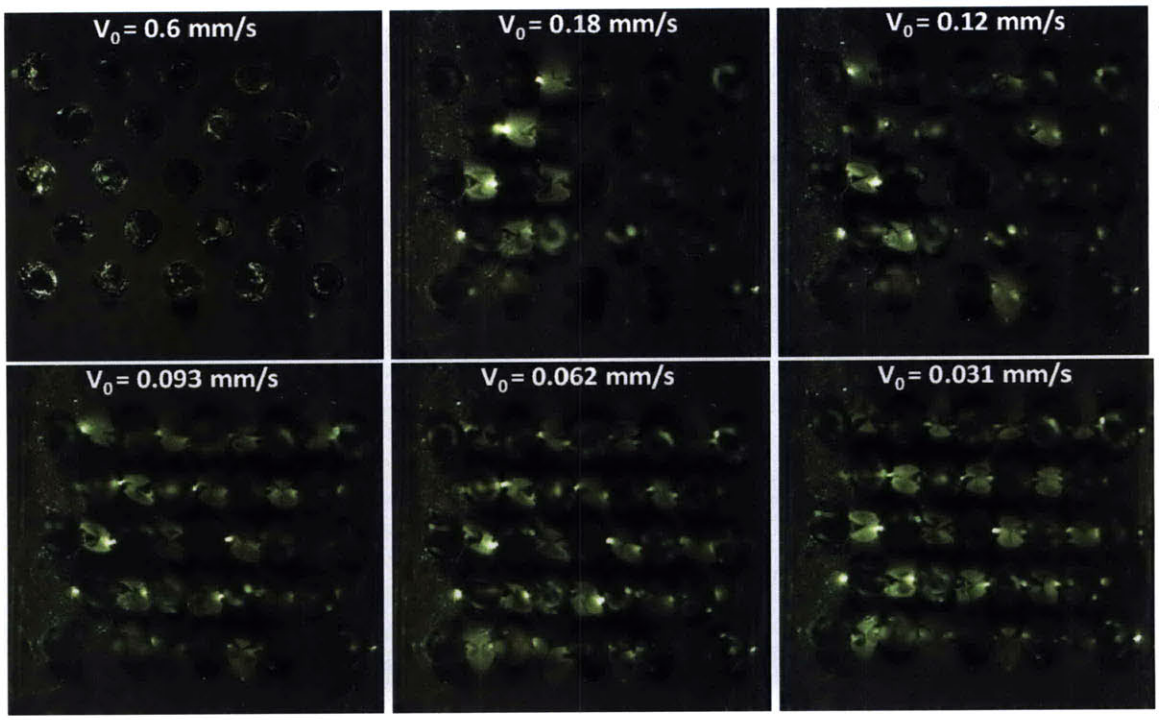

Figure 3-18: Variation of capture for 500 nm non-magnetic particles with input flow rate

Table 3-6 - Buildup Coverage variation on changing input flow rate for 500 nm particles

Flow velocity V_0 (mm/s)	Number of capture zones (max: 18)	Buildup Coverage C	Magnetophoretic force ratio γ
0.6	0	0	0.002
0.18	5	28%	0.006
0.12	6	33%	0.009
0.093	14	78%	0.012
0.062	17	94%	0.018
0.031	18	100%	0.036

3.3.3.4 Effect of magnetophoretic force ratio γ on capture

As described in the previous chapter, the Lagrangian particle trajectory model shows that capture behavior of nonmagnetic particles in a given flow field depends only on two non-dimensional numbers - Magnetophoretic ratio γ and the Reynolds number Re. The effect

of Reynolds number variation is small (Re<<1) since the flow field regimes and the flow field distribution do not change dramatically on varying the flow velocity within a limited range less than 0.001 m/s. Hence, γ predominantly governs the capture behavior of particles. In the experiments described previously, variation of individual experimental variables ultimately changed γ which affected the amount of capture. Effect of γ on capture can also be verified directly by relating buildup coverage with γ for two different particle sizes – 500 nm and 900 nm. According to the particle trajectory model, regardless of non-magnetic particle size, the amount of capture should be same for a given value of γ. This will be the focus of next set of experiments. Table 3-6 from the previous section shows the variation of capture behavior with changing γ for 500 nm particles. On changing γ from 0.002 to 0.036, coverage C changes from 0 to 100%. Similar set of experiments were repeated with 900 nm particles for a similar range of γ's. The final buildup profile images are shown in Figure 3-19 and coverage results are tabulated in Table 3-7 below.

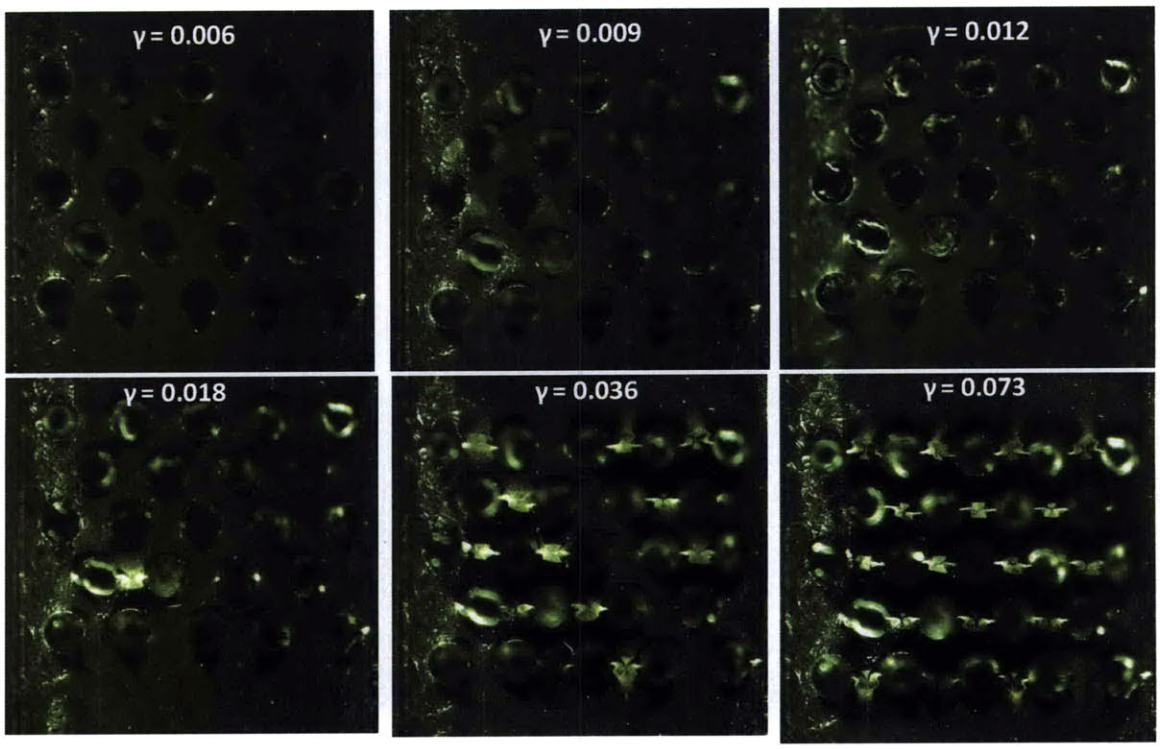

Figure 3-19: Variation of capture for 900 nm particles with magnetophoretic ratio γ

Table 3-7 Buildup coverage variation on changing input flow rate for 900 nm particles

Flow velocity V_0 (mm/s)	Number of capture zones (out of 18)	Buildup Coverage C	Magnetophoretic force ratio γ
0.6	0	0	0.006
0.4	0	0	0.009
0.3	0	0	0.012
0.2	1	6%	0.018
0.1	11	61%	0.036
0.05	17	94%	0.073

The results for 900 nm particles in Table 3-7 again show a trend similar to that observed for 500 nm particles. As the flow velocity is decreased and the value of γ increases, the amount of capture and consequently the buildup coverage increases from 0 to 94%. However, on comparing results between 500 nm and 900 nm particles (Table 3-8) it becomes apparent that maintaining similar γ across two different particle sizes leads to very different outcomes. We can observe that for the same value of γ, 500 nm particles are captured much more readily than 900 nm particles. In effect, 900 nm particles seem to require much higher values of γ for the same amount of capture when compared to 500 nm particles. This is an unexpected observation from the experimental results. Experiments quantifying amount of particles captured have been performed in the next section which confirm the deviation of behavior from the particle trajectory model.

Table 3-8: Capture behavior as a function of γ across two different particle sizes

Magnetophoretic force ratio γ	Buildup Coverage - 500 nm	Buildup Coverage - 900 nm
0.002	0	NA
0.006	28%	0
0.009	33%	0
0.012	78%	0
0.018	94%	6%
0.036	100%	61%

3.3.3.5 Effect of switching field direction

The results presented until now involve the applied magnetic field in 'y' direction parallel to sample flow, which can be referred to as the 'parallel' configuration. The applied field direction can be switched to point along 'x' axis, so it is perpendicular to the direction of flow (y direction), and is called the 'perpendicular' configuration. To understand the effect of switching the field direction, two capture experiments were performed for 900 nm particles with same magnetophoretic ratio γ, but in both parallel and perpendicular configurations. The results are presented in Figure 3-20. In a parallel configuration, capture zones are located between the wires along the x-plane as observed previously. However, when the field direction is switched to a perpendicular configuration, the particle capture zones also switch by 90^0, and the buildup occurs in the y-plane in-front-of and behind the wires. Figure 3-21 shows the magnetic field distribution for parallel and perpendicular configurations. It can be seen that the dark-blue regions, which are regions of magnetic field minima rotate by 90^0 in magnetic field distribution as well. These results corroborate observations from particle tracking simulations (Figure 2-20) in Chapter 2 that show that focusing and capture of particles switches by 90^0 on rotating the applied field by 90^0.

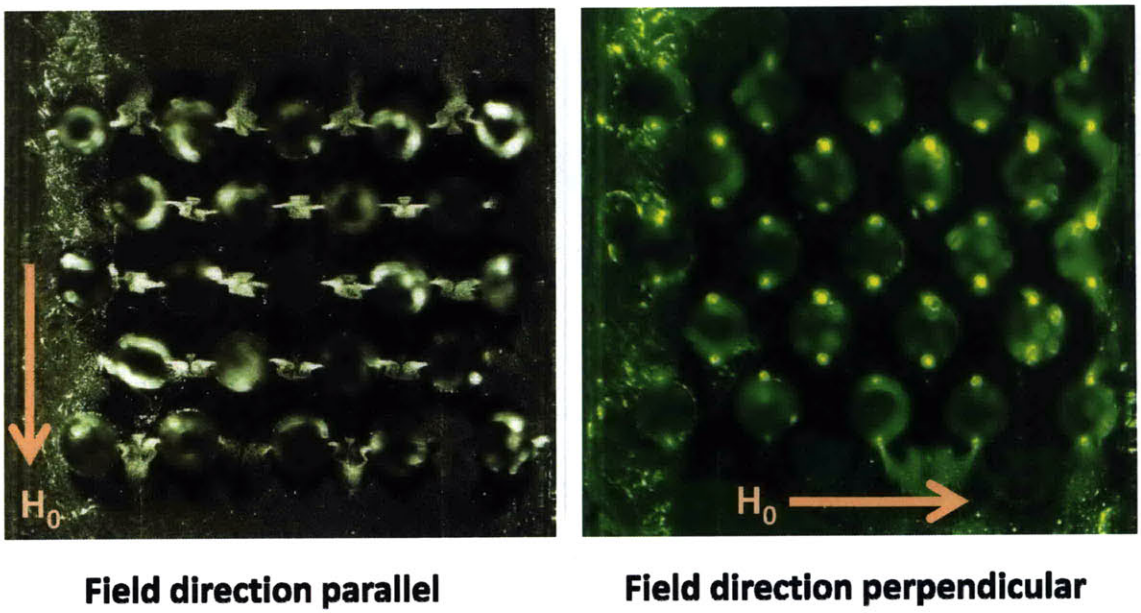

Figure 3-20: Capture experiments, $\gamma = 0.29$, 'parallel' and 'perpendicular' configurations

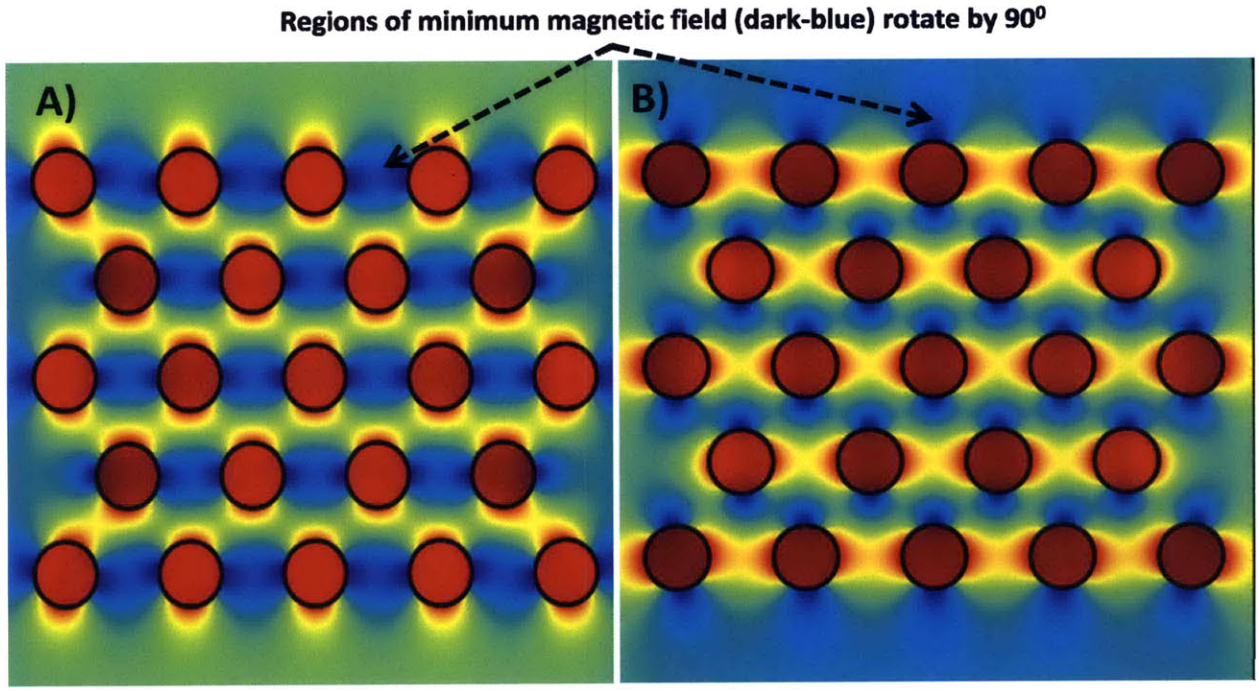

Figure 3-21: Magnetic field distribution for 'parallel' and 'perpendicular' configurations

3.3.4 Conclusions from qualitative experiments demonstrating non-magnetic particle capture

In this section, qualitative results from experiments demonstrating capture of non-magnetic fluorescent polystyrene particles were shown. The experiments showed that when nonmagnetic particles were immersed in a magnetic environment, and subjected to an inhomogeneous magnetic field, they were focused towards zones of magnetic field minima resulting in their capture. This capture phenomenon was demonstrated to be size dependent. Only when large particles that magnetic buoyancy force caused significant variations in their particle trajectories, capture was observed.

The particle trajectory model for capture was verified by determining the dependence of capture behavior of particles on magnetophoretic ratio γ through experimentally varying parameters such as incident flow velocity V_0 and particle size R_p. More buildup coverage C (as observed through more fluorescent build up) and hence higher capture was observed in two scenarios – either when V_0 was reduced or when R_p was increased.

According to our single particle trajectory model, γ is inversely proportional to V_0 and is directly proportional to R_p^2, thus γ is predicted to increase in both scenarios. Thus, capture visualization experiments qualitatively validated single particle trajectory model.

Fluorescence microscopy experiments were performed for two magnet configurations – 'parallel' and 'perpendicular' to understand the effect of magnetic field direction. The results showed that for a parallel configuration, fluorescent non-magnetic particle buildup occurs on the obstacles in the x-plane (perpendicular to flow direction). However, when the field is rotated to a perpendicular configuration, the capture zones rotate by 90^0 as well. Comparison with magnetic field distributions showed that captures zones fall closely around the magnetic field minima due to focusing of non-magnetic particles in these regions.

Finally, capture experiments were also performed to qualitatively relate capture amount to γ for different particle sizes. In this situation, particle trajectory model suggests that the capture behavior should depend purely on the value of γ. However, the experimental results showed that for a smaller R_p, the capture occurred much more readily (at a much smaller γ) than for a larger particle size. This is a deviation from the single particle trajectory model. To understand the quantitative validity of the proposed model, and to understand the extent of deviation from the model, the amount of capture needs to be quantified. Capture quantification experiments were carried out and are the topic of next section.

In conclusion, capture visualization experiments provided the proof of principle for capture of non-magnetic particles immersed in a magnetic medium. These experiments also verified the size dependent nature of magnetic buoyancy force which is the governing principle for developing a size based separation system using magnetic buoyancy forces.

3.4 Magnetophoretic capture experiments – a quantification study

This section describes experiments performed to quantify the amount of capture of non-magnetic polystyrene particles immersed in a magnetic medium on application of an inhomogeneous magnetic field. Magnetic fluid was flowed through a set-up built to generate magnetic buoyancy forces on non-magnetic particles. A controlled pulse of fluorescent nonmagnetic particles was injected into the flow stream. The amount of particles captured by the obstacle course was quantified using fluorescence spectroscopy. These experiments built on the results from the previous section and quantitatively demonstrated the effectiveness of magnetic buoyancy forces in performing submicron separations. The following sections describe modification of the experimental set up in order to demonstrate quantitative capture, the experimental procedure and the results and conclusions from these experiments. Finally, a comparison of experimental results with predicted capture efficiencies from Lagrangian particle tracking simulations are provided.

3.4.1 Design of experimental set up

3.4.1.1 Design of obstacle geometry

The experimental set up used for capture quantification experiments was similar to that used for capture visualization experiments with a few modifications. A transparent poly-acrylate flow channel was constructed as before for use as a capture device with an array of cylindrical posts embedded in a rhombic geometry through this cell. Since, the interest in these set of experiments was to quantify the capture, a larger number of obstacle rows were used. The flow cell incorporated a total of 325 obstacles arranged in 65 rows in a modified rhombic configuration. The original rhombic array was modified to address issues of channeling observed in previous experiments. The channeling is shown in Figure 3-22a. The gap between wires flow cell boundary provided a channel for particles to escape, thus reducing capture efficiency of this geometry. The modification of array

geometry is illustrated in Figure 3-22b. It can be observed that through shifting alternate rows of wires towards either left or right, the existing channels are plugged. The exact specifications of wire spacing and wire diameter as described in Table 3-1 hold true for the modified design as well.

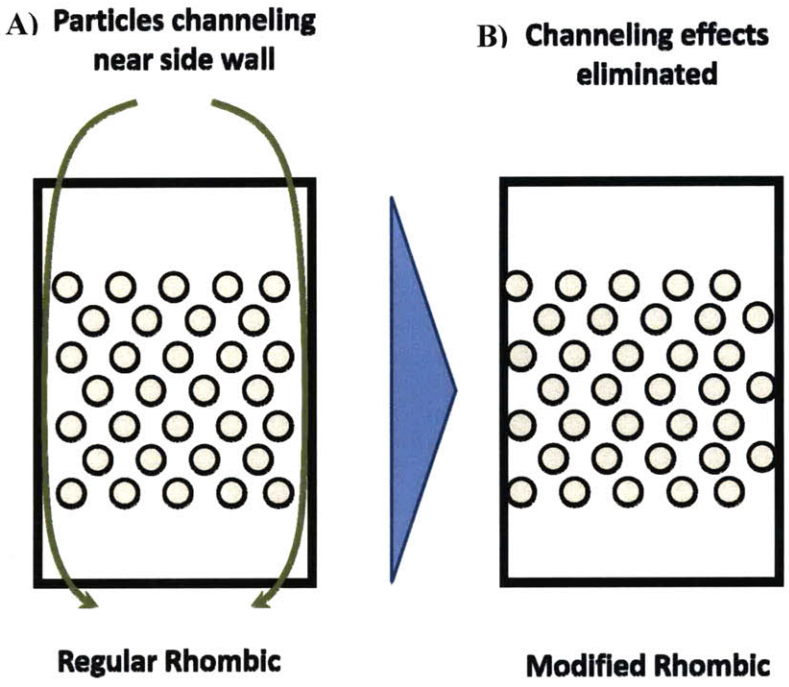

Figure 3-22: Modification of array geometry for quantification experiments

3.4.1.2 Choice of magnetic field direction

A perpendicular magnetic field configuration was chosen for capture quantification experiments (orientation of field perpendicular to flow). This was done due to two reasons. Firstly, a much higher value of magnetic field induction (max. 0.28 T) could be produced in a perpendicular configuration of magnets as compared to a parallel configuration (max. 0.06T). A higher value of magnetic field generates larger magnetic field gradients and thus, stronger magnetic buoyancy forces for capture. The comparison of experimental values of magnetic field generated in parallel and perpendicular orientations are shown in Figure 3-23 below. It can be observed that a perpendicular orientation generates almost five times higher magnetic fields than a parallel orientation.

Secondly, it was also shown that a perpendicular configuration more effective at capture of nonmagnetic particles in chapter 2

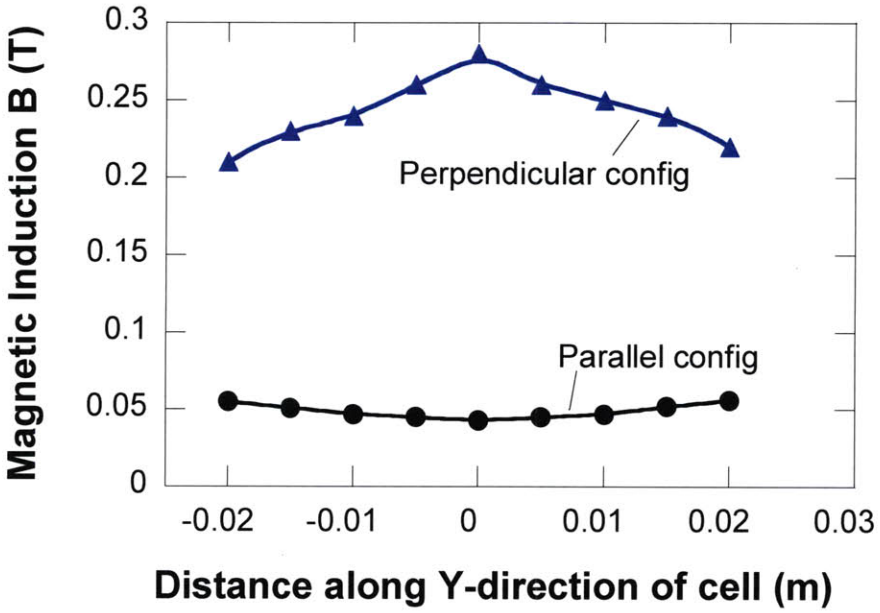

Figure 3-23: Comparison of magnetic field induction for a parallel and perpendicular configuration

3.4.1.3 Choice of operating conditions –

Operating conditions were chosen based on conditions that gave meaningful results for visual capture experiments. Table 3-9 summarizes the values and ranges of operating conditions used in various experiments. Non-magnetic fluorescent particle sizes were chosen on basis of commercial availability. Higher magnetic fields and magnetizations, observed in Table 3-9 as compared to Table 3-2 in the earlier section, are due to a perpendicular magnet configuration. Since the magnetic fields are higher, it is possible to flow the mixture of particles and magnetic fluid at higher velocities through the separation chip. For these experiments, the choice of flow velocities is made such that at the lower end of velocity range (0.0003 m/s), it is possible to obtain significant capture of large particles, while at the higher end of the range, the velocities are large enough that particle trajectory deviations are minimal and hence, no capture is observed. Flow

velocity is directly correlated with throughput, hence, in an ideal separation device, process economics would dictate operating at as high velocities as possible while maintaining the specified separation or capture efficiency.

Table 3-9: Operating parameters for capture quantification experiments

Parameter	Units	Value/Range	Remarks
Velocity of fluid V_0	m/s	0.0003 to 0.0018	Estimates from particle tracking
Fluo. particles Radius	nm	240, 520, 860	Commercially available
Magnetic Field H_0	10^5 A/m	1.67– 2.23	Perpendicular config. results in higher values
Mag. Fluid strength	Wt%	2%	Controlled by synthesis
Fluid Magnetization	A/m	735	From MH Curve
Fluid Viscosity	Pa.s	0.001	Same as water [10]

3.4.2 Experimental Methods

3.4.2.1 Materials

Fluorescently tagged polystyrene beads were purchased from Spherotech Inc. (Lake Forest, IL) and Duke Scientific (Palo Alto, CA). Their particle size, excitation and emission maxima are listed in Table 3-10. The fluorescent dyes have been incorporated into the polymer matrix and hence, the fluorophores do not leach during the course of experiments.

Table 3-10: Particle size, excitation and emission wavelengths for fluorescent particles

Vendor size	Measured size	Excitation maxima	Emission maxima	Company
240 nm	240 nm	590 nm (yellow)	610 nm (orange)	Spherotech Inc.
520 nm	519 nm	530 nm (green)	578 nm (yellow)	Duke Scientific
860 nm	857 nm	530 nm (green)	578 nm (yellow)	Duke Scientific

Particle size was verified for 520 nm and 860 nm particles using scanning electron microscopy (SEM) and the average size was adjusted to be 519 nm and 857 nm respectively. Particle size for 240 nm particles was verified using dynamic light scattering (DLS)[2]. The obtained SEM images are shown in Figure 3-24.

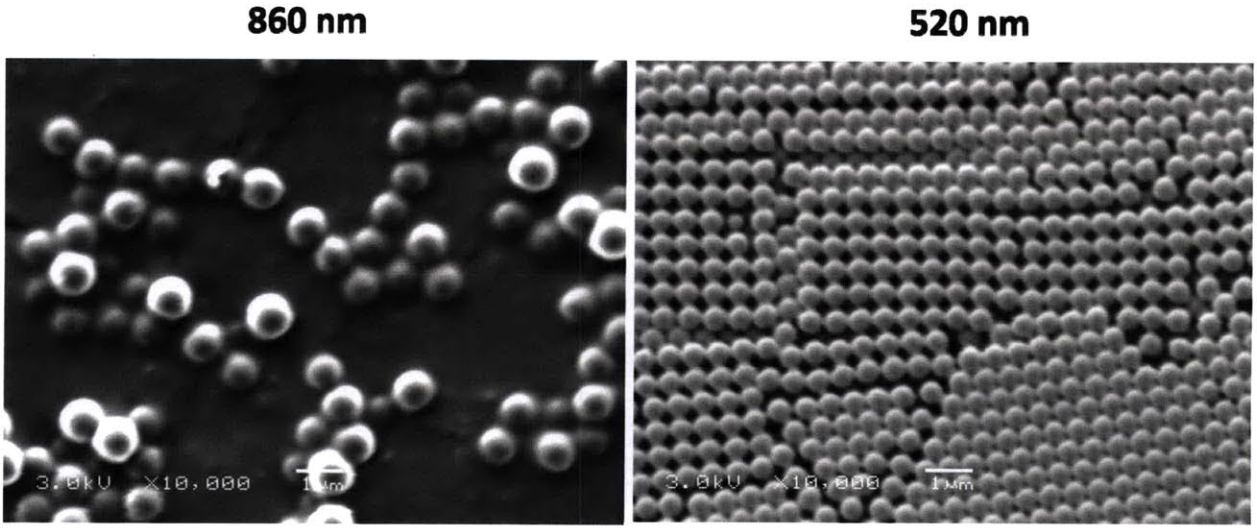

Figure 3-24: SEM images of 860nm and 520 nm fluorescent polystyrene particles

2 wt% magnetic fluid was used as synthesized in previous chapter. Stainless steel pins were embedded in the flow cell to generate the obstacle array. Polyacrylate was used to create a transparent flow cell to generate the appropriate velocity profile to test the particles. De-ionized water was used to flush the flow cell. Neodymium magnets (25x10x5 mm^3) with maximum field at the surface of about 1.3 Tesla, were purchased from Indigo Corporation (Toronto,ON) and joined end to end with poles aligned to increase applied field strength. Soft polyethylene tubing was used for connections. 50 μl syringe (Hamilton Inc, No. 80500) was used to inject fluorescent particles as a controlled pulse into the tubing.

3.4.2.2 Experimental sample preparation

For the purpose of quantification experiments, 2 wt% magnetic fluid, synthesized and purified as explained earlier, was continuously flowed through the separation cell. A 50 micro-liter pulse containing a mixture of fluorescent non-magnetic particles and

magnetic fluid was injected into this stream. The composition of a typical injected pulse shown in Table 3-11 consisted of the fluorescent particles (1% w/v - used as purchased and diluted to 0.08% w/v in the final mixture), and 2 wt% magnetic fluid. The mixture was agitated using a vortex mixer and sonicated for 5 minutes to allow for uniform mixing of components.

Table 3-11: Composition of a typical injection pulse for experiments

Component	Amount	Composition in mixture
Magnetic Fluid 2.17 wt%	0.5 ml	2 wt% MF
Fluorescent particles 1% w/v	44 µl	0.08% w/v
Final Mixture	**0.544** ml	

3.4.2.3 Experimental Set up and method

Pulse chromatography experiments were carried out to quantify the amount of non-magnetic particles captured. A detailed description of construction and operation of the experimental set up is provided below. Schematic of set up is shown in Figure 3-25 and pictures of the set up are attached in Figure 3-26 and Figure 3-27. The set up consists of a transparent poly-acrylate flow cell with an array of cylindrical iron obstacles embedded in a modified rhombic geometry (Fig. through the length of the cell as explained in the design section (Figure 3-22). The flow cell and magnets were held in position using a custom designed holder made of anodized aluminum. The flow cell and holder were both machined at the MIT central machined shop. Pure magnetic fluid (2 wt%) was sent at a constant volumetric flow rate with the help of a syringe pump (Sage M365, Orion Corporation, PA) to maintain a specific flow velocity over the obstacle array. Care was taken to ensure there are no air bubbles inside the array that could distort the flow profile. A mixture of magnetic fluid and fluorescent particles was prepared according to Table 3-11 for injection as a controlled pulse. At t=0, bar magnets were placed in the holder to apply a uniform magnetic field in the perpendicular configuration on the obstacle array. A micro-syringe (Hamilton Inc, No. 80500) was used to inject a controlled pulse of 50 µl

sample mixture into the tubing slightly upstream of entrance of flow cell as shown in Figure 3-26. The fluorescent nonmagnetic particles injected through this pulse would mix into the already flowing magnetic fluid and make their way through the obstacle array. To quantify capture behavior of non-magnetic particles, 20 μl samples were collected for analysis at regular time intervals from the outlet of flow cell. The time interval for sample collection was varied depending on flow rate used. A 20 μl sample was collected from every 36 μl flowing out of the system. This corresponded to one sample per minute for a flow rate of 0.3 mm/s, or one sample per 30s for flow rate of 0.6 mm/s etc. A total of 12 samples was collected while magnets were still in place. Then, the magnets were removed quickly, effectively turning off the magnetic forces and 12 more samples were collected. These collected samples were diluted by 64 times using de-ionized water and sonicated thoroughly for 5 minutes to ensure proper mixing. The fluorescence content of these samples was analyzed using a spectrofluorometer (Photon Technology Inc, Birmingham, NJ). Detailed description of fluorescence analysis is explained in the next section. A control experiment was performed with no applied magnetic field with 12 samples collected in the same manner described as above.

These experiments were carried out for different flow rates and particle sizes. The goal of the experiments was to determine concentration profile as a function of time at the outlet of the flow cell under two states – presence and absence of magnetic field. Concentration profiles could be used to determine fraction of nonmagnetic particles captured on obstacle array vs. fraction escaping even in the presence of magnetic field. Before we discuss the experimental results, we need to discuss the method for determination of concentration of nonmagnetic particles in a magnetic fluid mixture. This is done through a spectrofluorometric analysis which is the topic of the next section.

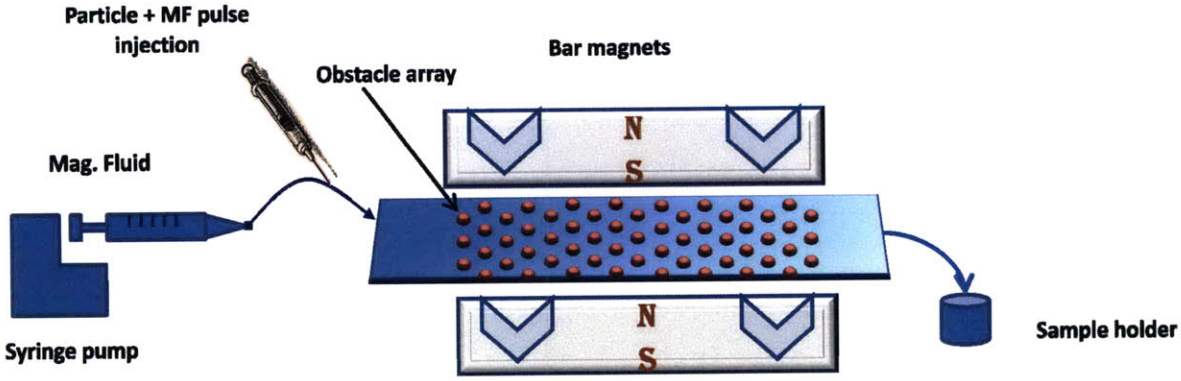

Figure 3-25: Schematic of experimental set up for capture quantification experiments

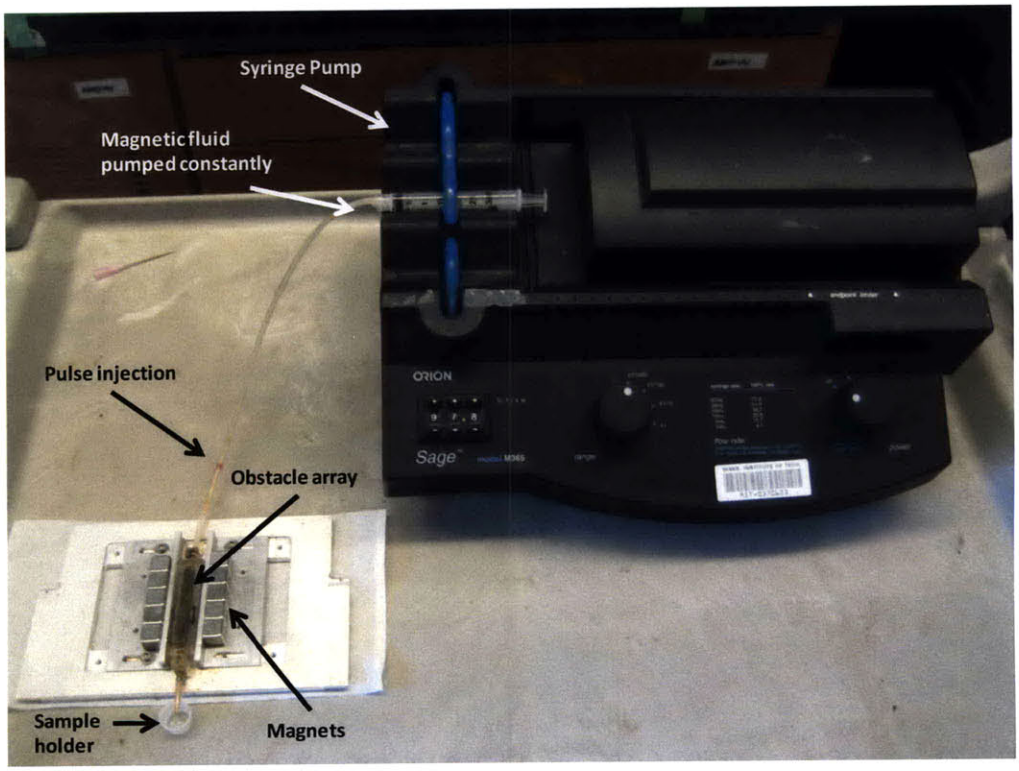

Figure 3-26: Photograph of actual experimental set up

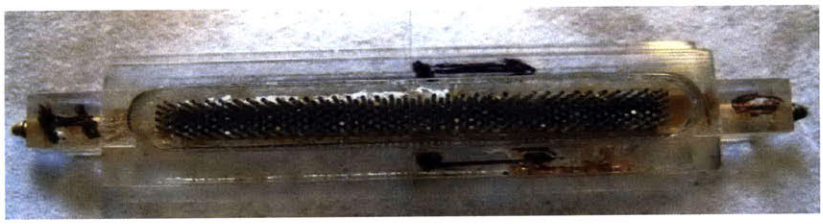

Figure 3-27: Capture flow cell containing cylindrical obstacle array.

3.4.3 Spectrofluorometric analysis of samples for concentration determination

This section deals with developing a method for quantifying the amount of non-magnetic particles in a sample. Fluorescence has been used as a reliable and accurate method for detecting even minute concentrations of non-magnetic particles in previous studies in our research group [1-2, 12]. Other studies in literature dealing with analysis and separation of submicron non-magnetic particles on a microscale have also utilized fluorescence for concentration measurements [13-15]. Hence, we have chosen fluorescence for the quantitative analysis of capture

First, the principles of fluorescence will be discussed and then a concentration determination technique using fluorescence spectroscopy will be explained.

3.4.3.1 Principles of fluorescence

Fluorescence is the phenomenon of emission of visible light by a substance when it is subjected to light of a differing wavelength. Fluorescence is caused by excitement of a paired electron in the fluorophores molecule to an excited state and subsequent return of this electron to the ground state[16]. The timescale for fluorescence is in the order of 10^{-8} seconds which makes it really attractive for analyzing dynamics of extremely fast interactions. Molecules displaying phenomenon of fluorescence, also known as fluorophores, are usually organic compounds which contain delocalized electrons present in conjugated double bonds. The fluorescent particles used in this thesis have been prepared by polymerizing a fluorophore in the presence of styrene and polystyrene core particles. These fluorophores, once incorporated in the particles, do not leach and their fluorescence remains stable for long periods of time[17].

3.4.3.2 Stokes shift and discussion of excitation and emission spectra

The emission wavelength in fluorescence is invariably longer (lower energy) as compared to the exciting wavelength. This phenomenon is known as Stokes Shift and is

observed in fluorescing molecules in a solution phase. Fluorophores can display fluorescence over a small range of wavelengths, though the fluorescence intensity peaks at a particular exciting wavelength. This information is represented through an excitation spectrum for a particular fluorophores. Once excited, the fluorescent molecules emit fluorescence over a range of wavelengths as well (displaced by stokes shift) and this phenomenon can be represented through an emission spectrum. The excitation and emission spectra for particles used in this thesis are shown in Figure 3-28. Fluorescent particles were chosen with fluorescence peaks at different wavelengths.

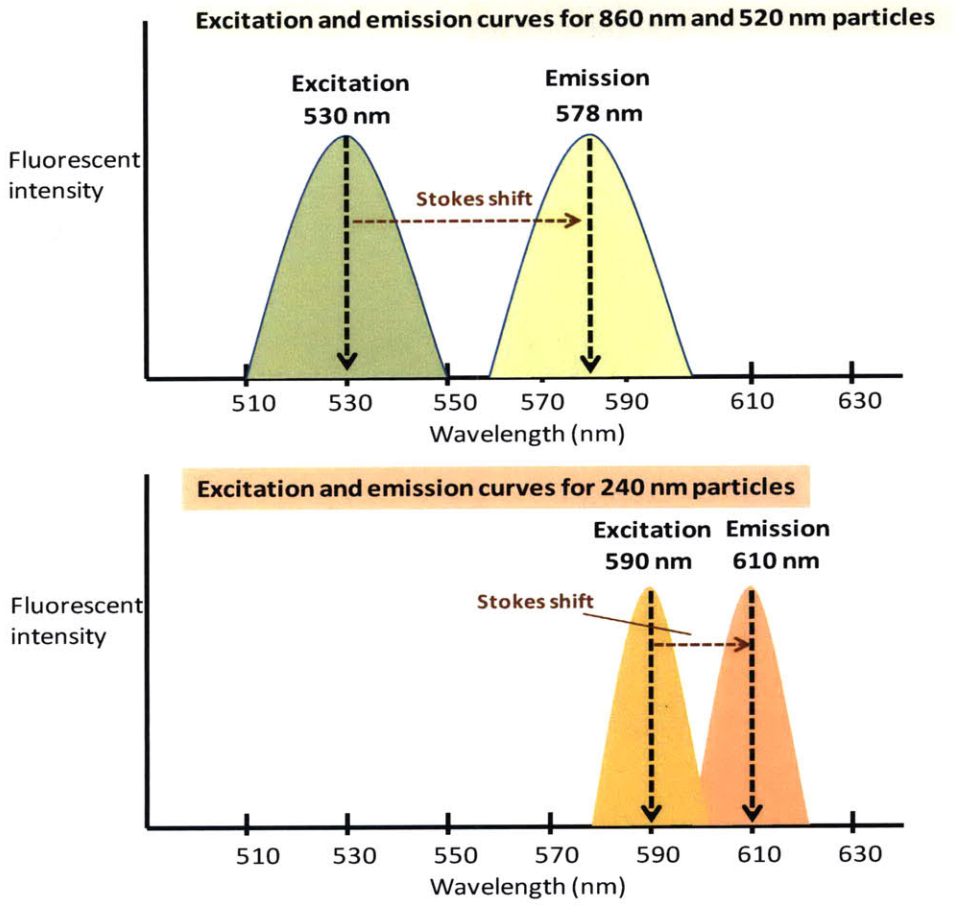

Figure 3-28: Excitation and emission curves for fluorescent polystyrene particles

The particles of size 860 nm and 520 nm could be excited over a range of 510 to 550 nm with an excitation peak of 530 nm. The particles of 240 nm were chosen with an excitation peak at 590 nm and emission peak at 610 nm.

3.4.3.3 Equipment for performing fluorescence spectroscopy

Concentration of particles was determined by calibrating the fluorescent intensity of a sample with concentration as described below. A spectrofluorometer was used to determine the fluorescent intensity in a sample mixture of magnetic fluid and fluorescent particles. The picture of spectrofluorometer used for this thesis is shown in Figure 3-29a with a detailed of sample chamber in Figure 3-29b. The spectrofluorometer contains a xenon lamp which has ability to produce light at all wavelengths between 250 nm and 700 nm. A motorized monochromator located next to the lamp can be adjusted to filter out all unnecessary wavelengths and select the required excitation wavelength. This light beam is then directed onto a sample chamber, containing the sample mixture to be analyzed in a sample holder with specified dimensions. The fluorescence is detected using the motorized emission monochromators which can scan a range of specified excitation wavelengths. The signal is transferred to the photomultiplier tubes to be amplified and the information is transmitted through to a computer. Spectrofluorometer (Quantamaster^{TM} 30, Photon Technology International, Bridgewater NJ) was used for this thesis.

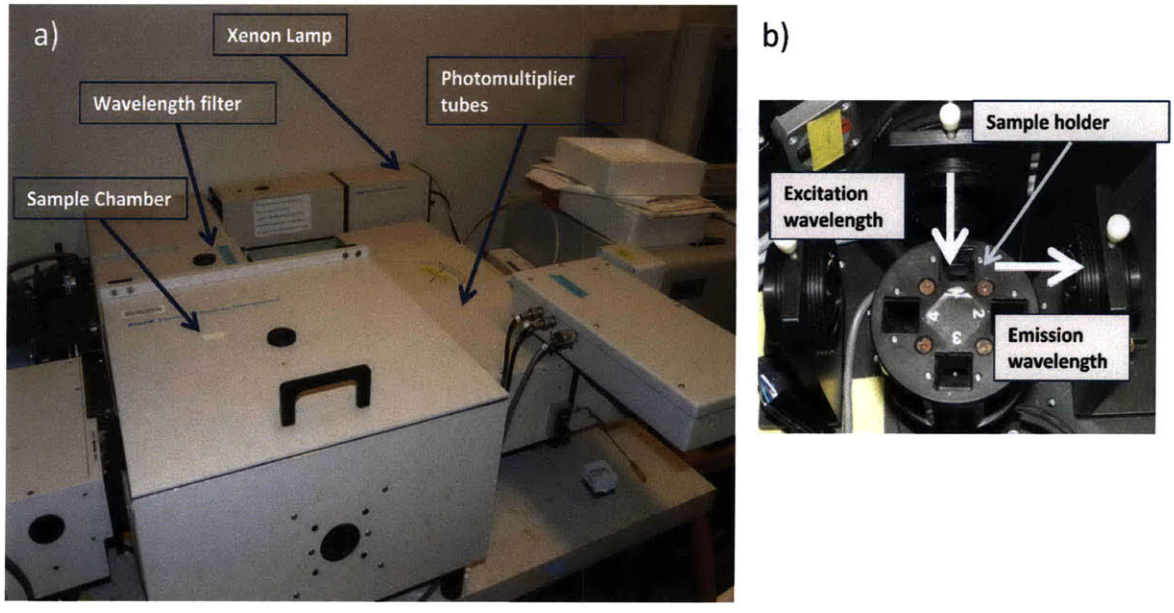

Figure 3-29: Schematic and picture of spectrofluorometer

3.4.3.4 Calibration of concentration

The output from a spectrofluorometer is in the form of an excitation or emission spectrum for a specific sample containing fluorescent particles. For this thesis, the excitation wavelength was chosen corresponding to excitation maxima for the fluorescent particles. Information from the resulting emission spectrum was used to determine concentration of particles. For capture quantification experiments, fluorescent particle concentration was in the range of 0.08% w/v in a 2 wt% magnetic fluid. Magnetic fluid at 2 wt% is dark brown and opaque to fluorescence with a high degree of scatter. To overcome this issue, fluorescence spectroscopy was carried out on significantly diluted samples. In a previous study, it has been shown that fluorescence signal detection increases exponentially with an decrease in magnetic fluid concentration[2]. It is also known that fluorescence decreases linearly with decrease in fluorescent particle concentration. The overall effect of an exponential increase and linear decrease would be to increase the fluorescence signal. The above logic was used in order to determine an optimal dilution for a mixture of fluorescent particles and magnetic fluid for performing fluorescence spectroscopy.

A serial dilution experiment was performed where a mixture of 2wt% magnetic fluid and 0.05% w/v fluorescent particles mixture (excitation maximum 530 nm) was diluted multiple times. Many samples were prepared, each diluted to half the concentration of previous sample, using deionized water. Thus, samples with dilutions of 2x, 4x, 8x, 16x, 32x, 64x and 128x were prepared. Fluorescence emission spectra were obtained from these samples using a spectrofluorometer by excitation at 530 nm and detecting the fluorescent signal at emission of 578 nm. It was observed that the fluorescent signal increased rapidly on dilution and reached a maximum at 64x dilution before becoming too low for detection. Thus, a 64x dilution resulting in a fixed magnetic fluid concentration of 0.031 wt% was chosen for all further quantifications. The fluorescence emission spectra after a 64x dilution for various fluorescent particle concentrations in (%w/v) are shown in Figure 3-30.

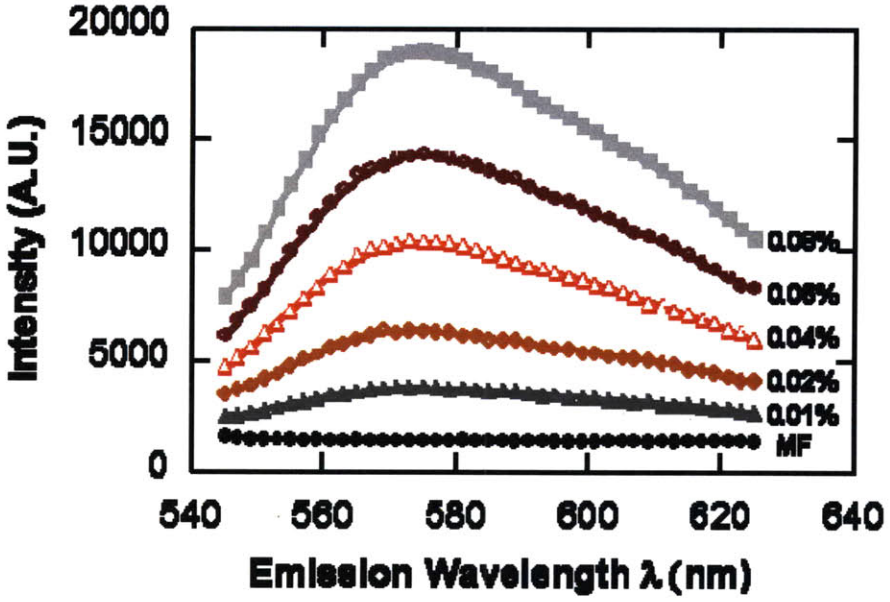

Figure 3-30: Fluorescent spectra obtained for a serial dilution experiment

It can be seen that the pure magnetic fluid emits a low base signal around 1500 units. As the fluorescent particle concentration increases, the height of the peak at 578 nm increases proportional to concentration and reaches a maximum at 0.08% w/v of fluorescent particles (data for 0.1% w/v is not shown in this figure). The information from emission spectra can be analyzed by extracting the emission signal intensity I at 578 nm, subtracting the baseline intensity value of pure magnetic fluid and finally normalizing it against the intensity I_0 at a specific concentration. For this calibration, base concentration for I_0 was chosen at 0.05% w/v of particles. To minimize random error in fluorescence signal detection, an average of 5 intensity measurements was taken for each wavelength. In addition to analyzing the signal at the emission peak (578 nm), two other wavelengths close to the peak (575 nm and 580 nm) were also analyzed. Normalized intensity values I/I_0 were obtained in this way for several fluorescent particle concentrations C_i while keeping the magnetic fluid concentration constant at 0.031 wt% (i.e. a 64x dilution). These normalized intensity ratios were plotted against concentration to obtain the calibration curve relating I/I_0 with C_i which is shown in Figure 3-31. A very strong fit is observed in Figure 3-31 with a high R^2 value which indicates that at low particle concentrations, fluorescence signal from spectrophotometry scales linearly with

concentration. This proves the effectiveness of fluorescence as an accurate method for concentration determination.

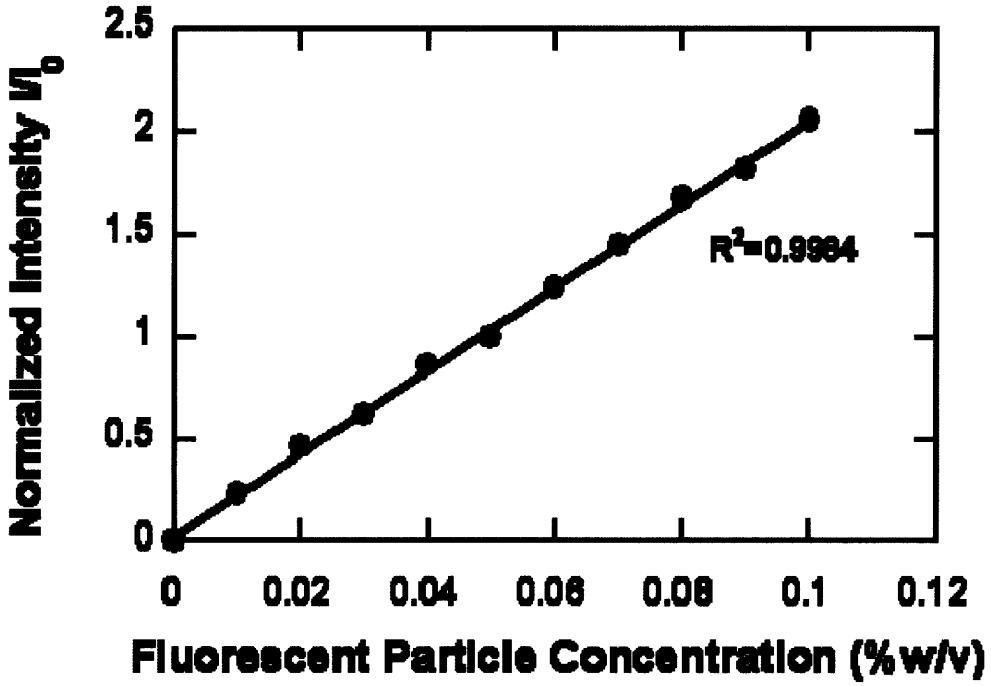

Figure 3-31: Calibration of fluorescent intensity vs. concentration of nonmagnetic particles

3.4.4 Experimental results and discussion

In this section, the results obtained from quantification of capture will be discussed. As described earlier, in a typical experiment, the sample mixture of non-magnetic particles and magnetic fluid was injected into a stream of magnetic fluid passing through the capture device to perform pulse chromatography experiments. After the mixture injection (t=0), twelve data samples were analyzed, first with magnets in place and then twelve more samples were analyzed with magnets removed. This section will first describe the shape of concentration profiles obtained for quantification experiments and the determination of amount of non-magnetic particle capture from these profiles. Later, the discussion will focus on change in amount of capture on varying different experimental variables – non-magnetic particle size R_p, inlet flow velocity V_0, and magnetophoretic

force ratio γ. Finally, results of experiments to separate two non-magnetic particle sizes using the capture device will be discussed.

3.4.4.1 Evolution of nonmagnetic particle concentration profile at outlet with time for a pulse chromatography experiment

Figure 3-32 shows the evolution of concentration profile plotted as a function of sampling intervals for a pulse chromatography experiment. The experiment was performed for 860 nm particles and an inlet flow velocity of 0.0009 m/s. At this velocity, value of magnetophoretic force ratio $\gamma = 0.039$. For this value of γ, we observe significant capture in the separation device as observed in Figure 3-32. Dashed curve shows the concentration profile in the absence of a magnet (control experiment) and resembles the typical bell shaped residence time distribution for a flow channel. The concentration peak is observed at the mean residence time of the flow cell. The solid curve shows the concentration profile in the presence of a magnet and can be observed to have two peaks – the first peak corresponds to particles which breakthrough while the magnet is still on. This first peak is similar to that of the control experiment, occurs at the mean residence time of the device albeit with a smaller height. Sufficient sampling time was allowed so the observed concentration essentially drops to zero, before removing the magnet. This allowed all particles which eluded capture to escape the flow cell. Once the magnet was removed, a second concentration peak was observed. This peak corresponds to the non-magnetic particles that were permanently captured in the device when the magnet was 'on'. Since these curves are analogous to residence time distribution for particles injected into the cell, the area under the curve is proportional to the total amount of particles. The total area is approximately equal between the control experiment and capture experiment and any minor differences can be attributed to inaccuracies of injection volume using a micro-syringe. From figures such as Figure 3-32, it is possible to calculate the amount of particles captured vs. the amount escaped for any particular experiment and compare these to the total amount of particles injected. The amount of particles captured is proportional to the area under the curve of eluted particles (peak after the magnet is removed). The ratio of this area with the total area gives percent capture of particles for

any specific experiment. For this particular experiment, it was found that 48% of 860 nm particles injected were captured by the separation device at a velocity of 0.00045 m/s. Pulse chromatography experiments such as these were performed over a series of particle sizes and inlet flow velocities to determine the effect of these variables on amount of capture. The next section will present results describing the effect of varying inlet flow velocities.

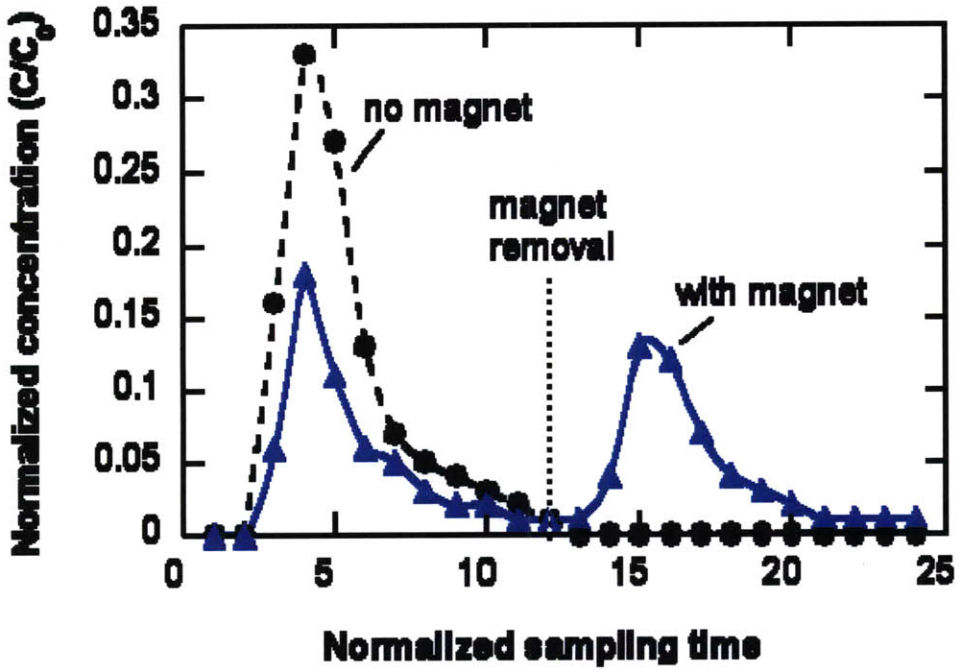

Figure 3-32: Concentration profile at the outlet of separation device for a pulse chromatography experiment with 860 nm particles. Dashed curve represents the no-magnet case and solid curve represents the case when magnet is present.

3.4.4.2 Effect of varying inlet flow velocity on capture

Pulse chromatography experiments were performed for 860 nm fluorescent particles over a range of inlet velocities. Each experiment was repeated a minimum of three times to ensure reproducibility. Figure 3-33 shows concentration profiles plotted as a function of sample intervals for different flow velocities. The sample intervals were chosen to be proportional to residence time of particles in the device. Thus, sampling was at more

frequent intervals for higher velocities and at less frequent intervals for lower velocities. The curves seen in Figure 3-33 are similar to Figure 3-32 in the previous section. The dashed line indicates the outlet concentration profile when magnetic field is absent. This curve shows particles breaking through around the residence time of the device with some axial dispersion and/or channeling. The solid curves represent concentration profiles with magnetic field 'on' for different velocities. For the highest value of velocity at which experiments were carried out (V_0 = 0.0018 m/s), the solid curve closely resembles the no-magnet case. Here, most nonmagnetic particles escape the capture device even in the presence of magnet. A significantly smaller second peak of captured particles can still be seen in the eluate after the magnet is removed indicating that a small fraction of particles were trapped in the device even at this velocity. It can be observed from Figure 3-33, that as the inlet velocity is decreased, the amount of capture increases steadily, and consequently the amount of particles escaping decreases steadily. The first peak becomes progressively smaller and the second peak becomes progressively larger. This experiment shows the effect of inlet velocity on amount of particle capture quantitatively. A similar trend was observed visually in capture visualization experiments described in the previous section. The information in Figure 3-33 can be translated into capture efficiency of the separation device (θ) and plotted against the inlet flow velocity (V_0). Figure 3-34 shows the results of this analysis. It can be seen that at the highest velocity of 0.0018 m/s, capture efficiency is only 25%. As the flow velocity decreases, capture efficiency increases steadily, before saturating around 60%. As explained earlier in this chapter, capture of particles is determined predominantly by the interplay between the hydrodynamic drag and magnetophoretic force on the particles. At a high value of velocity, hydrodynamic drag dominates and most particles follow fluid streamline closely and escape capture. However, as velocity decreases, magnetophoretic force becomes stronger significant, resulting in greater deviations in particle trajectories and hence, the particles are focused in magnetic field minima. This interplay can also be shown by plotting capture efficiency as a function of magnetophoretic force ratio γ. As velocity decreases, γ increases since it is inversely proportional to V_0. We observe that as γ increases, the θ increases as seen in Figure 3-35. The shape of curve in Figure 3-35 also agrees with that predicted by the simulation model – a sharp rise in capture efficiency is

predicted with increase in γ followed by saturation. The results seem to show qualitative agreement with capture model. Comparison between theoretical and experimental results will be performed later in this chapter. The next section will describe results from experiments studying the effect of particle size on capture efficiency.

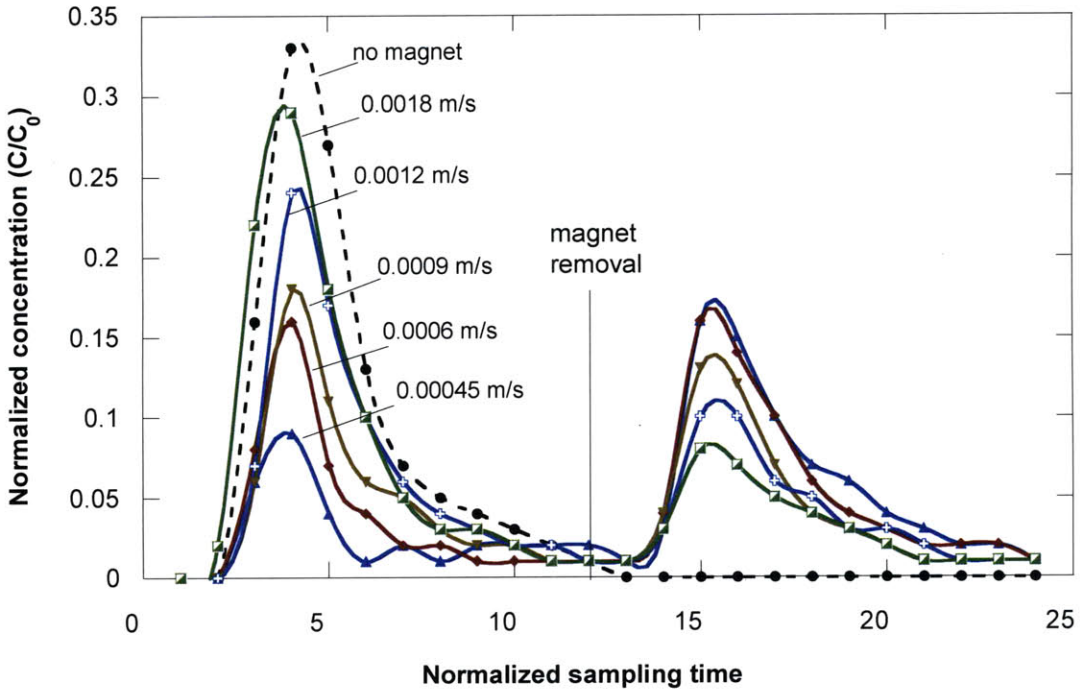

Figure 3-33: Effect of varying particle size on concentration flow profile through the capture cell

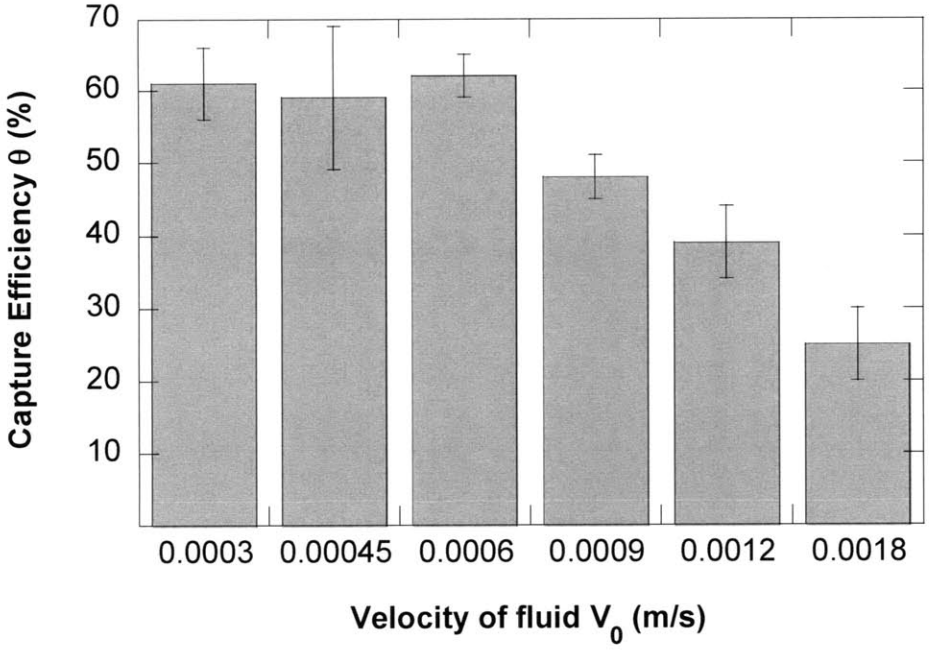

Figure 3-34: Percent of 860 nm particles captured in pulse chromatography experiments performed at different inlet velocities

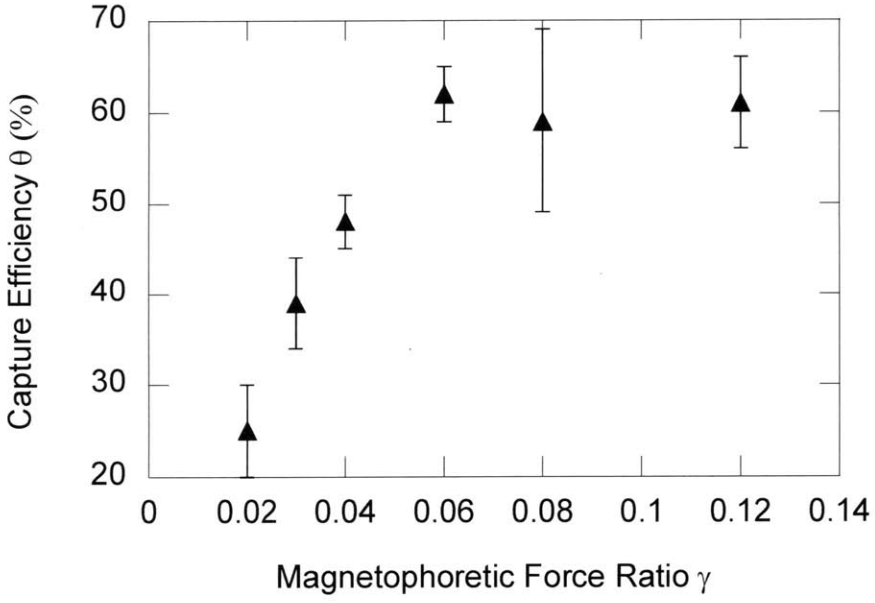

Figure 3-35: Capture efficiency as function of MFR γ for 860 nm particles.

3.4.4.3 Effect of particle size on capture

One of the key characteristics for a particles separation system is differential capture based on particle size. To understand the how capture behavior varies with particle size for this separation device, pulse chromatography experiments were carried out for three different particle sizes – 860 nm, 520 nm and 240 nm. These experiments were performed over for six different inlet velocities and the concentration profiles at the outlet of device were determined. This information was converted into capture efficiency (as described earlier) and plotted vs. inlet flow velocity, which is shown in Figure 3-36. Two trends can be observed from this figure. First, as flow velocity increases, capture efficiency decreases for all particle sizes. This result is consistent with observations from previous section, and holds true for all particle sizes. Second, for each specific inlet flow velocity, larger particles display higher capture efficiency i.e., at a specific inlet flow velocity, when magnet is switched on, 860 nm particles have the most tendency to be captured by magnetophoretic forces, followed by 520 nm particles, and finally by 240 nm particles. This result quantitatively corroborates the observations from capture visualization experiments, where larger particles displayed higher buildup coverage over the obstacle array as compared to smaller particles. Thus, larger particles experience a higher capture force since magnetophoretic migration velocity is proportional to R_p^2. This is an important observation for a separation device. The observed preferential affinity for larger particles as compared to smaller particles proves that the chromatographic separation system works in principle. While designing a separation system, plots such as Figure 3-36 would be helpful in optimizing separation resolution for particle sizes under consideration by choosing the right inlet flow velocity. In order to generalize the applicability of these plots, and to understand the system behavior for a generic choice of operating parameters (i.e. inlet velocity V_0, particle size R_p and magnetic field H_0) capture efficiency (θ) can be plotted as function of magnetophoretic force ratio γ. The results of θ vs. γ are shown in Figure 3-37. It can be observed that value of θ increases sharply with an increase in γ for all three particle sizes which is in qualitative agreement with the model. However, it can also be observed that smaller particles get captured much more readily as compared to larger particles for the same value of γ. According to the

particle trajectory model, the various data points should collapse onto a single curve and for a fixed value of γ, capture efficiency θ should collapse onto a single curve. However, the experimental results differ from the model, and show a more ready capture of smaller particle size. For a separation system, this phenomenon would negatively affect the capture resolution and merits further investigation. Some hypotheses for discrepancies between predicted and actual experimental results are outlined later in this chapter. The next section describes results from separation experiments for a mixture of 860 nm and 240 nm particles.

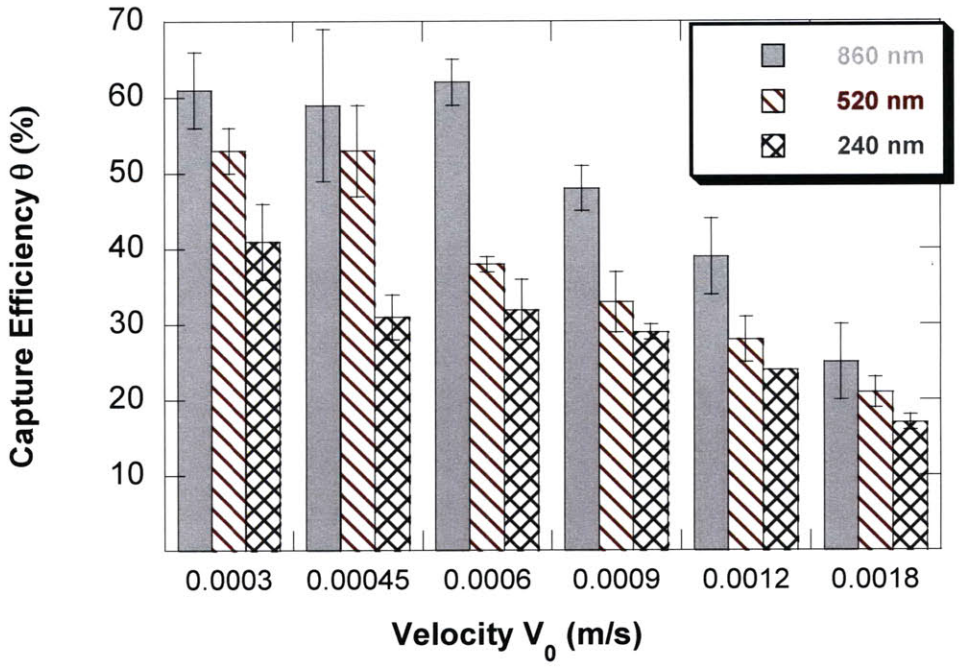

Figure 3-36: Plot of capture efficiency as a function of inlet flow velocity for three different particle sizes.

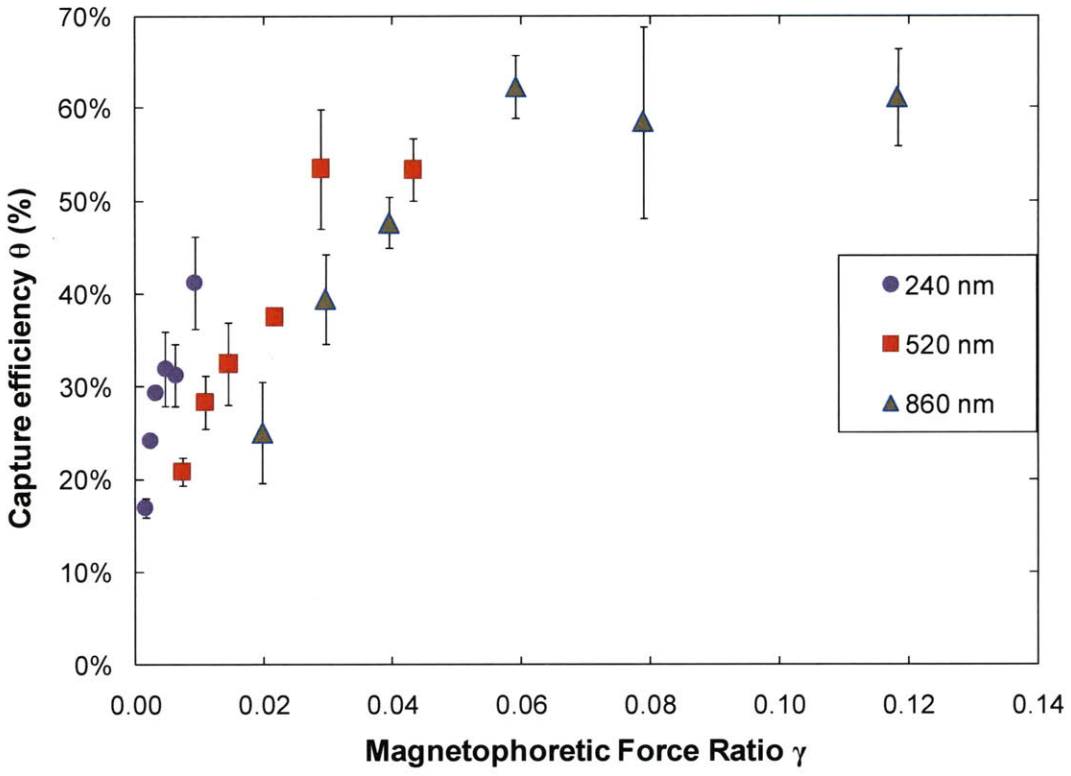

Figure 3-37: Plot of capture efficiency as a function of γ for the separation device for three different particle sizes

3.4.5 Demonstration of separation of a mixture of 860 nm and 240 nm particles

This section will describe the results from a proof of principle experiment performed to demonstrate the ability of the separation system to separate a mixture of two different particle sizes. A pulse chromatography was performed with an inlet flow velocity of 0.0006 m/s using the same procedure as described for quantification experiments. However, the sample pulse contained a mixture of 860 nm and 240 nm particles in equal concentration for the injected pulse. The composition of prepared sample for injection is described in Table 3-12.

Table 3-12: Composition of injection pulse mixture for separation experiment

Component	Composition of component	Amount	Composition final mixture
Magnetic Fluid	2.17 wt%	0.5 ml	2 wt% MF
860 nm Fluo. particles	1% w/v	22 µl	0.04% w/v
240 nm Fluo. particles	1% w/v	22 µl	0.04% w/v
Final Mixture		**0.544 ml**	

To understand the effect of presence of magnet on two particle sizes, a control experiment was performed with no magnetic field. The experiment was repeated with magnetic field turned on for a specific number of samples and then turned off. Concentration profiles at the outlet were analyzed for both cases and are plotted in Figure 3-38. In the absence of a magnet field (control experiment), both 860 nm and 240 nm display essentially a similar concentration profile at the outlet as expected, indicated by the dashed lines. In the presence of a magnet, the behavior is markedly different. 240 nm particles have a larger 'escape peak' and a shorter 'capture peak' as compared to 860 nm particles. In essence, 240 nm particles escape more easily as compared to 840 nm particles while the magnet is on. Thus, more of 840 nm particles are captured and recovered in the elution peak. The capture efficiencies for both particle sizes were calculated for this experiment and are plotted in Figure 3-39. This figure experimentally demonstrates the separation resolution achieved between 840 nm and 240 nm particles. The feed had equal concentration of 860 nm and 240 nm particles. In the stream escaping when magnet was still in place or 'on' (called the "lean" stream), the average composition of 240 nm particles was 60% as compared to 40% for 860 nm particles. When the magnet is turned 'off', the average composition of the eluted "rich" stream has a much higher composition of 860 nm particles as compared to 240 nm particles (63% vs 37%). One stream is richer in 860 nm particles while the other stream is leaner in the same. So, the separation potential has been quantitatively demonstrated through this experiment. This experiment also corroborates the observation of preferential capture of larger particles from pulse chromatography experiments. Even, when two non-magnetic

particle sizes are sent as a mixture through the separation device, the affinity for larger particle size is retained by the device. The separation resolution achieved by this experiment has significant potential to be improved and can be further optimized by varying the inlet velocity and magnetic field strength. In addition, the throughput of the device can be increased by using a higher channel cross section and additional obstacle arrays for the system.

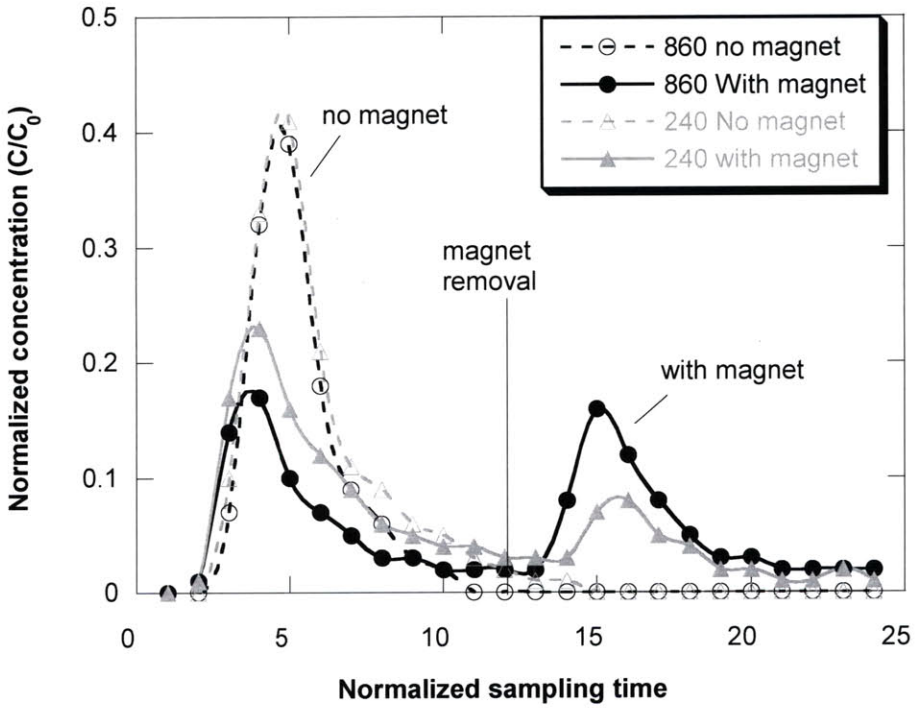

Figure 3-38: Concentration profile at the outlet of separation device for separation of 860 vs. 240 nm particles

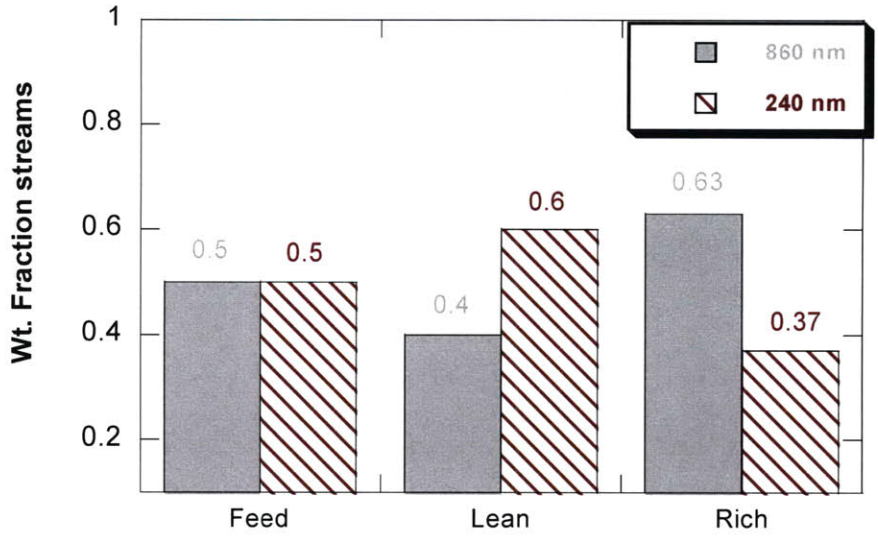

Figure 3-39: Average concentrations of 860 nm and 240 nm particles in streams collected with magnet 'on' and 'off'

3.4.6 Summary of quantitative study of magnetophoretic capture

In this section, results from pulse chromatography experiments to quantitatively demonstrate capture of non-magnetic particles were discussed. These results verified observations from visualization experiments discussed in the previous section. A pulse of fluorescent non-magnetic particles was injected into the capture/separation device and concentration at the outlet was monitored. In the absence of a magnetic field, a typical broadening of injection peak was observed, with some axial dispersion. However, when a magnetic field was applied for a short duration and then switched off, two concentration peaks were observed. The first peak represented particles escaping capture in the device and the second peak (after magnetic field was turned off) represented the elution peak of captured particles.

Through these pulse chromatography experiments, capture efficiency of the device was determined over a range of operating conditions and the results obtained validated qualitative observations from capture visualization experiments. The particle trajectory model for capture was verified by determining the effect of magnetophoretic ratio γ on

capture efficiency. This was done through experimentally varying parameters such as incident flow velocity V_0 and particle size R_p. The experiments showed that as flow velocity V_0 was increased, the height of escape peak relative to capture peak increased, representing a decrease in capture efficiency. The inverse dependence of capture efficiency on V_0 was proved in this way. It was also observed that separation efficiency increases sharply with γ and saturates at around 60% high values of γ (for 860 nm particles). The shape of capture efficiency vs. γ plot qualitatively agreed with simulation results.

It was also shown that at a specific V_0, larger particles were preferentially captured over smaller particles. This observation quantitatively proved the feasibility of separating a mixture of particles based on their size. To further demonstrate the capability of the device to perform size based separations, proof of principle separation experiments were carried out for a mixture of particle sizes. It was shown that larger particles could be preferentially trapped in the device and thus, two batches of liquid could be obtained – one rich and the other lean in large particles. Hence, it was demonstrated that magnetic buoyancy forces, generated through magnetic field gradients in the presence of a magnetic environment, were useful in separating non-magnetic particles based on size.

A significant observation from these experiments was that higher capture efficiency could be obtained for a smaller particle sizes, at a constant value of γ. These findings are not explained by the particle trajectory model. However, the deviations are consistent with qualitative observations from capture visualization experiments as well. The next section which compares experimental capture efficiency with predictions from 3D simulations performed for the experimental set up. Some reasons for deviation between simulations and experiments will also be outlined.

3.5 Particle trajectory simulations for predicting capture efficiency for the experimental set-up

This section describes the three dimensional (3D) particle trajectory simulations performed for the experimental set up to compare the capture quantification results obtained experimentally with predictions from simulation. In the particle trajectory simulations described in the previous chapter and earlier in this chapter, only x and y dimensions were considered. The inherent assumption was that the gradients in z-direction are insignificant. While this might hold true for magnetic fields (due to very long obstacles), the finite height of the flow cell makes consideration of z-direction important for completely describing the flow field. 3D simulations take into account the variation of both magnetic and flow fields in the z-direction. The particle trajectories thus obtained are truly three dimensional with particle motion described in x, y and z directions. The vector equation used for determining 3D particle trajectories remains equation (2.44) as before,

$$\underline{r}'_{p,i+1} - \underline{r}'_{p,i} \approx \left(\underline{v}' - \gamma \underline{\nabla}' H'\right)_i \Delta t_i' \tag{2.44}$$

However, since $\underline{r}_p$ now contains the x, y and z components, the velocity field $\underline{v}$ and the magnetic field gradient $\underline{\nabla H}$ need to be determined in 3D. This makes the entire process computationally intensive and requires the use of significant processing power as well as computer memory. In order to obtain results from simulation that closely mimic experiments, it is necessary to capture the variations in z-dimension. The time step used for integrating equation (2.44), can be written analogous to equation (2.45) as,

$$\Delta t_i' = \frac{\Delta t_0' V_0'}{\sqrt{\left(v_x' - \gamma \frac{\partial H'}{\partial x'}\right)_i^2 + \left(v_y' - \gamma \frac{\partial H'}{\partial y'}\right)_i^2 + \left(v_z' - \gamma \frac{\partial H'}{\partial z'}\right)_i^2}} \tag{3.3}$$

where v'_x is the x-component of dimensionless velocity etc, H' is the dimensionless magnetic field, Δt_0 is the initial chosen time step and V'_0 is the dimensionless velocity.

3.5.1 3D magnetic and flow field profiles for the set up

Simulations were performed for the experimental set up used for capture quantification experiments. Taking the computational intensity of the set up under consideration, only 13 rows of obstacles were considered as compared to 65 in the actual separation cell. This assumption should not affect the results from simulation in any significant way since most of the capture is expected to occur over the first few rows of wires (as observed in results of 2D trajectory simulations). Figure 3-40 shows a typical flow field profile and Figure 3-41 shows a typical magnetic field profile for the experimental set up.

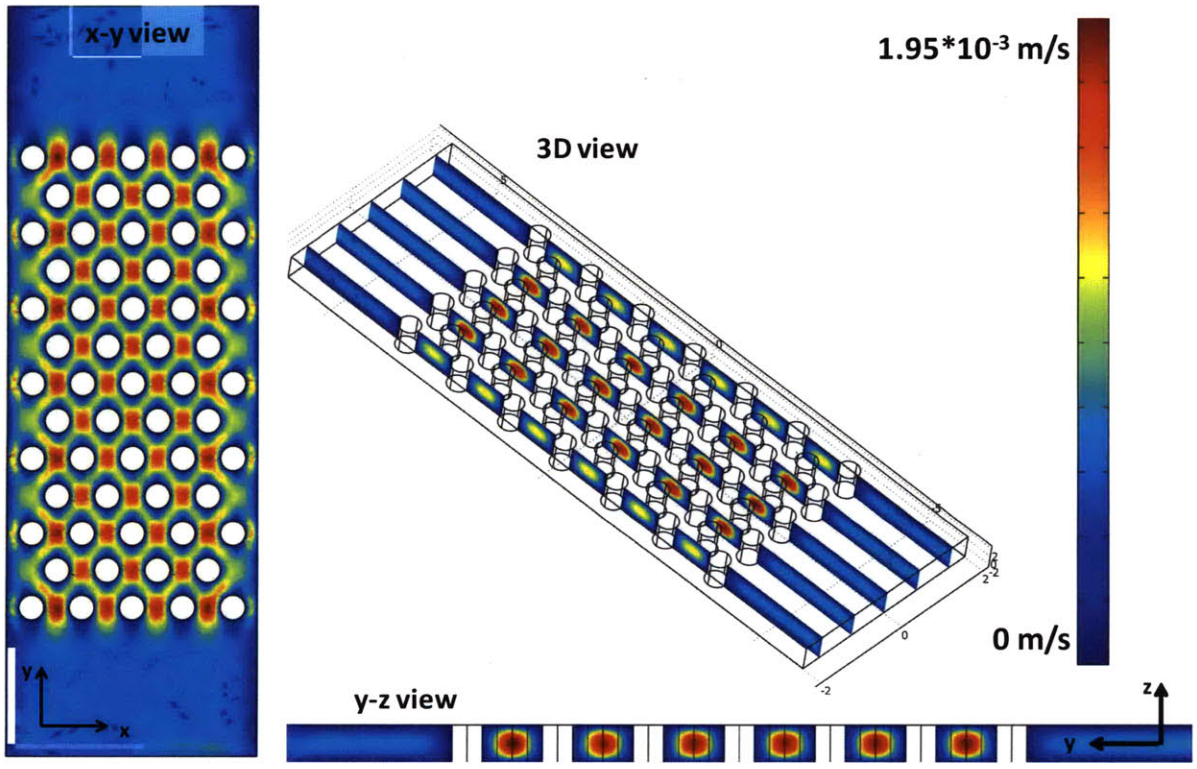

Figure 3-40: Typical 3D flow field profile for the experimental set up

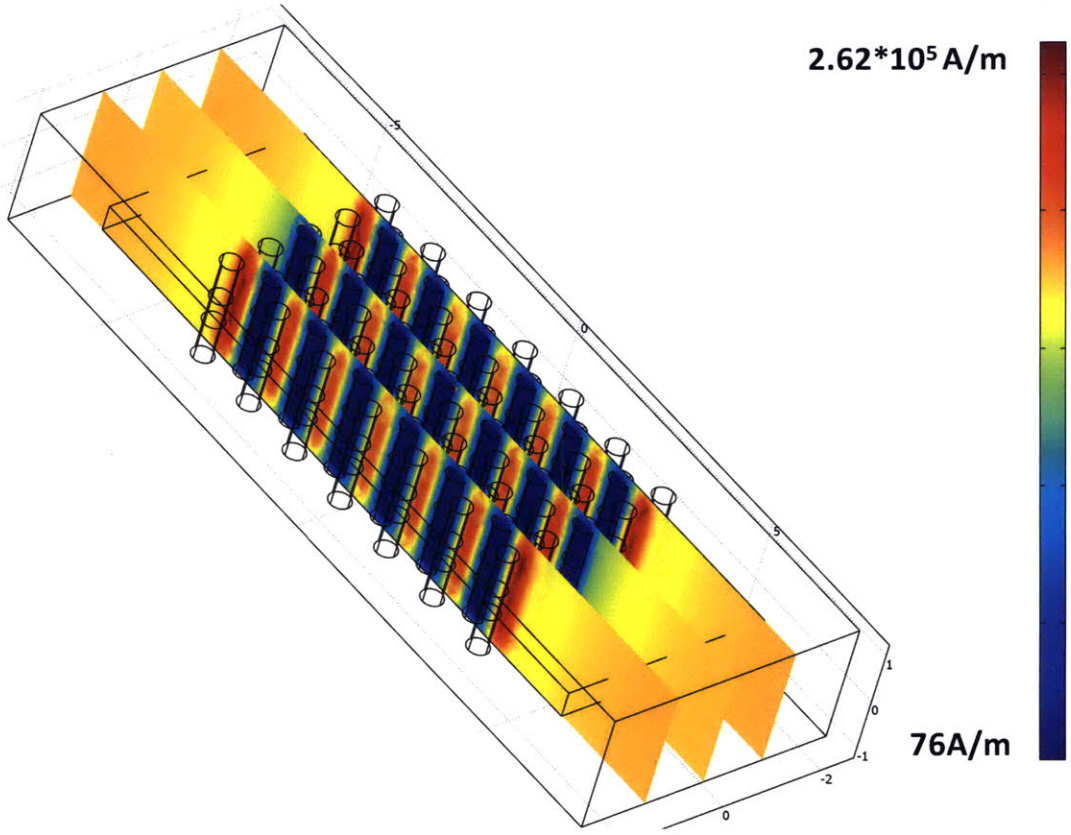

Figure 3-41: Typical 3D magnetic field profile for the experimental set up

From the flow profile, we can observe that in addition to the fluid accelerating between obstacles as in the 2D case, the flow also shows a parabolic profile in the z direction due to the thin walls of the separation cell. In Figure 3-41, the magnetic field however retains its characteristics as in the 2D case. Since the obstacle cylinders are long in the z-direction as compared to the flow cell height there are negligible gradients in the z-direction.

3.5.2 3D particle trajectories for the experimental set up

Using the magnetic and flow field profiles shown as above, particle trajectories were calculated in 3D for the experimental setup. These trajectories were found to depend on the values of γ alone. Below in Figure 3-42, 3-43 and 3-44 are shown particle trajectories for three different values of γ.

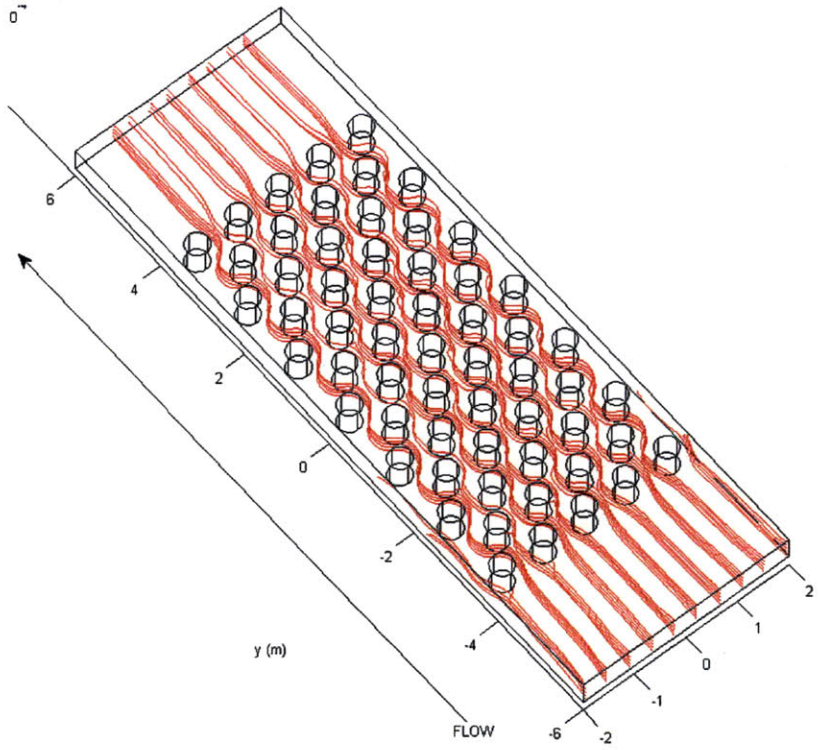

Figure 3-42: 3D particle trajectories for $\gamma = 0.1$

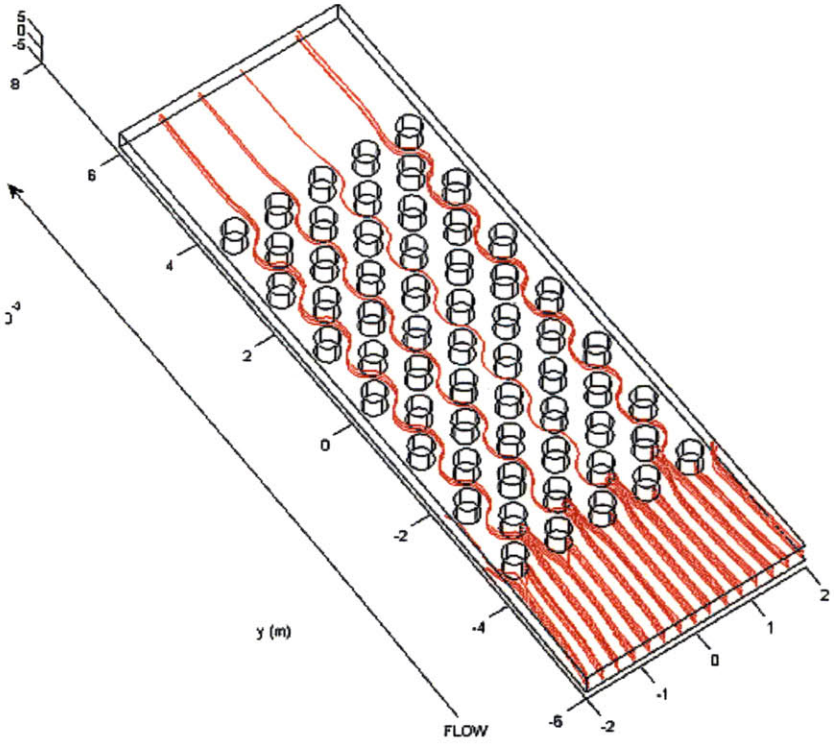

Figure 3-43: 3D particle trajectories for $\gamma = 0.15$

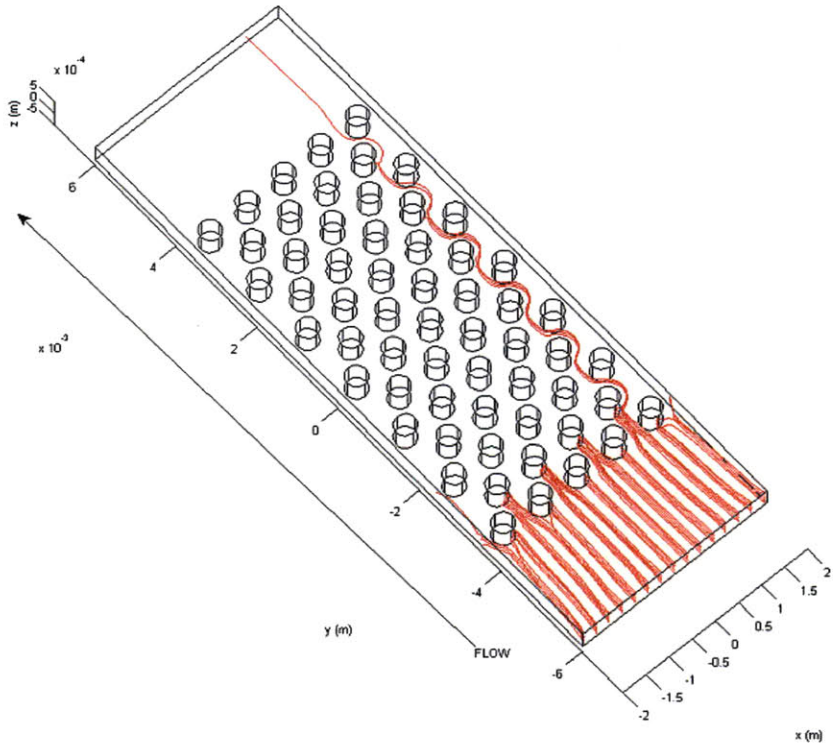

Figure 3-44: 3D particle trajectories for $\gamma = 0.2$

In order to compare the capture efficiency θ predicted by simulation with experimentally obtained results, curves of θ vs. γ were generated as shown in Figure 3-45. In the particle trajectories shown, we can observe that some particles get trapped on the wires whereas some others are deflected onto the walls of the device. For calculating θ, it is assumed that only particles deflected onto the wires are captured, while the particle deflected to the walls escape the obstacle course. Based on this assumption, the maximum capture predicted by simulations is 95%. When curves of θ vs. γ were generated for three different particle sizes (860 nm, 520 nm and 240 nm), they were found to coincide exactly showing that the magnetophoretic ratio γ is the only variable that determines capture.

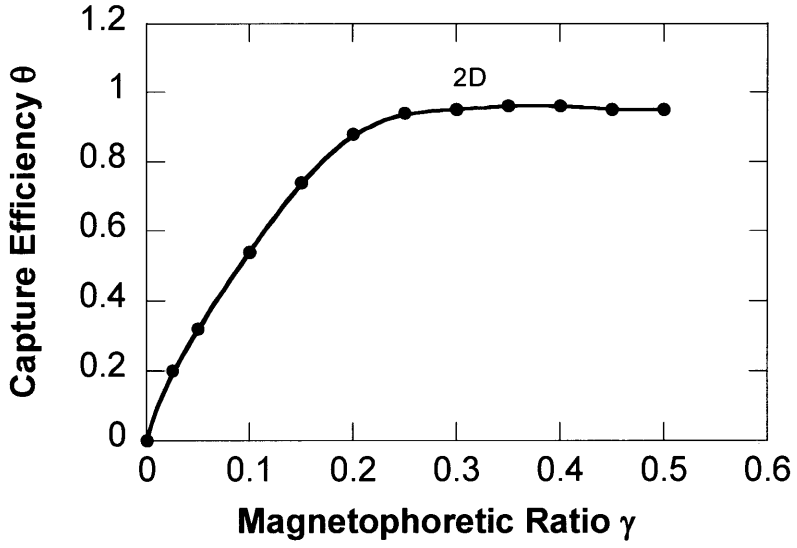

Figure 3-45: Plot of capture efficiency θ vs. magnetophoretic force ratio γ for the experimental setup

3.5.3 Comparison of capture efficiencies between simulations and experiments

The predicted value of capture efficiencies from simulation were compared with θ obtained experimentally. This comparison is shown in Figure 3-46. It can be observed from the figure that the experimental θ values rise sharply with γ, as is predicted by simulation. However, the simulation highly under predicts the amount of capture. Thus, the same amount of capture occurs at a much lower value of γ than that predicted by simulation. Also, it is observed that simulations predict the θ vs γ curve to be exactly the same regardless of particle size. In reality, however, smaller particles tend to get captured at a much smaller value of γ than larger particle sizes.

The other big difference between the experimental and simulation results centers on the saturation value of capture. The maximum capture efficiency obtained experimentally was around 60% for 860 nm particles as compared to 95% capture predicted by simulations.

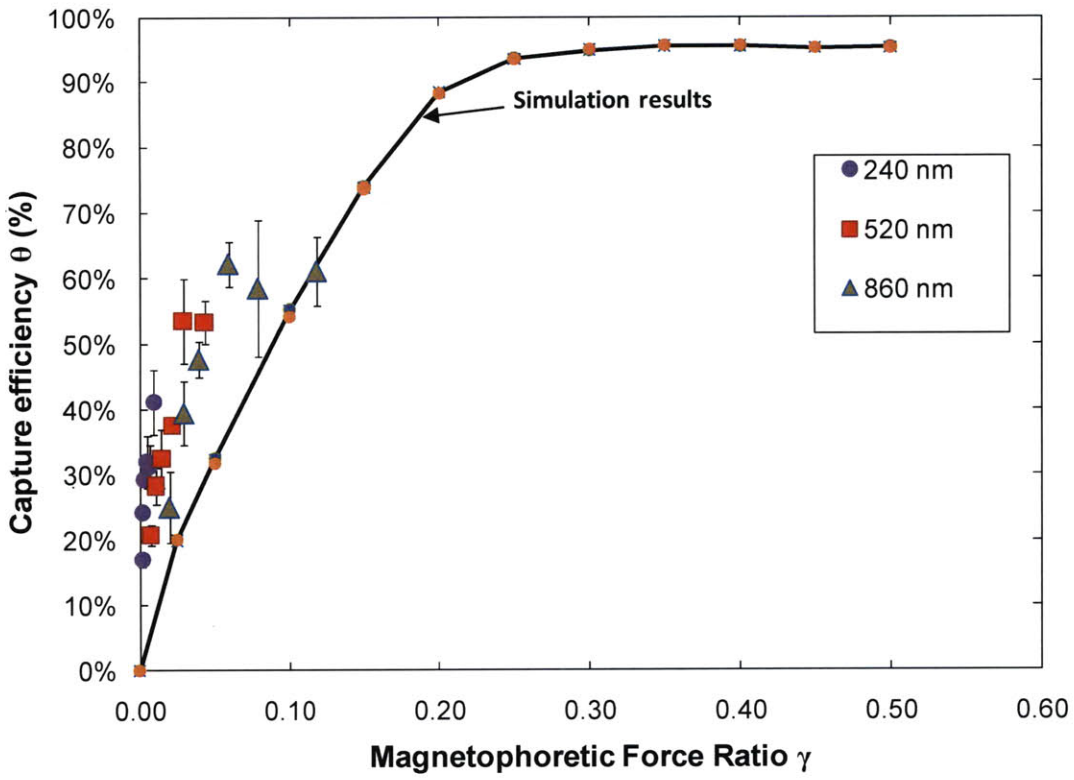

Figure 3-46: Comparison of capture efficiency (θ) vs Magnetophoretic Force Ratio (γ) – Experimental values for three different particle sizes compared to predictions by 3D particle trajectory simulations

3.5.4 Discussion on limitations of the particle trajectory model

The deviation of predicted capture efficiencies from simulations highlights the limitation of the single particle trajectory model in quantitatively determining capture efficiency. The single particle model ignores any interactions involving non-magnetic polystyrene particles. The main assumption is that once a single particle encounters the obstacle boundary, it is assumed to be captured. The interactions of particles with the obstacle are ignored. Since it is a single particle model, buildup on the wires and its effect on capture behavior has not been taken into consideration. Such a study was conducted for magnetic nanoparticle capture on cylindrical iron obstacles by Moeser [18] who showed existence of limits on regions of capture based on drag and diffusion forces on the magnetic

particles. This kind of analysis would be required for non-magnetic particles as well to determine the effect of build up and diffusion limitations on a capture.

In addition, a significant assumption was the lack of interaction between the non-magnetic particles with each other. Skjeltorp [19] showed that non-magnetic particles immersed in a magnetic environment behave like holes with an associated apparent magnetic moment given as,

$$M_v(\theta_p) = -\chi_{eff}(\theta_p)VH(\theta_p) \tag{3.4}$$

Where θ_p is the angle between the field direction and plane in which the non-magnetic particles exist (if particles exist in a planar layer), χ_{eff} is the effective magnetic susceptibility which is a function of θ_p, V is the volume of the particle and H is the applied magnetic field.

Due to this apparent magnetic moment, there are dipolar interactions between the non-magnetic particles which could lead to chain formation between non-magnetic particles. Chen [20] recently showed how considering only individual particles in capture modeling and ignoring particle chaining effects underestimates the effectiveness of separation process for magnetic nanoparticles. This study showed a significant increase in capture efficiency due to chaining of magnetic nanoparticles in high-gradient magnetic separation processes. This could possibly be true for non-magnetic particles in the presence of apparent magnetic dipolar interactions as well.

Another important limitation in the model is ignoring how non-magnetic particles affect the surrounding magnetic particles in the presence of magnetic field gradients. In this present model, the magnetic medium around the non-magnetic particles has been assumed to be a continuum since the non-magnetic particles are much larger than the magnetic particles. However, for smaller non-magnetic particles (D_p = 200 nm), and larger magnetic nano-particles, interactions would start becoming significant. Tejwani [21] recently demonstrated the anisotropies that exist in the magnetization of magnetic nanoparticles when present around a non-magnetic particle. It was shown that the

normalized magnetization of magnetic nanoparticles to be higher in the equatorial regions as compared to the polar regions of the non-magnetic particle.

Finally, in our model, we assume a uniform weighting of particle trajectories entering into the face of the flow cell. However, since the injection is slightly upstream of the device in the form of a pulse, the particle entry distribution must be weighted accordingly. This might be a major limitation in the trajectory model.

All these limitations would need to be addressed in a comprehensive model in order to better describe the capture of non-magnetic particles around inhomogeneous magnetic field gradients.

3.6 Conclusion

In this chapter, we discussed the experimental work performed to demonstrate preferential capture of non-magnetic particles in regions of magnetic field gradients and in the presence of a magnetic environment.

The magnetic environment was created by immersing non-magnetic particles in a magnetic fluid – a stable suspension of magnetite particles in water. Detailed synthesis of this magnetic fluid based on methods developed by Moeser[3] was described in this chapter. Through this synthesis, magnetite particles were stably dispersed in water using a PAA-g-PAA graft copolymer. The average core size was found to 6.7 nm with a number average hydrodynamic diameter of 33nm. Magnetic fluids with a concentrations as high as 3 wt% could be prepared using this method.

Particle trajectory simulations described in the previous chapter were used to design an experimental set up for first visualizing the capture of non-magnetic particles and then quantifying the amount of this capture. The geometric design (e.g. rhombic array and capture cell dimensions) and operating conditions (H_0, V_0) of the experimental set up were determined using these simulations.

Through capture visualization experiments, we were able to visually see evidence of preferential capture of larger sized particles. These experiments showed particles move towards and focus in regions of magnetic field minima. Through these experiments we were also able to qualitatively verify the dependence of capture on the magnetophoretic ratio γ. The results showed that capture of non-magnetic particles occurred either when particle size R_p was increased or the fluid velocity V_0 was decreased.

The qualitative results for capture of non-magnetic particles were further quantified through pulse chromatography experiments. Through these pulse chromatography experiments, capture efficiency (θ) of the device was determined over a range of operating conditions. The results obtained validated qualitative observations from capture visualization experiments. In particular, it was shown that θ rose sharply with γ for all particle sizes, as is predicted by simulation. It was also observed that at the same velocity V_0, larger particle sizes were preferentially captured. Separation experiments were performed for a mixture of 860 nm and 240 nm particles and the separation potential for the capture device was shown.

Three dimensional particle trajectory simulations were performed to determine the capture efficiencies predicted by the Lagrangian particle trajectory model and compare them to experimentally observed values. The experimental results qualitatively matched the θ vs γ trend predicted by simulation, though it was observed that the simulation model significantly under predicted amount of capture. Additionally, the experimentally observed saturation capture efficiency was 60%, whereas simulations predicted saturation capture to be 95%. These limitations of the single particle trajectory model were outlined addressing some of which could reduce the discrepancy between the experimental and predicted capture efficiencies.

3.7 References:

1. Fateen, S.-E.K., *Magnetophoretic focusing on submicron particles dispersed in a polymer-stabilized magnetic fluid.* 2002, Massachusetts Institute of Technology: Cambridge MA.

2. Gonzalez , L., *Negative magnetophoresis of submicron species in magnetic nanofluids*, in *Chemical Engineering*. 2008, MIT: Cambridge MA.

3. Moeser, G.D., et al., *Water-based magnetic fluids as extractants for synthetic organic compounds.* Industrial & Engineering Chemistry Research, 2002. **41**(19): p. 4739-4749.

4. Shen, L.F., P.E. Laibinis, and T.A. Hatton, *Aqueous magnetic fluids stabilized by surfactant bilayers.* Journal of Magnetism and Magnetic Materials, 1999. **194**(1-3): p. 37-44.

5. Bucak, S., et al., *Protein separations using colloidal magnetic nanoparticles.* Biotechnology Progress, 2003. **19**(2): p. 477-484.

6. Rosensweig, R.E., *Ferrohydrodynamics*. 1985, London: Cambridge University Press.

7. Moeser, G.D., *Colloidal Magnetic Fluids as Extractants for Chemical Processing Applications*, in *Chemical engineering*. 2003, MIT: Cambridge MA.

8. Sharpe, S.A. and Massachusetts Institute of Technology. Dept. of Chemical Engineering., *Magnetophoretic cell clarification.* 2004. p. 178 p.

9. Yoe, J.H. and A.L. Jones, *Colorimetric Determination of Iron with Disodium-1,2-dihydroxybenzene-3,5-disulfonate.* Industrial & Engineering Chemistry Analytical Edition, 2002. **16**(2): p. 111-115.

10. Gonzalez L A, S.F., K A Smith, T A Hatton, *Magnetophoresis of Nonmagnetic, Submicrometer Particles in Magnetic Fluids.* SMA Transactions in Molecular Engineering of Biological and Chemical Systems (http://dspace.mit.edu), 2004.

11. Annavarapu, R., *Electronic materials for capture visualization of submicron nonmagnetic particles*. 2009.

12. Park, E.S., et al., *Size-Selective magnetophoretic trapping of submicrometer non-magnetic particles immersed in a magnetic nano-fluid.* in preparation.

13. Takagi, J., et al., *Continuous particle separation in a microchannel having asymmetrically arranged multiple branches.* Lab On A Chip, 2005. **5**(7): p. 778-784.

14. Kang, K.H., et al., *Continuous separation of microparticies by size with direct current-dielectrophoresis.* Electrophoresis, 2006. **27**(3): p. 694-702.

15. van Oudenaarden, A. and S.G. Boxer, *Brownian Ratchets: Molecular Separations in Lipid Bilayers Supported on Patterned Arrays.* Science, 1999. **285**(5430): p. 1046-1048.

16. Lakowicz, J.R., *Principles of Fluorescence Spectroscopy*. 1st, third print ed. 1983, New York and London: Plenum Press.

17. Spherotech, *Technical Manual*, in *www.spherotech.com*. 2009.

18. Moeser, G.D., et al., *High-gradient magnetic separation of coated magnetic nanoparticles.* AICHE Journal, 2004. **50**(11): p. 2835-2848.

19. Skjeltorp, A.T., *One- and Two-Dimensional Crystallization of Magnetic Holes.* Physical Review Letters, 1983. **51**(Copyright (C) 2009 The American Physical Society): p. 2306.

20. Chen, F., *Magnetically Enhanced Centrifugation for Continuous Biopharmaceutical Processing*, in *Chemical Engineering*. 2009, MIT: Cambridge MA.

21. Saurabh, T., *Thermodynamic and Transport Properties of Nonmagnetic Particles in Magnetic Fluids*, in *Chemical Engineering*. 2009, MIT: Cambridge MA.

Chapter 4

Summary, Conclusions and Future Work

4.1 Introduction

A reliable industrial scale separation technology for fine particles in the sub-micron range will have numerous potential applications ranging from biotechnology to electronics. The focus of this thesis was on developing a novel scalable way of separating sub-micrometer nonmagnetic particles based on their size. A combination of simulation and experiments were used to develop and test the potential of a separation system that utilizes size dependent magnetophoresis of non-magnetic particles immersed in a magnetic fluid.

4.2 Summary of research

Nonmagnetic particles that are immersed in a magnetic environment experience magnetic buoyancy forces when subjected magnetic field gradients. These forces scale with the volume of the particle. It is possible to generate magnetic field gradients by applying a uniform magnetic field in a system consisting of structured array of iron obstacles. A mixture of particle sizes immersed in a magnetic fluid can be flown through this obstacle course wherein larger particles would experience stronger interaction with the obstacles and hence get separated in space from smaller particles.

Based on the above principle, a basic force balance on a single non-magnetic particle was performed and a Lagrangian particle trajectory model was developed for this system. Particle trajectory simulations were carried out in order to understand the nature of interaction of non-magnetic particles with iron obstacles. Simulations were performed for a single magnetizable obstacle. It was observed that each obstacle contained regions of both magnetophoretic attraction and repulsion. However, when a mixture of particles was flown through the system, the nature of interaction resulted in the preferential capture of larger nonmagnetic particles. It was observed that the likelihood of capture for a particle

was dependent on the dimensionless ratio of magnetophoretic velocity with fluid velocity, defined as the magnetophoretic velocity ratio γ and the Reynolds number (Re). However, for the range of particle velocities explored in this system, Re <1 and the creeping flow approximation holds, due to which the dimensionless velocity profile does not change significantly on change in Re. Hence the capture behavior predominantly depends on γ. γ was found to be proportional to square of particle radius (R_p^2) and inversely proportional to the particle velocity (V_0). Thus, larger particles experienced greater deviation in trajectories towards the obstacles as compared to smaller particles and were preferentially captured. It was determined that this preferential capture of larger particles from a mixture when flowing through an array of obstacles could form the basis of separation.

Using the above model, particle trajectories were simulated for multiple cylindrical obstacles in different geometric arrangements in order to determine the most effective geometry for separation. Specifically, particle trajectories for linear, square and rhombic geometric arrangements at different wire spacings were simulated. Among the geometries simulated, it was observed that rhombic geometry required the smallest value of γ for complete capture of particles and hence was the most efficient. Capture efficiency (θ) of nonmagnetic particles under various operating conditions was calculated and plots of θ vs. γ were generated.

The separation potential of the system was also experimentally demonstrated. Particle trajectory simulations were carried out to design the geometric and operating parameters of an experimental capture visualization system. Fluorescence microscopy experiments were performed to visualize the capture of nonmagnetic particles on a circular obstacle array. Capture visualization experiments were carried out for 860 nm, 500 nm and 240 nm particles at various flow velocities (various values of γ). These experiments visually showed fluorescent nonmagnetic particles moving towards regions of magnetic field minima around circular iron obstacles and regions of build up formation on the same. It was observed that capture occurred only when γ was large enough on the non-magnetic particles.

These visual observations were further quantified through pulse chromatography experiments. Through these experiments, capture efficiency (θ) of the system was determined over a range of operating conditions. The results obtained validated qualitative observations from earlier capture visualization experiments. In particular, it was shown that θ rose sharply with γ for all particle sizes. Three dimensional (3D) particle trajectory simulations were performed to determine capture efficiency predictions by the Lagrangian particle tracking model and these were compared to experimentally obtained values. Results showed a qualitative match between simulation and experimental results though the simulations significantly under predicted capture efficiency.

Finally, to demonstrate the separation potential of the system, separation experiments were performed for a mixture of 860 nm and 240 nm particles. These experiments successfully demonstrated the ability of the device to preferentially retain the 860 nm particles and hence generate two streams – one rich in a larger particle size and the other rich in a smaller particle size.

Thus, using an approach combining simulations and experiments, a novel separation technology was developed for fractionating submicron nonmagnetic particles by size.

4.3 Future work

There are numerous directions in which the current work can be extended. Some ideas are enumerated below –

1. An obvious direction is to perform the separations on a much larger scale by increasing the throughput of the separation system. This could be done by applying a stronger magnetic field using electromagnets, and increasing the cross section of the separation cell with larger number of obstacles. In addition, stronger magnetic fields would allow separation of smaller nonmagnetic particle sizes.
2. The applied field has been taken to be uniform throughout the system. One could envision a temporal and spatial fluctuation of applied magnetic field such as those

employed in Brownian ratchets [1-2] to enhance separation efficiency. In addition, a combined approach to separation utilizing separation forces exploited in geometric ratchets[1, 3-5], dielectrophoresis [6-7] and magnetic buoyancy forces could be used for separation. Recently, a study utilizing combined forces of magnetophoresis and dielectrophoresis was published which was able to attain increased flexibility in transport of particles on a microchip [8].

3. For the current thesis, a regular array of obstacles was utilized for capturing particles. Since this array is periodic, after a nonmagnetic particle navigates a few rows of obstacles, the other rows become redundant since the particle in essence "sees" similar geometry throughout and escapes the system. One way to address this issue is to incorporate a stochastic array of wires, where obstacles are placed at random through the system. A systematic study of stochastic variation of geometric obstacle arrangement combined with particle trajectory analysis could be carried out in order to evaluate the merit of this idea.
4. Another future direction could be related to the modeling aspects of the thesis. The particle trajectory proposed model in the thesis does not incorporate interparticle interactions between nonmagnetic particles. Recently discrete element modeling was used by Chen [9] to study the behavior of magnetic nanoparticle buildup on a wire array. A similar approach could be envisioned for modeling nonmagnetic particles in the current system. Other approaches to incorporate particle interactions have been taken by Gonzalez [10] and Fateen [11]. A continuum model for describing the behavior of nonmagnetic species immersed in a magnetic fluid developed by Gonzalez [12] could be applied to this system with appropriate boundary conditions to better understand particle dynamics and concentration buildup.
5. Finally, the capture and separations in the current thesis were demonstrated utilizing polystyrene particles. The current system could easily be applied to biological species such as viruses and cellular organelles to demonstrate the efficacy of magnetophoretic separations for bioparticles.

4.4 Bibliography

1. van Oudenaarden, A. and S.G. Boxer, *Brownian Ratchets: Molecular Separations in Lipid Bilayers Supported on Patterned Arrays.* Science, 1999. **285**(5430): p. 1046-1048.

2. Astumian, R.D., *Thermodynamics and Kinetics of a Brownian Motor.* Science, 1997. **276**(5314): p. 917-922.

3. Duke, T.A.J. and R.H. Austin, *Microfabricated sieve for the continuous sorting of macromolecules.* Physical Review Letters, 1998. **80**(7): p. 1552-1555.

4. Huang, L.R., et al., *Continuous particle separation through deterministic lateral displacement.* Science, 2004. **304**(5673): p. 987-990.

5. Chou, C.F., et al., *Sorting by diffusion: An asymmetric obstacle course for continuous molecular separation.* Proceedings Of The National Academy Of Sciences Of The United States Of America, 1999. **96**(24): p. 13762-13765.

6. Kang, K.H., et al., *Continuous separation of microparticies by size with direct current-dielectrophoresis.* Electrophoresis, 2006. **27**(3): p. 694-702.

7. Kralj, J.G., et al., *Continuous dielectrophoretic size-based particle sorting.* Analytical Chemistry, 2006. **78**(14): p. 5019-5025.

8. Liu, C., L. Lagae, and G. Borghs, *Manipulation of magnetic particles on chip by magnetophoretic actuation and dielectrophoretic levitation.* Applied Physics Letters, 2007. **90**(18): p. 184109-3.

9. Chen, F., *Magnetically Enhanced Centrifugation for Continuous Biopharmaceutical Processing*, in *Chemical Engineering*. 2009, MIT: Cambridge MA.

10. Gonzalez , L., *Negative magnetophoresis of submicron species in magnetic nanofluids*, in *Chemical Engineering*. 2008, MIT: Cambridge MA.

11. Fateen, S.-E.K., *Magnetophoretic focusing on submicron particles dispersed in a polymer-stabilized magnetic fluid.* 2002, Massachusetts Institute of Technology: Cambridge MA.

12. Gonzalez L A, S.F., K A Smith, T A Hatton, *Magnetophoresis of Nonmagnetic, Submicrometer Particles in Magnetic Fluids.* SMA Transactions in Molecular Engineering of Biological and Chemical Systems (http://dspace.mit.edu), 2004.

conventional and renewable energy sources. Figure 5-1 shows the world energy demand projections and renewable energy growth projections until 2030.

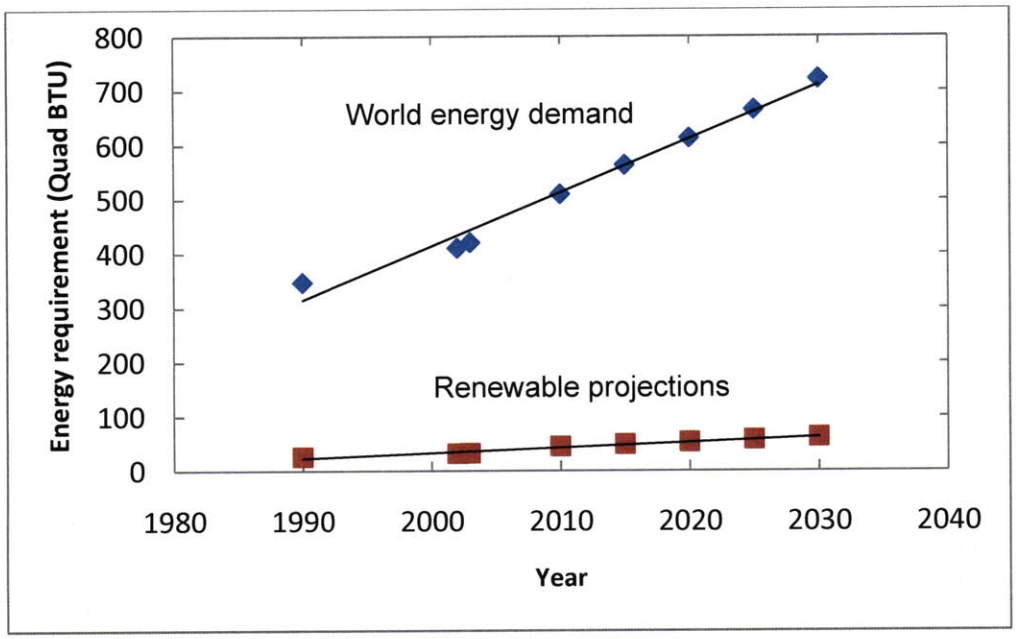

Figure 5-1: Projected world energy demand and renewable energy growth in the next two decades

A significant dependence on conventional energy sources has resulted in a rise in the concentration of carbon dioxide (CO_2) from a stable level of 280 ppm pre-industrial revolution to over 380 ppm in 2006. There is evidence of a strong correlation between rising global average temperatures and concentrations of CO_2 and other greenhouse gases[1]. Figure 5-2 shows the levels of CO2 in the atmosphere in the past 100 years along with a plot of global average temperatures from the Mauna Loa observatory [2-3]. There is evidence of a strong correlation between an increase in the average concentration of CO2 and an anomaly in the global average temperature. IPCC forecasts that in the business as usual scenario, i.e. in the absence of any measures to control green house gas (GHG) emissions or to stabilize the concentration of CO_2, global average temperature will continue to rise anywhere between 0.3 to 0.6 ^{0}C per decade [1]. Such a rise in temperature is predicted to set in place a series of self-reinforcing, irreversible, catastrophic changes in the earth's climate. There is a thus, a great sense of urgency among policy makers, at least in the developed world, to institute tight measures to

reduce GHG emissions. The Copenhagen accord in 2009 received commitments from both developed and developing countries to reduce GHG emissions measured through various metrics[4].

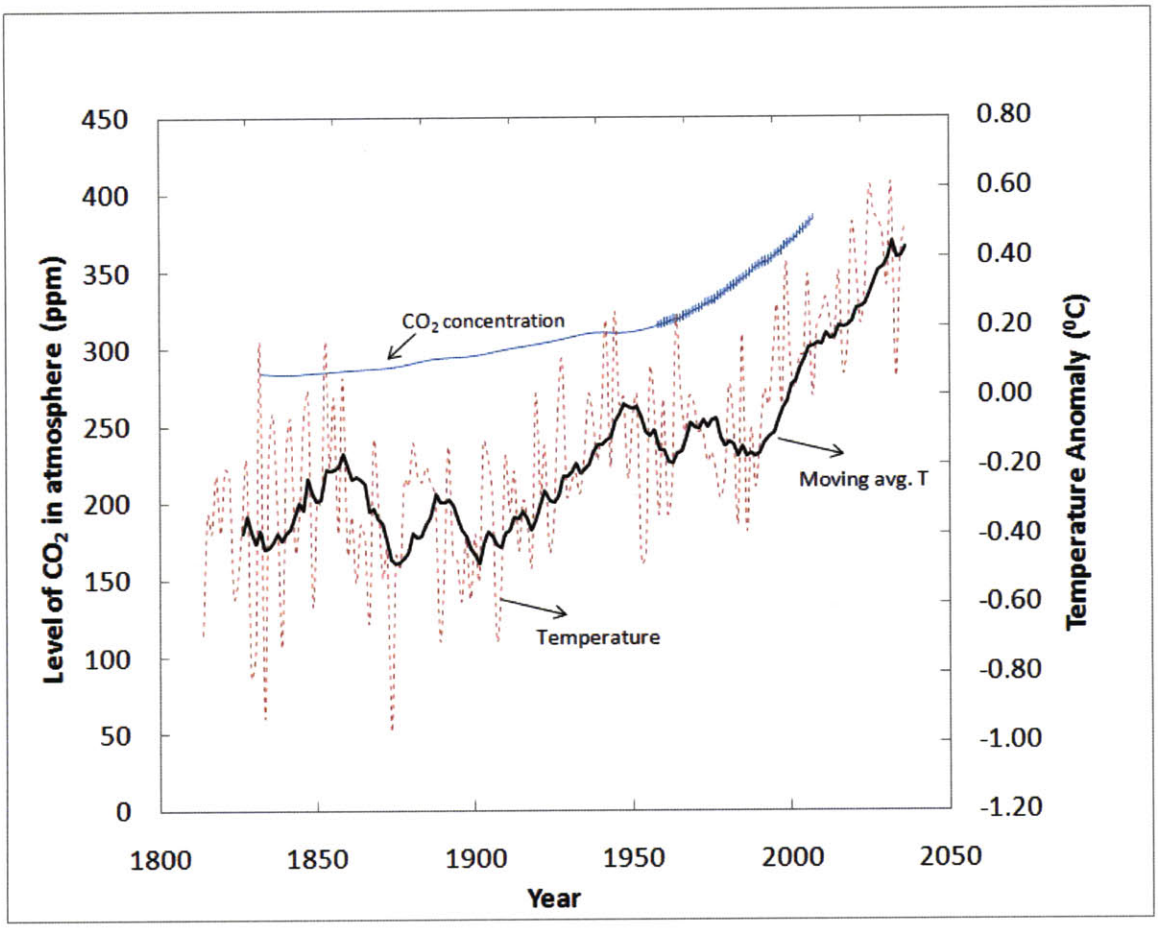

Figure 5-2: Global temperature anomaly and level of CO_2 in the atmosphere

Since a major source of GHG emissions is electricity production, (40% of GHG emissions in US are generated from electricity production [5]), governments reckon that clean energy sources such as solar photovoltaic energy will play an important role in meeting GHG reduction targets. Many states in US have already adopted renewable portfolio standards which require utility companies to produce a certain fraction of their electricity from renewable sources. Currently, 29 states in the US have RPS in place in the form of either binding or voluntary targets[6]. Figure 5-3 shows the renewable portfolio standards in place at the end of 2007 in various US states. The commitment to utilize renewable energy sources, and the consequent incentives in the form of RPS

greatly enhance the potential market for solar energy in the US. A detailed analysis of solar market in the US is the topic of the next section.

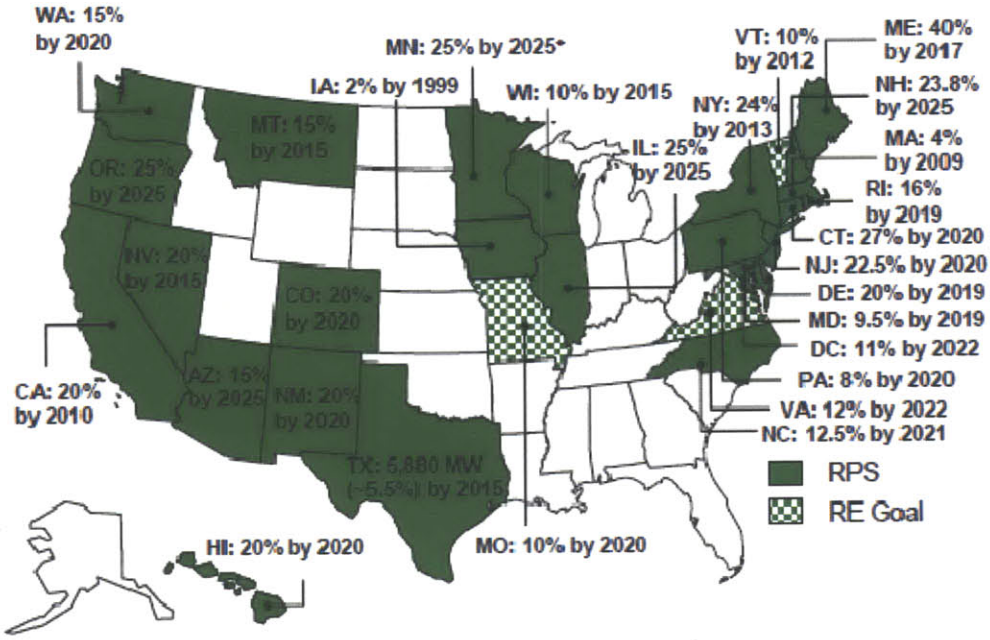

Figure 5-3: RPS in various states at the end of 2007 [adapted from 13]

5.3 Solar Photovoltaic Technologies

The solar energy industry has experienced phenomenal growth in the past decade and a half. Solar energy reaching the earth is captured through two major routes - solar photovoltaic (which converts solar energy to electricity) and solar thermal (which utilizes concentrated solar energy for direct heating). In this study, we will be focusing only on the solar photovoltaic (PV) technology. The first modern photovoltaic cells were discovered in 1954 at Bell Labs, and were extensively used for space exploration soon after. These cells are measured in terms of their efficiency, i.e. the proportion of electricity generated from incident light. In the past decade, there have been tremendous technological breakthroughs and efficiency improvements in solar PV technology with conversion efficiencies reaching 25%. The market has also experienced phenomenal growth due to extensive government subsidies and incentive programs in the recent years.

In this section, we will take a brief look at the conventional solar PV technology and compare to DSSC solar cells.

5.3.1 Inorganic silicon based solar cells

The basic purpose of a solar cell is to convert light directly into electricity. Inorganic silicon based solar cells were first discovered in Bell Labs by Russell Ohl in 1946 [7]. The principle of a solar cell is briefly explained below. When photons of sufficiently high energy (higher than the energy of band gap in silicon) hit a solar cell, electrons move from their valence band to a higher energy conduction band within the semiconductor, where they are free to move about along the layer. Each electron that moves to a conduction band also leaves a hole (absence of an electron) behind. This results in the creation of mobile electron-hole pairs. Movement of the charge carriers across the semiconductor either through diffusion or through an established electrostatic field results in electric current. The structure of a typical solar cell is shown in Figure 5-4.

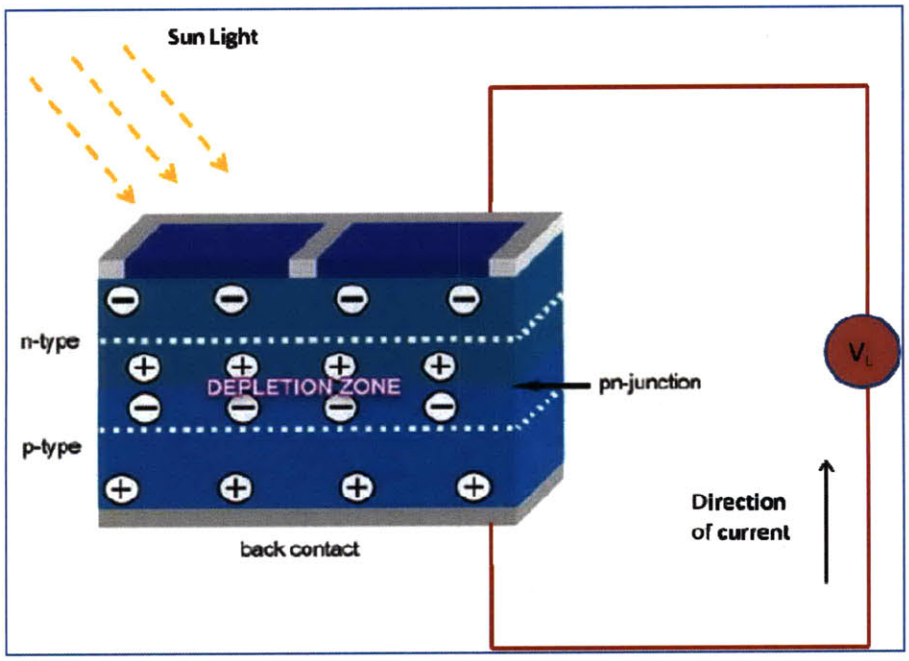

Figure 5-4: Schematic of a silicon based solar cell

A typical silicon based semiconductor consists of two layers – one doped with an n-type impurity, which makes it electron rich, and the other doped with a p-type impurity which

makes it electron deficient or "hole" rich. When these layers are put together, a PN junction is formed, which creates a steady state electrostatic field, and limits the flow of electrons directionally from the P-side to the N-side alone.

When photons of high energy hit the n-type layer, electron-hole pairs are released, and only holes are allowed to go across the PN junction (due to the directionality of the electric field). Thus, the N-side becomes electron-rich and P-side becomes hole-rich. If an external load is connected across this semiconductor, the electrons flow from the N-side over the P-side through this external load, thus generating electric current.

A typical solar cell produces only about 0.5 V in potential [8] which is too small to be useful practically. Thus, solar cells are combined in the form of packages known as modules. A typical module consists of about 72 cells and yields anywhere between 30 – 45 V in electric potential. These modules can be used to either charge a battery or integrated into a power grid using invertors.

5.3.2 Dye Sensitized Solar Cells

Dye sensitized solar cells (DSSC) use a completely different approach to generating photovoltaic electricity. These cells use organic dyes for generating free electrons upon excitation by visible light, which in turn generate electric current. The structure of a typical DSSC is shown in Figure 5-5. A DSSC usually consists of two electrodes. The top electrode is transparent and is coated with a thin layer of semiconductor particles (usually TiO_2). In a DSSC, unlike silicon-based solar cells, the photoreceptor and charge carrier are different. An organic dye, which can be excited through visible light, acts as the photoreceptor and supplies the conducting electrons. A commonly used Ruthenium based dye known as N3 is shown in Figure 5-6. This dye is coated on nano-sized semiconductor particles. When photons hit the dye, it reaches a photo-excited state (Dye*), which further decomposes into an oxidized dye (Dye^+) and a free electron. This electron is quickly taken up by the semiconductor particles and transferred through the external circuit to the load. The electrolyte has the ability to switch between oxidized (Ox) and reduced (Red) states. The oxidized dye (Dye^+) interacts with a reducing electrolyte (Red) to be

regenerated, while oxidizing the electrolyte (to Ox). The oxidized electrolyte is reduced back to its original state at the bottom electrode. Through this cycling, photovoltaic electricity is generated in a DSSC.

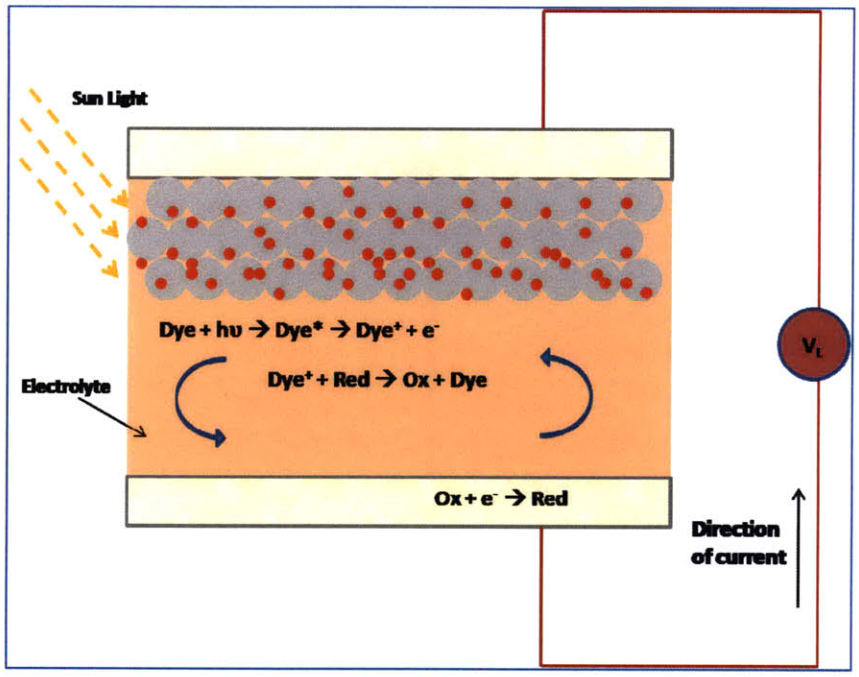

Figure 5-5: Schematic of DSSC

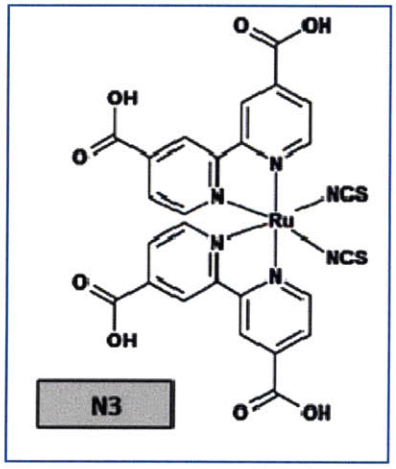

Figure 5-6: A typical Ruthenium based dye for DSSC cells (adapted from [9])

5.3.3 Comparison of Pros and Cons of Silicon based cells vs. DSSC

DSSC photovoltaic technology, though in an early stage compared to silicon based photovoltaic technology, is known to have several advantages and some disadvantages over existing the conventional PV technology. These are outlined below [10]:

- Lower purities required – In DSSC, since the charge carrier is different from the photoreceptor for a DSSC cell, the purity requirement on the charge carrier (e.g. TiO_2 semiconductor) is much lower than for a Silicon-based cell. This can result in lower of costs of manufacturing, and hence lower the cost/kilowatt of energy generation for the technology
- The DSSCs can be manufactured as flexible sheets and are mechanically robust. In comparison, the silicon-based solar cells are fragile, and hence need considerable protective layers and delicate handling. This allows DSSCs an advantage in terms of lower installation costs.
- DSSCs are able to provide good performance even under conditions of low light, cloudy skies and varying angles of incidence of sunlight [9-10]. This is because in DSSCs, electricity generation largely occurs when the process is kinetically favorable. In comparison, in silicon based PVs generate electricity only when it is energetically favorable and a large portion of energy is dissipated as heat.
- A major disadvantage of DSSC technology has been the liquid electrolyte required for operation, which could freeze under low temperatures and require advanced sealing mechanisms [10-11].
- Finally, electricity conversion efficiencies in DSSC have been comparatively lower than silicon based solar cells. Maximum possible DSSC efficiencies are known to be around 11% [12] while traditional Si based PVs have known to achieve much greater efficiencies (in the range of 40%). This is explained in the next section.

5.3.4 Comparison of efficiencies between various solar PV technologies

The most important measurement for a solar cell is its efficiency, i.e. the amount of light energy converted to electricity (measured in watt/watt). Solar PV efficiencies are

important because they are an indicator of the cost-effectiveness of solar devices. Efficiencies directly translate into the cost-per-unit-area and cost-per-watt of this technology. Tremendous research in photo-voltaics in the last two decades has resulted in a rapid improvement in efficiencies, and currently the best efficiencies have reached close to 40% [13-14]. Figure 5-7 below shows best obtained solar PV efficiencies at a research scale[13].

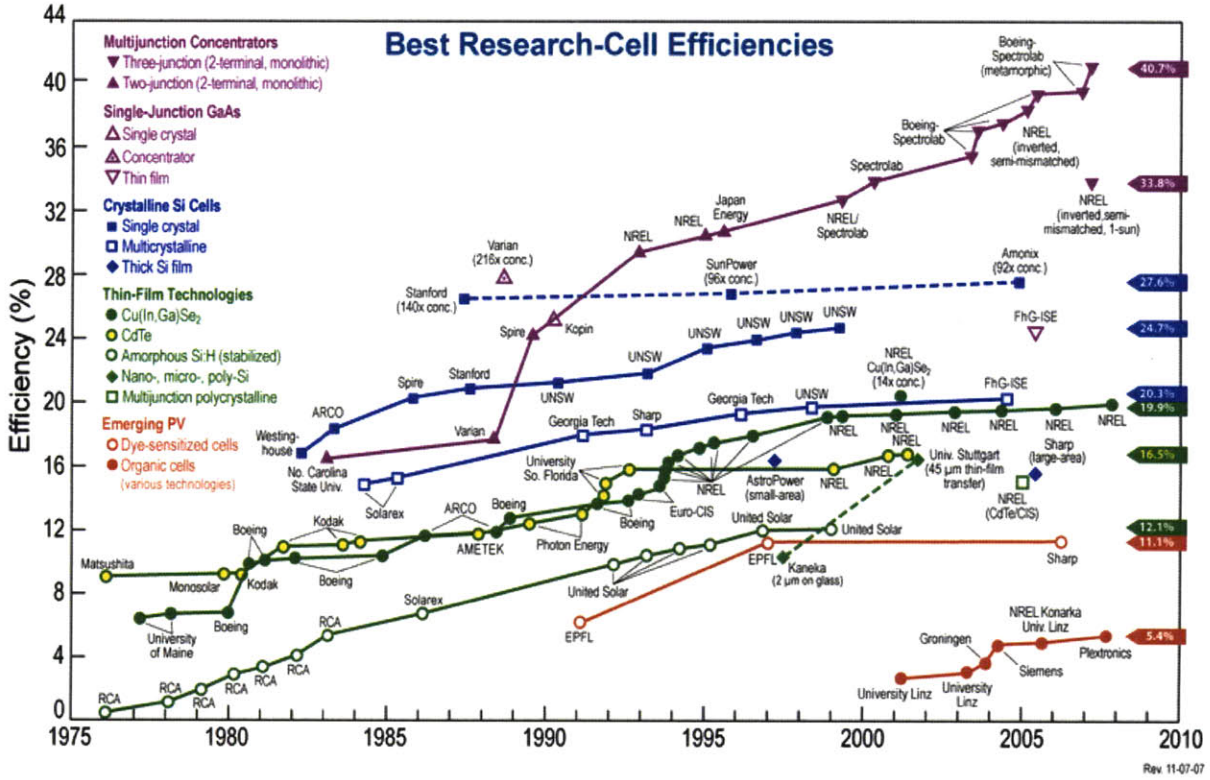

Figure 5-7: Best observed efficiencies for solar PV (adapted from [13])

From the chart we can observe that the best conversion efficiency to date has been observed at Boeing Spectrolab at 42.7%. Multi-junction solar concentrators consist of multiple layers of thin film solar cells and have displayed the highest efficiencies. However, they are prohibitively expensive to date[15]. Among the most commonly commercially available crystalline silicon technology, the best available efficiency has been around 28%. We can observe that DSSC solar cells are still at much lower efficiencies when compared to silicon based technologies, with best observed efficiencies around 11.1%. The efficiencies presented above have been observed under controlled

laboratory conditions, with a focus on obtaining maximum conversion of solar energy to electricity. In practice, a number of mitigating factors that result in much lower commercially achievable efficiencies. Researchers at National Energy Research Laboratory (NREL) refer to these as a series of efficiency gaps outlined in Figure 5-8. The reason for these gaps have been multiple - the presence of less controlled conditions while manufacturing at higher throughputs, larger devices on scaling up, and finally loss of active area during integration into modules [14].

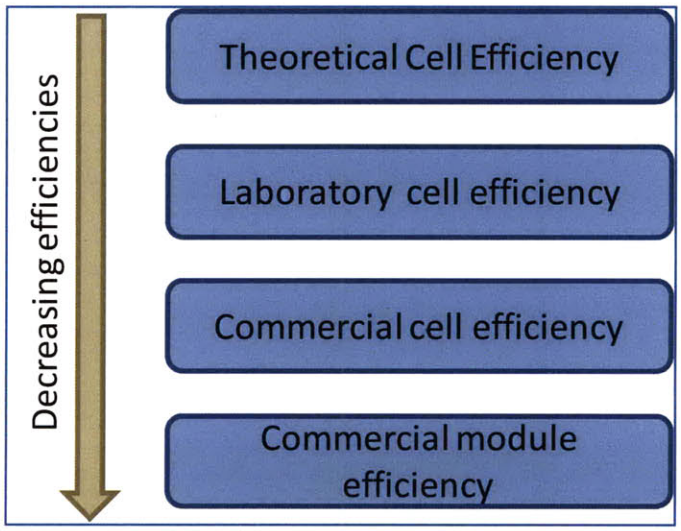

Figure 5-8: Efficiency trend for a solar cell

5.3.5 Comparison of cost

Even though DSSC has a lower laboratory efficiency of only around 11%, it is more attractive than silicon based technologies because the overall cost is potentially to be lower than conventional technologies. Hoffman [16] has done a comparison between the various silicon-based and novel technologies such as DSSC on a cost basis. Figure 5-9 below shows the results of this comparison and plots cost per kWh of electricity against efficiency (and price per area). It can be seen from this figure that DSSCs are lowest cost per kWh but are also lowest in terms of efficiency of electricity production per unit area. This means that though the efficiency of DSSC is much lower than advanced silicon based technologies, the inherent costs in manufacturing etc. still place DSSCs at an

advantage as compared to other technologies. However, a low efficiency of power per unit area requires larger area of exposure in producing the same amount of power using DSSC. This might be a limiting factor for DSSCs.

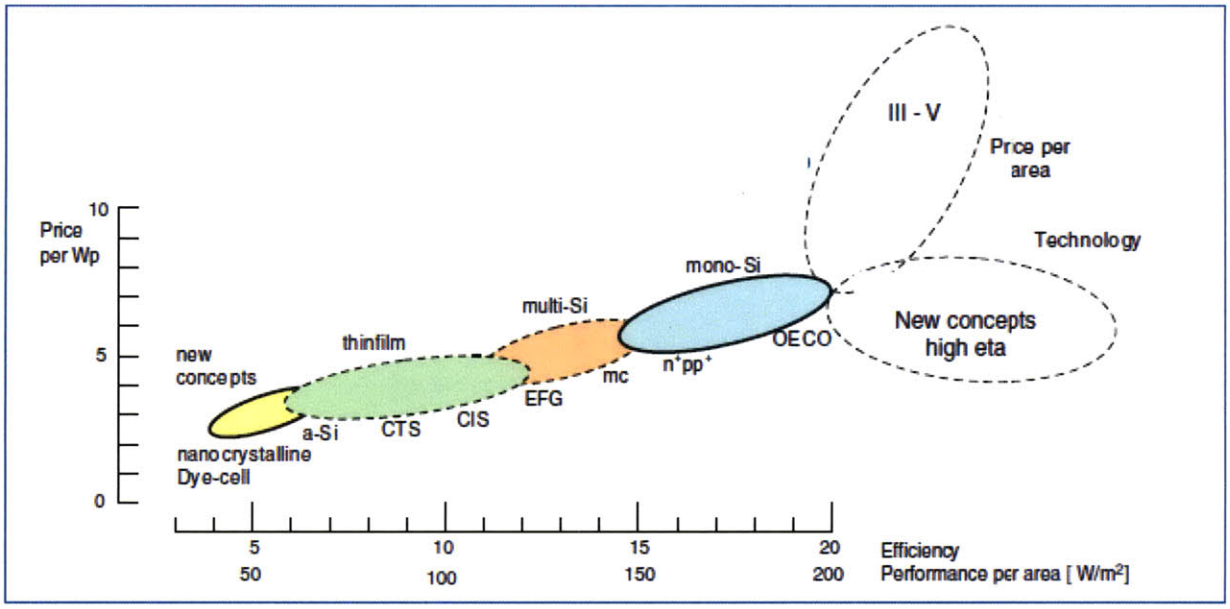

Figure 5-9: Cost comparison of DSSC vs. other solar cell technologies (from [16])

In this section, we saw the technological background for DSSC solar cells, and a comparison with the conventional silicon based solar PV technology. In the next section, we will analyze the solar PV market and evaluate its attractiveness for DSSC technology.

5.4 Industry Analysis

In this sub-section of the paper, we will try to understand the attractiveness of the solar photovoltaic industry from the perspective of a DSSC company. This is an evaluation of the external context, i.e. its market environment, and how it affects the firm performance. We will first define the boundaries of the industry/market we are planning to analyze and then, look at the industry from a value chain perspective to understand the business model. Then, an industry analysis will be carried out using a PIE&4 slices framework developed by Saloner et al [17]. This analysis will try to answer questions such as – is the solar PV industry an attractive industry to be in from the perspective of an entrant and

from the perspective of an incumbent? Is there sufficient value creation to make presence in this market attractive? If value is indeed created, how much of it can actually be captured? And finally, what characteristics of the market context are important determinants of the profitability in this industry.

5.4.1 Definition of Industry

Defining the boundaries of the industry is critical before attempting an industry analysis. For the purpose of this analysis, we define the industry to be the solar photovoltaic industry in the US. If we define the industry to be too broad, for e.g. the renewable energy industry in the US, then we tend to include too many players (such as wind energy, biofuels etc) and hence the analysis will become diluted. If the industry definition is too narrow, e.g. the Dye sensitized solar cell industry, then we will ignore many important players who will influence the attractiveness of this industry (namely other solar cell based technologies). Hence, it is appropriate for our purpose to define the industry as we have done above.

5.4.2 The solar PV industry value chain

Every industry can be represented as a series of value adding steps starting from raw materials to final consumers. Value is created at each step since the product at the end of each step is worth more than the raw material. This value is captured when this product is sold to the final consumer. Since, each participant in the value chain contributes to the final product and the value creation, profits generated on selling the product to the final consumer need to be divided between various components of the chain. However, it is extremely difficult to determine how much value a specific component of the chain has added to the final product. Naturally, each participant in the chain likes as large a share as possible of profits generated by the entire chain. Hence, the capture of value for this component depends on a number of factors specific to each industry. This can result in certain members of the value chain being 'squeezed out' of profits.

An industry analysis is essential to allow firms to think strategically about how to maximize value capture from a particular industry [17]. A great example of value created vs. the value captured is the personal computer industry. The various components of the value chain in this industry are – the suppliers of computer parts (e.g. Intel for microprocessors, Samsung for monitors), the computer assemblers (e.g. Dell, Compaq). and finally the operating system manufacturers (e.g. Microsoft). There is no doubt that enormous value is created by the PC industry. However, the exclusivity of technology and dominance by Intel for its microprocessors and the dominance of Microsoft for its Windows operating system allow them to capture most of the value from this chain. The PC assemblers (like Dell) are 'squeezed for margins' by other components of the value chain and hence, this industry is not a very attractive from an assembler's perspective. The technological advantage and supplier power of both Intel and Microsoft give them an upper hand when it comes to value capture. Similar analysis could be carried out for the Solar PV industry. Understanding which value chain components have an advantage in value capture is critical and can be performed through an industry analysis framework presented in a later section.

The solar PV value chain is shown in Figure 5-10 below [8, 18]:

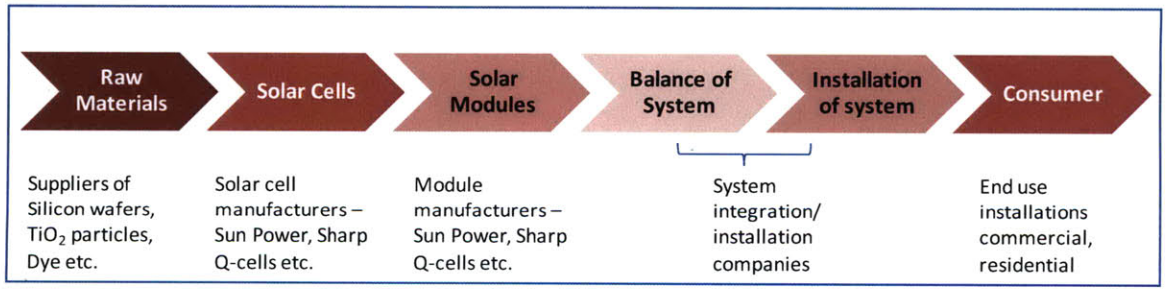

Figure 5-10: Value chain for the solar PV industry

There are six key stages in the value chain. The first component in the chain relates to raw materials required for solar cell manufacture. This could vary depending on the technology under consideration. For typical silicon-based or thin film solar cell technology, the raw material is high purity polycrystalline silicon [8]. For DSSC solar cells, the raw material would be semiconducting Titania (TiO_2) and Tin Dioxide (SnO_2)

nano-particles. The next link in the chain consists of solar cell and module manufacturers. Some large companies for silicon-based technology include SunPower in the US, Sharp in Japan and Q-cells in Germany. For DSSC, start ups exist in this space such as G24i, Hydrogen solar, Konarka etc. [10]. Most of the cell manufacturers also produce solar modules. Finally, some firms just provide the balance of system (BOS) and installation services. BOS provides the balancing between power generation and consumption for a solar application such as current and voltage regulation and occasionally storage to match power supply with demand. Typically, firms provide balance of systems and installation services together. The final link in the chain is end consumption, which could be in various forms - individual residential customers, commercial establishments looking to improve their carbon footprint and utilities generating electricity from renewable sources.

Henderson et al [8] have shown how the competition and the margins in various segments of the supply chain vary for silicon-based technologies in 2006 and has been summarized in Table 1. We can see that the most profitable place to be present in the value chain, for silicon-based technologies is upstream in raw material supply. As we move down the value chain, the number of players increases and margins start to get squeezed.

For the case of DSSC, we would expect the margins to be similar for module installers. However, commodity raw material (TiO_2) suppliers would have lower profit margins as compared to silicon suppliers due to a lack of specialization, while dye supplier will have higher margins. We still expect a significant share of profits for the cells and modules manufacturers. In order to develop an in-depth understanding of market dynamics, we need to conduct an industry analysis for DSSC.

Table 5-1: Silicon PV industry margins along the value chain (adapted from [8])

	Raw material (Silicon)	Cells	Modules	Installation
No. of players	20	100	500	5000
Revenues ($ Billions)	1.4	7.7	10.2	3.2
Gross Margin (%)	53%	21%	5%	20%

5.4.3 Porter's five forces and the PIE and 4 slices Framework

Porter [19] first suggested a way to decide whether a well-defined industry had potential for offering attractive rates of return on capital by analyzing the competitive landscape. This was based on five principle competitive threats:

- The rivalry among existing competitors reducing profitability in some way.
- The threat of new competitors emerging
- Substitute products/services challenging your business
- The bargaining power of buyers reducing your profits
- The bargaining power of suppliers reducing your profits

These are known as Porter's five forces and the extent to which each of these competitive threats are significant in an industry determines how attractive a particular industry is. Saloner et al [17] have further modified this framework to develop what is known as the PIE&4 slices framework. Below, we provide a brief description of the framework and apply it for the solar photovoltaic industry. In doing so, we will take the perspective of an entrant, since a firm using DSSC is more likely to be a start-up which would be trying to enter the solar PV market.

5.4.4 Potential Industry Earnings

Potential Industry Earnings or PIE is the total value that a firm can hope to capture from a value chain [17]. This denotes the value to final consumer minus the opportunity cost of resources used to build the good or provide the service. An industry with a higher value of PIE is always considered more attractive than an industry with low PIE. The value of PIE can be represented using the industry demand curve in Figure 5-11. Such demand curves are also used for calculating PIE quantitatively in the industry.

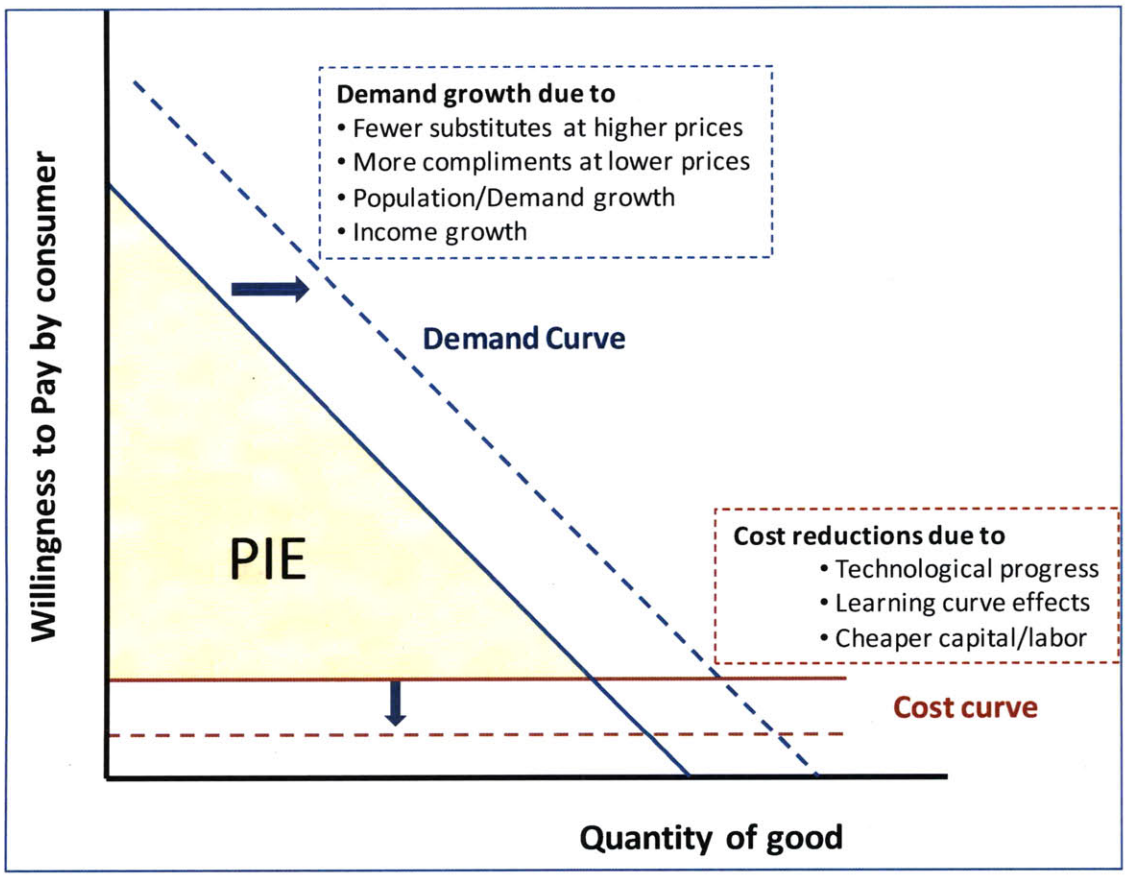

Figure 5-11: PIE represented in typical industry demand and supply curves

In the figure, we observe the demand curve is downward sloping. This is because, there are always a few consumers who are willing to pay a high price for a product, as quantity of good produced/sold increases, consumers with lower willingness to pay obtain the product. The opportunity cost curve here is shown as flat (fixed cost ($) per quantity) but

it could be upward sloping. The area between the industry demand curve and opportunity cost curve is the total PIE, which is consistent with its definition. PIE increases either due to greater demand or lower cost of supply. The factors, which enhance PIE from the demand side, include greater demand for the good for some reason (e.g. higher population). Fewer substitute products and an increase in complements also enhances PIE. Complements are goods that may not produced by the incumbent firm but are used in conjunction with the product under consideration. On the cost side, PIE could increase due to – lowering of manufacturing costs through technological progress, learning curve effects (learning curve effects show that the greater the cumulative volume a firm manufactures, the lower the cost of production of the good) and availability of cheaper labor. Using these qualitative factors, one can analyze how attractive the PIE for a particular industry is and what the trends in PIE are.

In essence, PIE determines the value creation in an industry. How much of the value that is created is captured can be analyzed using the 4-slices framework presented below.

5.4.5 Capturing the PIE – description of the 4 slices

Capturing the PIE depends fundamental market forces at play which influence the profitability of the industry. These include:

5.4.5.1 Barriers to entry for a market

Whenever new competitors enter a market, they bring with them resources and desire to gain market share, which results in a lower share of PIE for incumbents [19]. Thus, having high barriers to market entry, and a threat of sharp retaliation from incumbents keeps others firms from entering and the industry remains more attractive. Some examples of barriers to entry include barriers of technology and trade secrets, brand and reputation of incumbents, legal barriers like patents and resource barriers such as capital requirement and economies of scale. Incumbents always have an incentive to invest in raising the barriers to entry to their particular industry.

5.4.5.2 Vertical Forces – Buyer and supplier power

Buyer and supplier power refer to the amount of PIE captured by firms up and down the value chain. These are referred to as vertical forces. A supplier group is powerful if it is concentrated (few players), the product it sells is unique or differentiated and it has high switching costs (i.e. it is difficult to switch to another product for an incumbent). Buyers are powerful if they are concentrated and purchase in large volumes. Also, if the buyers are purchasing undifferentiated (commodity) products, then they can play suppliers of each other and capture more of the PIE. Thus, supplier power 'upstream' and buyer power 'downstream' determine how profitable the incumbent can be at their present location in the value chain.

5.4.5.3 Competition

In a highly competitive industry, the amount of PIE captured remains small. The effect of competition can be illustrated through consideration of the two extreme cases – monopoly (only one firm) and perfect competition (large number of firms). In the case of monopoly, since the incumbent firm is the only one capable of producing the product, they can set a high price and maximize the PIE captured. In the other extreme case of perfect competition, the product under consideration becomes a commodity, which is traded for a fixed low price in the market. This low price guarantees that an incumbent firm captures a very small share of the PIE. Thus, the state of competition greatly determines how much value can be captured in an industry.

In summary, the PIE and 4 slices framework is useful to conduct a quick analysis for a particular industry. We can determine whether sufficient value is created in this industry and how much of this value can be captured by an incumbent positioned at a specific location in the value chain.

5.4.6 Case Study – Application of PIE&4 slices to DSSC solar cell firm

The PIE + 4 slices can be applied for a DSSC firm present in the solar PV industry.

5.4.6.1 PIE for the solar PV market

In the solar PV industry, we observe rapid growth in the size and trends of PIE over the past few years. One of the biggest factors driving PIE has been the world energy demand growth, which was shown in Figure 5-1. Since the overall energy demand is growing, and a greater proportion of this demand is being satisfied by renewable energy (Figure 5-3), the demand for solar PV has been showing a sharp increase in the past few years. In addition to imposing general requirements of renewable portfolio standards on the electricity generation, many states have specific incentives to lower the costs and incentivize adoption of the solar PV technology. For instance, Arizona, Colorado, Delaware, Nevada and New York states offer incentives in the form of rebates ranging from \$2 – 4/W of solar PV system capacity installed [20]. Some other states have similar incentives as well. A combination of incentives and lower cost of technology has resulted in an explosive growth of global PV shipments in the recent years [8]. Figure 5-12 below shows the exponential growth of shipments of PV cells and modules in the past decade in the US market.

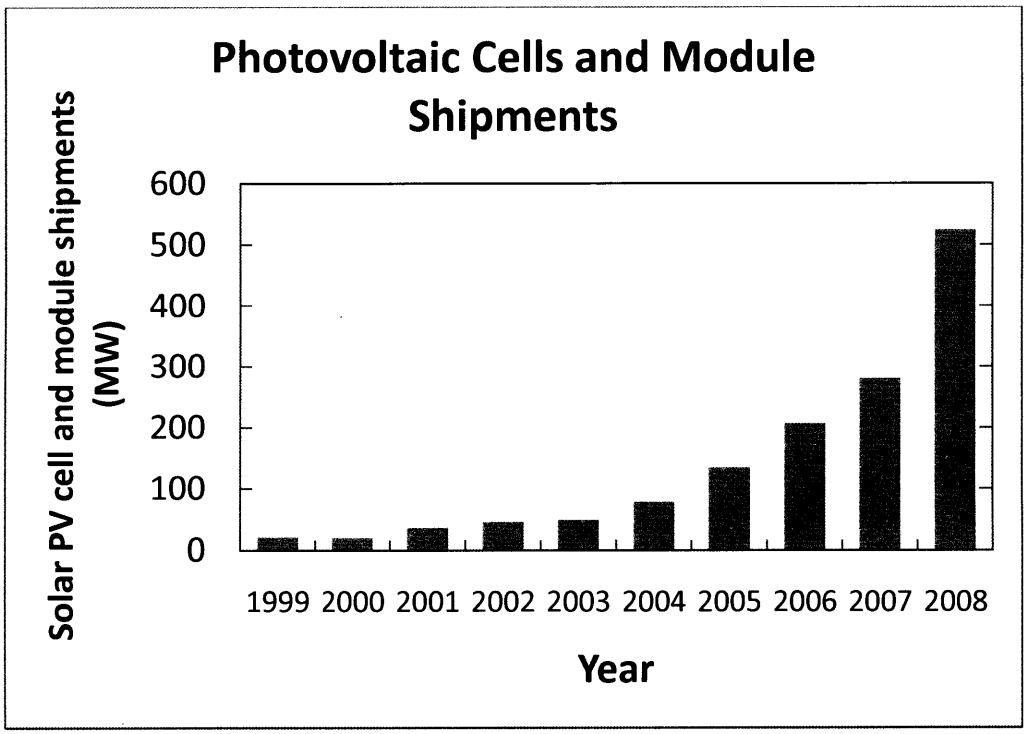

Figure 5-12: Solar PV Cell and Module shipments in the US over the last decade

In addition to a rapid demand growth as evidenced above, the solar PV module costs have seen a sharp decline since late 70s and have stabilized in the recent years to roughly $4/Watt [8]. From this evidence above, we can conclude that the solar photovoltaic industry has been growing strongly in the recent years and hence this market is an attractive one for both incumbents and entrants in terms of PIE. We can also observe some trends in the niche segment of DSSC market. According to the market research firm Nanomarket LLC, DSSC market is projected to grow significantly in the next few years due to their potential low costs, added value for consumers and technical advantages over the solar PV technology. The projected market figures for DSSC are shown in Figure 5-13. The figure shows that in the short term, close to a $100 million exists for DSSC (in 2010). This market is expected to grow to close to $500 million over the next five years. The competing third generation solar PV technology, organic photovoltaic, is expected to grow as well, though becoming a significant player at a later stage.

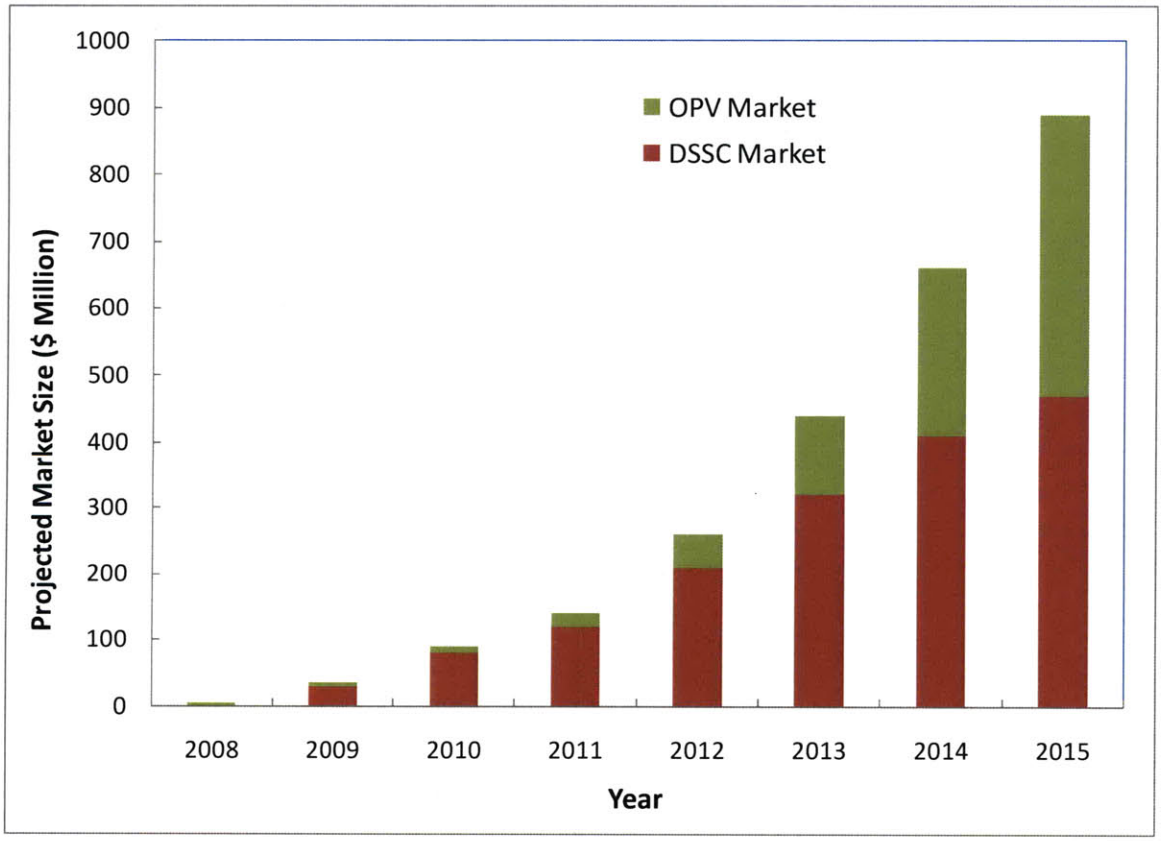

Figure 5-13: Project market for DSSC and Organic Photovoltaics (from [21])

In addition to a strong market growth potential, the DSSC technology has seen a sharp increase in research focus over the past few years. This increase in focus has been seen in both academic and industrial research, as can be seen by the increase in both peer reviewed publications and patents in Figure 5-14. These numbers were obtained from searches with key word "Dye Sensitized Solar" on Engineering Village [22] and patents were obtained from Gonzalves et al [9]. This shows that the promise of DSSC has been recognized in both industry and academia. A substantial increase in the number of patents in the recent years indicates that many companies might be building an intellectual property barrier and hence, indicates a growing commercial interest in DSSC.

We conclude that PIE in the solar PV market is quite high, and is rapidly growing. More specifically, the DSSC market is showing a strong growth potential with a solid market and growing interest among industry and academia.

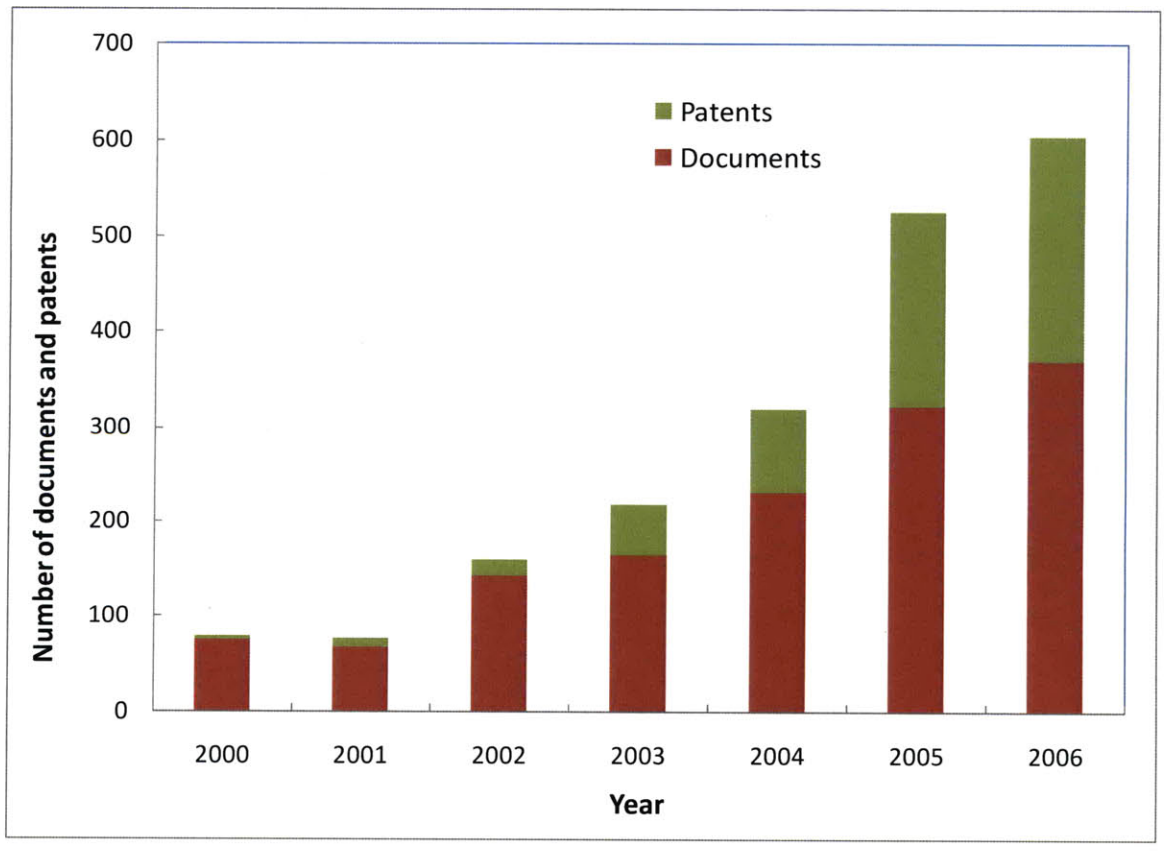

Figure 5-14: Documents and patents with DSSC research in the past few years

Next, we need to analyze the four slices for this market. We first analyze the competitive landscape for this industry.

5.4.6.2 Barriers to entry

An incumbent in the Solar PV market, utilizing silicon based technology can defend their market share due to the presence of a number of barriers – they have inherent economies of scale required to be cost effective (due to large volumes of production), capital requirements are large and finally, they have brand recognition. However, the picture is different for a DSSC technology based startup. These startups will be able challenge the barriers established by conventional silicon based players, since they bring a dramatic new technology to the market. DSSC based cells are expected to be manufactured through a roll-to-roll manufacturing process and are supposed to be more cost effective when compared to silicon wafer processing. The capital intensity for this kind of process is low as well. Finally, these startups could cater to a niche market segment where the brand recognition of large solar PV players is not significant. Thus, with appropriate technological knowhow, entry for a DSSC based startup into the solar PV market is not restrictive. On the flip side, since entry barriers for DSSC based startups are lower, they need to be pro active with respect to raising entry barriers for competing startups. This could be accomplished by establishing a strong IP portfolio (ring-fencing), rapidly building a brand in the niche segment and finally, exploiting learning curve based sustainable cost-advantage over an entering firm.

Thus, in summary, low BTE in the DSSC market is a double-edged sword. On the one hand, it allows a DSSC startup to successfully challenge large incumbents in the Solar PV market. But on the other hand, it requires firms to be proactive in raising BTE, once they become incumbents in order to maintain sustainable advantage.

5.4.6.3 Vertical Integration – Buyer and Supplier power in the market

Supplier power

The discussion of buyer and supplier power in the solar PV market can be understood after having a basic understanding of the Solar PV value chain described in section 5.4.2.

The suppliers for a silicon based PV cell are pure silicon wafer manufacturers, who command high margins (order of 50%). Hence, they wield significant power in this market. Thus, vertical integration backward into raw materials makes sense for these silicon-based manufacturers.

To understand the perspective of manufacturers of DSSC solar cells, we look at the inputs into the DSSC manufacturing process. The basic components required are Titania (TiO_2) particles, Ruthenium based or similar organic dye, the electrolyte and finally substrate for assembly. Of these materials, Titania is a commodity material widely used in paints, toothpastes etc. Thus, the supply of this should be widely available. However, the particular grade of Titania required to make efficient solar cells (i.e. monodisperse with well controlled particle size distribution etc.) might make it more expensive. Similarly, the required glass substrates and iodide electrolytes should be commonly available and hence, would indicate low supplier power. The photosensitive dye is a key component of the DSSC cell, and would be proprietary. The supplier of this dye would wield significant power and hence, this would be a possible area for DSSC cell manufacturers where value could be lost. It would make sense then for a cell manufacturer to vertically integrate into the dye manufacturing business.

Buyer Power

Buyer power for the solar PV market depends on various market segments. Utility and industrial consumers hold significant power largely due to their scale. However, the individual consumer segment is quite fragmented, and thus, do not hold much power. This would be a great segment for the DSSC startups to establish themselves initially, and remain sufficiently profitable.

5.4.7 Competitive Analysis and Industry Landscape

The competitive rivalry is very high, especially in the solar PV industry, which has grown tremendously in the past two decades, and has a large number of established players, in both conventional Si based solar and thin film solar technologies. Even in the nascent DSSC market, quite a number of start-ups exist. This section will look at the

competitive landscape for the Solar PV and DSSC solar market, and determine the extent of rivalry and how it would affect value capture in this market. A brief description of various players in the solar market has been provided at the end of this section.

The state of various players in this market can be summarized using a State of Technology vs. State of Company chart shown in Figure 5-15. We can observe from the figure that most of the large established players in the Solar PV market currently operate in the conventional (1^{st} generation) and thin film (2^{nd} generation) technologies. Chinese companies SunTech and JASolar are both in the rapidly growing segment. It can also be seen that the largest and most mature player (Sharp) is most lagging from a technological perspective. The established players in this market are still operating in conventional PV technology. On the other hand, most of the companies operating in the 3^{rd} generation technologies like DSSC and organic photovoltaics are early and late stage startups. In the DSSC technology, G24i looks the most promising at this stage whereas Konarka looks most promising for the organic photovoltaic technology. Thus, the competition is segregated into two parts in the figure. One set of large established players in conventional field, and the other set of startups in novel 3^{rd} generation technologies.

A more detailed description of various competitors is provided in the next section to gain a more thorough understanding of the market place.

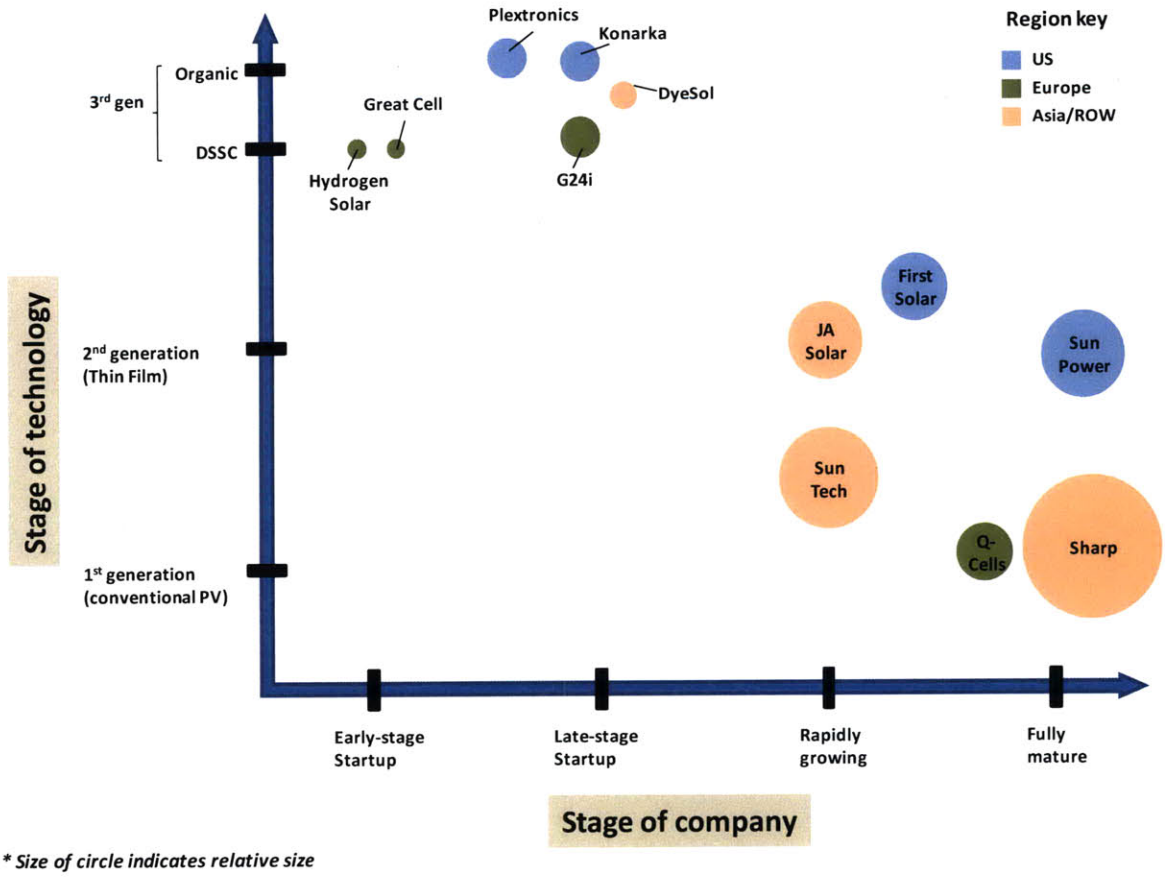

Figure 5-15: Figure summarizing positioning of key players in the Solar PV market

5.4.7.1 Key players in the Solar PV industry

The Solar PV is a global industry with competitors spread across US, Europe and Asia. Below is a description of a few key players in the solar PV industry and the start up space.

Sharp Solar –

Sharp solar is a part of the Sharp electronics conglomerate headquartered in Japan and is the global industry leader in solar PV production. Sharp was founded in 1959 by Tokuji Hayakawa and was one of the first players in the Solar PV field. It had a total global installed capacity of 2 GW in 2008, and hence, commanded an impressive market share of 25% of the total global installed Solar PV capacity [23]. Sharp has a strong presence in Japan, Europe (Germany) and the US. Sharp has developed manufacturing process to

mass-produce high efficiency polycrystalline silicon solar cells and multi-junction thin film solar cells. Recently, Sharp has introduced innovations in the area of deploying thin film solar cells with built in LEDs in building walls as well as large scale high capacity (1 GW) horizontal deployments of thin film solar cells.

Q-Cells:

Q-Cells is based in Germany, and is a large player in the Solar PV market with about 550 MW of installed capacity. Q-cells was founded in 1999, and has experienced phenomenal growth in the past decade due to a favorable German market, with substantial incentives [24]. Currently, it has a strong presence in Europe and is rapidly expanding into the US and Canada. Recently, the company has been going through a tough time following the financial crisis. It has altered its business model to sell of many of its portfolio companies, and is undergoing a transformation from being a pure solar cell player to a more diversified PV company manufacturing both modules and systems. Traditionally, Q-Cells has produced polycrystalline solar cells.

SunTech –

SunTech is a solar PV company founded in China in 2001 and with sales in Asia, Germany and the US. In January 2009, SunTech reported reaching an installed manufacturing capacity of 1 GW riding on the boom in demand for solar PV in the Chinese economy [25] and currently stands at close to 1.4 GW [26]. Thus, SunTech commands about 18% of the global market. This company primarily produces solar PV using polycrystalline silicon wafers and is highly competitive primarily due to low production/manufacturing costs. Recently, SunTech has set up its first manufacturing plant in Arizona. With support from the Chinese government, it has emerged as a formidable competitor to European and Japanese Solar companies.

SunPower [27] –

SunPower was founded by Dr. Richard Swanson, a former Stanford university professor in 1987. SunPower's core competency is to produce high efficiency, high performance thin film polycrystalline silicon modules. SunPower targets all the three segments for

solar power - residential, commercial and utility segments. Currently, SunPower has a strong presence in California (US market) and is a key player in German, Spanish and Italian markets. It has expanded recently into Japan and some other parts of Europe and Asia. Currently, SunPower has a manufacturing capacity of 574 MW and expects its capacity to increase to 1 GW by late 2010 [26]. SunPower is a consolidated player and plays in various portions of the value chain – solar cells, modules and installation of the systems.

The rest of the solar PV market is divided among a number of small players. The silicon based solar PV industry is thus, consolidated between a few entrenched large companies who have manufacturing capacities in the GW range. We can observe that with many large entrenched incumbents and the sheer numbers of other small competitors make the solar PV industry intensely competitive and makes for a very difficult environment for a start up. In addition to the players competing with solar PV technology, a number of start-ups exist currently who are looking to commercialize the next generation of solar technologies. The next section outlines the various startups utilizing non-Si based PV technologies.

5.4.7.2 Key startups in Solar PV area

There are a number of startups looking to commercialize the DSSC based technology and related technologies such as organic photovoltaic solar cells. Below is a brief description of some key startups in this field.

Konarka Technologies [28-29] –

Konarka Technologies is a cleantech startup founded in 2001 by Nobel Laureate Alan Heeger. It is based in Lowell Massachusetts, and is currently developing both organic polymer solar cells and dye sensitized solar cells. Konarka has developed a novel photoreactive polymer called Powerplastic® which can be coated on flexible sheets using roll-to-roll manufacturing. These sheets could then be integrated onto a variety of end-use applications, thus producing solar power on a variety of portable objects. This will potentially allow Konarka to tap into new markets and applications. Konarka claims that

roll-to-roll processing capabilities will allow low cost scale up and mass production capabilities. Currently, Konarka has more than 350 worldwide patents and filings covering various aspects of their technology (such as materials, devices, processes, and applications) that provides it with a great IP fence to further scale up its operations. Konarka is also recently developing a roll-to-roll manufacturing facility for the organic PVs and expects to be able to ramp up to a capacity of 1GW production in the next few years.

DyeSol [30] –

Dyesol was founded in 2004 to commercialize the DSSC technology developed at EPFL and successfully manufacture DSSC related products at a commercial scale. Dyesol manufacturing facilities are located in Australia (started in 2008) and currently, the company sells a variety of DSSC related products to assist researchers in developing DSSC prototypes. These include dyes, pastes, electrolytes and substrates. Thus, they currently occupy a position one step up the value chain as compared to its direct competitors (i.e. supplying raw materials). They are currently partnering with a number of downstream DSSC companies in order to incorporate the DSSC materials into their products (e.g. building material, consumer electronics etc)

G24i [31] –

G24i was founded in 2006 in Cardiff UK to manufacture DSSC cells on a commercial scale. They hold a variety of patents and have Prof. Michael Graetzel of EPFL (the original inventor of DSSC technology) on their board of advisors. They have recently built a 180,000 square foot manufacturing facility in Wales to manufacture DSSC cells in a roll to roll fashion. They began shipping their first commercial product in 2009, and produce solar products for both indoor and outdoor applications. A typical product includes a portable universal solar charger that could be built into a backpack and used to charge portable electronic devices. Their vision is to develop devices that would be able to charge in the sun, and hence allow consumers to become free from power outlets.

Hydrogen Solar [32]

Hydrogen Solar is an early stage company founded in 2002 and based in England. It is currently developing a technology to utilize DSSC solar cells for producing clean hydrogen at a low cost. The electricity generated in DSSC is used in tandem with their proprietary technology to produce hydrogen using low cost materials. This company is still in an early stage with a working prototype and is currently doing research to build a strong IP portfolio for future commercialization.

5.4.8 Conclusions from Industry Analysis

We have seen that the solar PV market is highly attractive and fast growing industry. Solar PV shipments have grown exponentially in the US and the world over the last decade and this growth is expected to continue. In addition, increasing R&D in the DSSC market and ever improving efficiencies mean that the PIE for this market is growing strongly. From the four slices perspective, barriers to entry (BTE) are high due to high capital requirements and learning curve advantages for the incumbents in the conventional PV market. However, for a new technology like DSSC, the BTE are not so high due to lower capital outlays and primarily consist of IP barriers. Supplier power (esp. Silicon) is strong in conventional PV market but that is, again not necessarily the case for DSSC, since most raw materials are commodities. However, manufacturers of photo-responsive dyes might have some leverage as suppliers.

This market is defined by its competitive intensity. Since it is a fast growing market, there are a number of large and established players in the conventional PV space, with GWs of manufacturing capacity. Hence, this would be a difficult market to compete for a startup. However, if the DSSC based technologies are able to serve a niche market, which leverages their competitive advantage (where the conventional players are not able to compete), they might still be successful. This is the topic of the next section.

5.5 Implications for strategy for a DSSC based startup

5.5.1 Evaluation of competitive advantage for DSSC based startup

We have looked at the comparison of pros and cons between DSSC and conventional PV technologies in the previous sections. In the last section, we also obtained an understanding of the external (i.e. market) context in which a DSSC startup would be operating. In order to better evaluate the relative impact of various advantages of DSSC over conventional PV, we have developed a framework to compare these from a technical and economic perspective and place them in the market context. The summary of this comparison is presented in Table 2.

We can see from the table that the three most relevant features that will provide DSSC technology with an advantage include the robustness, superior performance under low light and portability. In the current market context, these advantages will allow a DSSC start up (e.g. G24i) to access new markets which currently do not utilize solar energy e.g. integration in backpacks, or for building facades. Since the large incumbents utilizing conventional technology do not play in this market, it provides these startups the time to establish themselves and gain critical mass. Once they grow sufficiently to cross the size threshold, it would be possible to build upon the potential lower costs of the DSSC technology to gain long run sustainable advantage. The case for targeting a niche market and the case for not building on cost advantage are the topics of next section.

Table 5-2: Comparing the relative competitive advantages of DSSC technology with conventional PV technology

Technical Advantage	Economic Advantage	Market Context	Potential Competitive Advantage	Relative impact
Ability to manufacture flexible and mechanically robust sheets	Lower costs for installation and protective layers	Conventional players lack this capability currently	Ability to tap into new markets e.g. building facades etc. which require flexible sheets of solar PV	
Good performance under low light conditions/ varied angles of incidence	Higher utility over lifetime i.e. lower capital cost per kWh over lifetime	Conventional PV performs poorly under a lack of standard conditions	Ability to tap into new markets e.g. indoor PVs, newer geographies with low insolation	
Portability of power generation	Possibly cheaper than battery power?	Conventional PV lacks portability	Ability to integrate PV to new products e.g. backpacks for portable charging	
Roll to roll manufacturing capability	Lower initial capital outlay, lower manufacturing cost/KW	Conventional PV is capital intensive, however manufacturing assets currently in place for most incumbents	May ramp up production faster than incumbents. Lower barriers to entry	
Lower purity of raw material (e.g. TiO_2) acceptable	Lower cost of raw material translates to lower cost/kWh of power generated	Conventional PV requires high purity silicon for manufacture	Cost/kWh advantage is good from a long run perspective. However, in the short run, incumbents will use their excess capacity to nullify this advantage.	

5.5.2 Incumbent response in the face of entry

As indicated in the earlier section, even though the DSSC technology has the potential to provide a lower cost/kWh than conventional silicon based technology; this advantage might not be valuable in the short run. This can be understood by considering the

response of incumbents to the entry of a startup. An entry of a new competitor is always bad for incumbents, since it represents a potential to lower incumbents' share of industry profits as well as increase competitive intensity in the industry [17]. Thus, the existing firms display different kinds of strategic behavior to raise entry barriers and deter entry. In order to rationally predict this behavior of incumbent firms, when a DSSC firm enters the market, we need to look at the typical strategies employed in more detail. Here, *incumbent* will refer to conventional PV firms and *entrant* will refer to a startup employing DSSC technology.

Besanko et al [33] describe these responses which include –

- **Limit or predatory pricing** – Limit pricing refers to a strategy whereby an incumbent firm charges a lower price for a particular product, before entry occurs. Typically, in limit pricing the incumbents have a marginal cost advantage over the entrant. In the situation when this is not true, but where the incumbent has excess capacity, the cost of expansion has already been *sunk*. In this situation, again it makes sense for the incumbent to lower prices temporarily (even below than their marginal cost), in order to make it less attractive for the entrant. Here, the firm employing predatory pricing expects that the losses it incurs while driving competitors from the market, can be made up later through profits during a period of lower competition.

- **Capacity expansion** – Incumbent firms expand capacity, even when demand is not as high, in order to change how the entrants view the post-entry competition. This strategic action serves as a credible commitment (i.e. a veiled threat) which shows that the incumbent can expand output rapidly, at low marginal cost should entry occur.

We can understand these strategic actions through an example. In 1986, a startup Irish airline company, Ryan Air established a low cost airline on the Dublin-London route and started offering significantly lower fares [34] than its rivals British Airways and Aer Lingus (I£99 compared to I£208). Ryan Air was able to offer these discount fares due to its low cost, economy airline strategy as compared to the "full service" large airlines.

However, at that time, both BA and Aer Lingus were flying at roughly 60% of their total capacity. Perceiving the threat from an upstart, both BA and Aer Lingus decided to cut fares aggressively, and offer early bird discount fares (around £69) to strategically utilize this excess capacity. Thus, though their profits dipped in the short term, they were able to drive Ryan Air out of the market through aggressive acquisition of Ryan Air customers.

The present state of the silicon industry is similar to the above case. There are few large incumbents, who have close to 8 GW of manufacturing capacity in 2009. Due to the recent downturn, the solar industry is experiencing serious over capacity and hence, the capacity utilization has been at low nearing 30% [35-36]. Thus, under the threat of entry, both predatory pricing and capacity expansion are possible responses to a DSSC startup. The resulting price competition is bad for everyone; however the impact will be worst on a startup. Thus, cost based advantages and price based competition is not a recommended strategy for a new entrant into the solar PV market. The solution to this dilemma is presented in the next section.

5.5.3 "Judo strategy" to avoid pre-emption during market entry

5.5.3.1 Judo Strategy

For an entrant, one way to get around the typical response of large established incumbents is to utilize their small size to their advantage [33]. This is known as "Judo Economics". Here, the entrant *credibly* commits to being small, and stays in a niche market. This could be done by choosing markets or customers who are off the mainstream of the industry. Under these circumstances, the large incumbents would discover that lowering prices to drive out a small player will not be sustainable, because of the losses from the rest of its customers, and would tend to ignore this "small" competitor. In the previous example of Ryan Air vs. BA and Aer Lingus, had Ryan Air initially committed to stay in a niche segment of flying second tier cities, probably it would not have solicited an aggressive response from its established rivals.

In the current case, for a DSSC start up, it would have to show a *credible commitment* to stay small, by not targeting the mainstream utility or industrial customers of conventional PV technology. Rather, if they target the individual consumer segment through differentiated products, they have a greater chance of success.

5.5.3.2 Targeting a niche market

Firms can survive in competitive industries by targeting a so-called niche market. A niche market is one where an incumbent sells a sufficiently differentiated product, such that the competition is much muted [17]. This differentiation could be in terms of quality, level of service, customer segment targeted and functional features in the product. The benefit of differentiation is that products compete most closely to others which are closest to them. In the case of DSSC start up, the first three competitive advantages (flexibility/robustness, wider operating conditions and portability) will serve to differentiate the product from a conventional PV product, and hence the target segment would be individual customers and consumer products. Also, the competition will now be limited to other startups who are trying to commercialize similar third generation solar cell technology.

Thus, in the above section, we have seen how a DSSC start up can compete against established incumbents in a growing market by exploiting the right competitive advantages. The final subsection will deal with the appropriate initial strategy for a start up after market entry.

5.5.4 Strategy for commercialization after market entry

In this subsection, we will try to answer questions which pertain to the business strategy for a start up immediately after market entry. There are many situations when the first and most innovative firm on the market fails to profit from their innovation. Rather, it's the imitating firms who outperform the pioneering firm and gain market share over it. Teece [37-38] has done seminal work in this area and developed a framework to guide the initial strategy for a start up. The two key questions include – when is it appropriate

for a firm to license the new technology to an established player vs. internally develop the product; what extent of ownership of complementary assets is required to succeed in the market place? We will first briefly look at the theory developed by Teece and then apply the framework to a DSSC based start up.

5.5.4.1 The Teece Framework – how startups benefit from innovation

The history is littered with examples of situations where the most innovative firm did not make the cut. The UK firm, Electrical Musical Instruments (EMI) was the first to introduce the CAT scanner to the market, through original research. But it was GE ultimately dominated this market. RC Cola had to cede ground to Coke and Pepsi and Xerox lost to Apple and IBM after developing some key ideas for the personal computer. Teece systematically analyzed what made innovators succeed or fail at realizing value from their innovation [37]. Based on his analysis, he came up with three key characteristics which determine the initial strategy of a firm.

Appropriability regime – Appropriability regime refers to the ease of imitation of the technology and the efficacy of the legal mechanisms of protection. A firm could operate in a "tight" or "weak" appropriability environment. In a tight environment, the technology is relatively easy to protect, and legal mechanisms are enforceable. Examples would include a pharmaceutical product whose chemical structure cannot be copied by an imitator. Here, the patent protection can be strictly enforced. In a weak appropriability regime, the legal mechanisms such as patents or industry practices such a trade-secrets are hard to enforce and it is easy to either "invent around" them or imitate. Examples include process innovations and products which could be reverse engineered.

Complementary asset specialization – An innovation always needs a set of complementary assets to be commercialized successfully. These include capabilities or assets such as manufacturing infrastructure, marketing, vendor & customer relationships and brand recognition. These capabilities could either be "specialized" (require significant capital investments and know-how before utilization) or be "generic" (do not require to be tailored for the innovation specifically). The intuition here indicates that

firms that control specialized complementary assets would hold a lot of power at the market and hence obtain a greater share of profits, while the converse is true for firms controlling generic assets.

Dominant design evolution – In any innovation, the product design goes through a number of iterations, before finally a dominant design emerges in the market place. Examples of dominant design include the Apple I-Pod for an MP3 player, which all competitors now try to emulate. Before a dominant design is established, there is fierce competition amongst firms based on design and to get their design to get established as the standard.

Of these three characteristics, the appropriability regime and the specificity of complementary assets are relevant for the case of a DSSC start up. Due to the presence of an established solar PV market, a dominant design for solar PV cells has already been developed. Based on Teece's work [37-38], we can develop the following framework as indicated in Figure 5-16 to recommend an initial strategy for a start up.

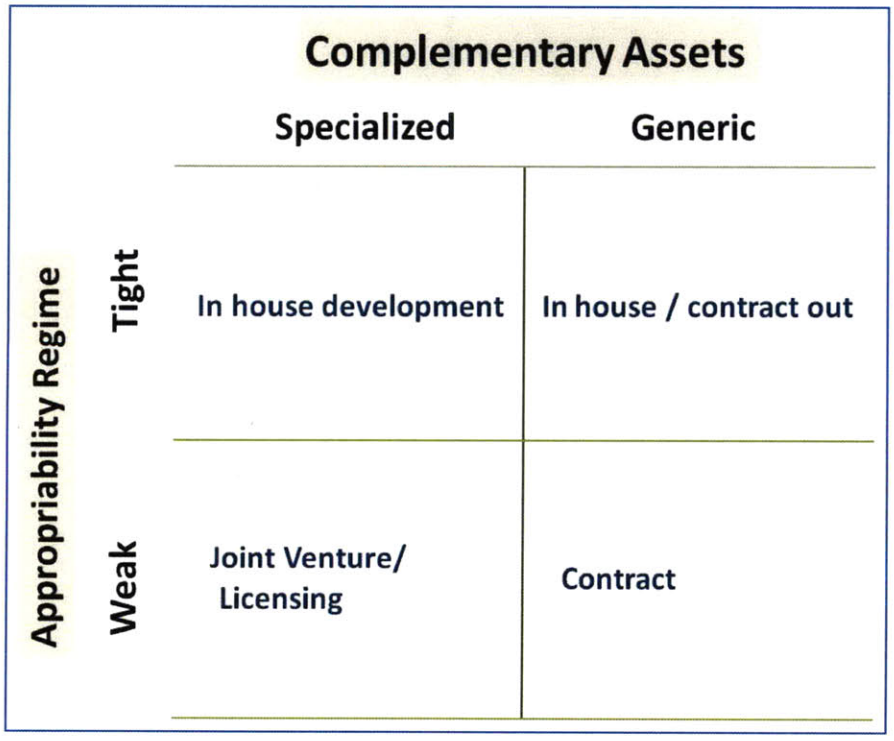

Figure 5-16: Initial development strategy for a start up

Here, the 2 by 2 chart indicates various scenarios that could exist based on the regime of appropriability and complementary assets. We describe the four scenarios below:

Appropriability tight, complementary assets specialized

If the appropriability regime is tight, in general it allows the start up additional time to be successful, on its own. Thus, in the case where the complementary assets are specialized and require significant adaptation and capital investment specific to the technology, it is still possible to commercialize the technology in-house. Examples of such innovations include pharmaceuticals, which have strong patent protections on drug formula and need to develop specialized manufacturing processes for commercialization.

Appropriability tight, complementary assets generic

In the case where manufacturing, and other capabilities (sales and marketing, distribution channels) are generic, a number of firms exist, which could perform these operations. Since, the appropriability is tight, it would be relatively safe for the start up to contract out the actual operations of manufacturing etc., and still retain a significant share of the profits. If they choose to, they could develop these capabilities in house as well. Examples of such companies would include speciality process developers for refinery processing (e.g. UCI)

Appropriability weak, complementary assets specialized

In the situations, where appropriability regime is weak, the start-up is at a significant disadvantage when the complementary assets are specialized. In this scenario, in a promising market, it would be a matter of time before established competitors work around patents to develop their versions of the product. Thus, its critical to act early and gain a first mover advantage. If development of specialized complementary assets is capital and time intensive, it would be advisable for the start up to license its technology to an established player which could be an eventual winner in the race.

Appropriability weak, complementary assets generic

In the final scenario of weak appropriability and generic complementary assets, it would be advisable for the start up to contract their operations early and build on their first mover advantage through brand development. This would provide the firm with an advantage in a crowded market place, in the long run.

Thus, in this section, we observed the theory behind deciding on the initial strategy for a startup to successfully commercialize an innovation. In the next section, we will apply this framework to a DSSC startup.

5.5.4.2 Application to a DSSC start up

In order to apply the Teece framework to a DSSC startup, we need to qualitatively analyze the various elements of technology to determine the nature of both appropriability and complementary assets.

Appropriability

On analyzing companies commercializing DSSC technologies, it can be conjectured that the appropriability regime is tight. The process of DSSC is covered by IP from multiple aspects of the technology – materials utilized in the production are patented, the devices themselves are patented (i.e. putting the materials together in the form of a device), and finally the processes to manufacture DSSC devices and some of the applications in which they could be utilized are patented as well [31]. Thus, this technology is covered from many angles, so the appropriability is tight.

Complementary Assets

The most common method to manufacture of DSSC seems to be through a roll-to-roll manufacture process. Roll-to-roll manufacturing process has been in existence for a very long time and was utilized earlier in the production of photographic films and in screen printing applications [39-40]. Currently, this technology has been evolving in the production of printable electronics. Thus, we can infer that the level of specialization is

low in manufacturing assets. Since the DSSC start up will be targeting a niche market, new vendor and customer relationships will need to be established (no existing large players in this arena). Thus, the complementary assets are definitely more generic than specialized. Some of the manufacturing equipment may need to be customized, however since they will be building on existing technology, it should be relatively faster. Thus, we can conclude that the complementary assets are more generic than specialized.

From our framework in Figure 5-16, we can observe that for tight appropriability and generic complementary assets, the strategy could be to either develop some specialized capabilities in-house while contracting out the generic processes. On further research, we find this strategy is being employed by some startups. For e.g. G24i (described earlier) performs the roll to roll manufacturing of DSSC cells in house, through customized manufacturing equipment (specialization high). However, for the finishing of modules and encapsulation, which is a fairly generic operation in the industry, G24i prefers to outsource, thus saving time and resources.

5.5.5 Summary of recommended strategy for a DSSC based start up

In this section of the capstone chapter, we developed a strategy for a DSSC based start up company to succeed in the solar PV market. First we analyzed the competitive advantages of DSSC based technology vs. silicon based solar PV technology. We determined that feature based advantages of DSSC technology such as robustness and flexibility of solar cells, ability to operate under varying level of light and portability are key competitive advantages that should be exploited in the market. Also, we analyzed possible incumbent reactions to market entry of a new competitor and recommended against competing on price (utilizing cost based advantages). We recommended following a "Judo" approach in order to mitigate aggressive reactions from incumbents; this involves making a credible commitment to stay small in the initial phase for a startup company.

We also developed the strategy for a DSSC start up after market entry by following Teece's framework [37] of focusing on regimes of appropriability and complementary

assets. We determined that a DSSC start up would lie in the regime of tight appropriability and generic complementary assets (more generic than specialized). For this scenario, we recommended that it would be appropriate to contract out the most generic of operations while retaining any specialized operations in-house. All the while, the focus of the start-up should be on building on their competitive advantages to develop a sustainable brand image and reputation in the market place. This will allow them the ability to compete against established players in the long run.

5.6 Conclusion and the role of fine particles in energy

In this capstone paper, we have attempted to highlight the role of fine particles in the energy industry. This was done with a particular focus on the 3rd generation solar cell technology – the Dye Sensitized Solar Cells. We motivated the importance of renewable energy, particularly solar, in providing a clean source of energy for our growing energy needs. Then we briefly focused on the DSSC technology vis-à-vis silicon based solar technology and the role of fine particles in success of DSSC. We also outlined the key advantages of DSSC and how DSSC can dramatically enhance the integration of solar cells into everyday objects, potentially opening up new markets.

In order to analyze the attractiveness of DSSC in the solar PV market, we utilized the PIE & 4 slices approach. We found that this market is exhibiting strong growth in potential industry earnings with an expected market of $500 million over the next 5 years (a cumulative accumulated growth rate of 100% per year). We also found that one of the key forces in this market is the competition from established players (at least in the conventional PV space). We mapped the existing competition based on their size, maturity and stage of technology in order to get a better understanding of the market context. Finally, we recommended developing expertise in producing the DSSC dyes in-house to mitigate effect of supplier power in this industry.

In the final section of this report, we developed a strategy for a DSSC based startup to succeed in this attractive but competitive solar PV industry. Here, we mapped the relevance of competitive advantages of DSSC vs. conventional technology based on

technical, economic and market contexts. We recommended that this start up adopt a Judo approach to market entry to mitigate aggressive incumbent behavior. After analyzing the market conditions pertaining to the success of DSSC technology (i.e. appropriability and complementary assets), we recommended that the firm contract out the most generic operations while retaining specialized operations in house.

Thus, in this paper, utilizing the example of DSSC technology, we have outlined the role of fine particles in the fast growing renewable energy industry.

5.7 References –

1. IPCC, *Climate Change 2007: Synthesis Report*, R.a.R.A. Pachauri, Editor. 2007.
2. Mauna-Loa-Observatory. *CO2 concentration at Mauna Loa observatory.* Available from: http://www.esrl.noaa.gov/gmd/ccgg/trends/
3. Hadley-Center. *Hadley Center Temperature Data.* 2010; Available from: http://www.cru.uea.ac.uk/cru/data/temperature/.
4. Wikipedia. *Copenhagen Accord.* 2010; Available from: http://en.wikipedia.org/wiki/Copenhagen_Accord.
5. EIA, U., *Carbon Dioxide emissions from generation of electric power in the US.* 2000.
6. USDOE. *States with renewable portfolio standards.* 2007; Available from: http://apps1.eere.energy.gov/states/maps/renewable_portfolio_states.cfm.
7. Perlin, J., *The Story of Solar Cells*, in *Organic Photovoltaics*. 2009, CRC Press.
8. Henderson R, C.J., et al. *Sun Power.* 2006.
9. Goncalves, L.M., et al., *Dye-sensitized solar cells: A safe bet for the future.* Energy & Environmental Science, 2008. **1**(6): p. 655-667.
10. Wikipedia, *Dye Sensitized Solar Cells.*
11. Coakley, K. and M. McGehee, *Photovoltaic Cells Based on Nanoporous Titania Films Filled with Conjugated*, in *Organic Photovoltaics*. 2009, CRC Press.
12. ACS, *Ultrathin Dye-sensitized Solar Cells called most efficient to date.* Science Daily, 2006.
13. Kazmerski, L., *NREL compilation of best research solar cell efficiencies*, USDOE, Editor. 2010.
14. NREL, *Closing the gaps*, NREL, Editor. 2005.
15. Wikipedia. *Solar Cells*. Available from: http://en.wikipedia.org/wiki/Solar_cell.
16. Hoffmann, W., *PV solar electricity industry: Market growth and perspective.* Solar Energy Materials and Solar Cells, 2006. **90**(18-19): p. 3285-3311.
17. Saloner, G., *Strategic Management*. 2001, New York: John Wiley.

18. PV Group, A.E.I.L. *Solav PV supply chain presentation, .* 2009; Available from: http://www.slideshare.net/joeberwind/supplychain-presentation06-mar-090130pm.
19. Porter, M.E., *Competitive advantage: creating and sustaining superior performance*. 1985, New York: Collier Macmillan.
20. Cory K S, S., B, *Renewable Portfolio Standards in States: Balancing goals and rules*, in *Electricity Journal*. 2007.
21. Nanomarkets. *Market size estimation for DSSC and OPVs*. 2009; Available from: http://nanomarkets.net/whitepapers.
22. Engineering-village. *Search for journals and other documents*. Available from: www.engineering-village.com.
23. Sharp-Solar. Available from: www. sharp-solar.com/history/index.html.
24. Q-Cells, *Annual Report.* 2009.
25. Suntech-Power.
26. Reuters, *Suntech,Trina Solar sign $11.7 bln loan deals*, in *Reuters*. 2010.
27. SunPower. *Annual Report*. 2009; Available from: http://us.sunpowercorp.com.
28. Wikipedia. Konarka Technologies; Available from: http://en.wikipedia.org/wiki/Konarka_Technologies.
29. Technologies, K. 2010; Available from: www.konarka.com.
30. Dyesol. 2010; Available from: www.dyesol.com.
31. G24i, 2010.
32. Solar, H., 2010.
33. Besanko D, e.a., *Economics of strategy*. 2010, Hoboken NJ: John Wiley and Sons.
34. *Dogfight over Europe - Ryanair*, in *Rivkin J et al*. 2000.
35. Bloomberg, *Solar Power generation capacity may double in 2010*, in *Bloomberg*. 2009: NYC.
36. Treehugger.com, *Recession could cut solar industry in half by 2010*. 2009.
37. Teece, D.J., *Profiting from technological innovation: Implications for integration, collaboration, licensing and public policy.* Research Policy, 1986. **15**(6): p. 285-305.

38. Teece, D.J., *Competition, cooperation, and innovation : Organizational arrangements for regimes of rapid technological progress.* Journal of Economic Behavior & Organization, 1992. **18**(1): p. 1-25.
39. Rolt. *Product Catalog.* 2010; Available from: www.rolt.com.
40. Wikipedia. *Roll to Roll processing.* 2010; Available from: http://en.wikipedia.org/wiki/Roll-to-roll_processing.